



AIRBUS

Master's Degree in Aerospace Engineering

Master's Degree Thesis

Numerical Assessment of Defects Effect on Boltless Composites Longitudinal Joints

Academic Supervisors:

Prof. Enrico Cestino
Prof. Giacomo Frulla
Prof. Stefan Hallström

Author:

Mara Santaniello

Industrial Supervisor:

Dipl.-Ing. Thomas Kruse-Strack, M.Sc.
(Airbus Operations GmbH)

July 2020



Declaration

The thesis entitled “Numerical Assessment of Defects Effect on Boltless Composites Longitudinal Joints” is carried out at the company Airbus Operations GmbH in Hamburg, under the supervision of a

This document has been reviewed and determined not to contain export-controlled technical data. I hereby declare that except where specific reference is made to the work of others, the contents of this dissertation are original and have not been submitted in whole or in part for consideration for any other degree or qualification in this, or any other university.

Numerical Assessment of Defects Effect on Boltless Composites Longitudinal Joints

by Mara Santaniello

Abstract

The work presented in this thesis focuses on the numerical assessment of defects effect on potential boltless design for fuselage panels longitudinal joints, typically identified as High Load Transfer (HLT) configuration.

Nowadays, the state-of-art joining technique for primary aircraft composite structures, such as fuselage barrels, is still mechanical fastening. This conventional approach limits the full exploitation of potential benefits, achievable by composite structures, in terms of weight and cost reduction. Therefore, alternative boltless joining technologies open new possibilities to further improve the airframe design of future aircraft generations. Two major techniques are currently under investigation, namely adhesive bonding and welding, which are employable to join thermosetting- and thermoplastic-based laminated composites, respectively. Nevertheless, difficulties in assessing the quality of joining line after manufacturing restrict the applicability of boltless joint to non load-critical structural components.

This thesis aims to numerically evaluate the effect of manufacturing-induced defects, such as weak bond or disbond, on the overall performances of the structural configuration. Longitudinal joints of the fuselage of Airbus A350-XWB aircraft family are used as reference design, since they are currently carried out through single-lap bolted technique. To simulate an HLT joint, a Finite Element (FE) model of a Wide Single Lap Shear (WSLS) specimen, previously adopted as test setup during BOPACS (Boltless assembling Of Primary Aerospace Composite Structures) project, is implemented in the commercial FE software Abaqus. Damage modeling exploits the Cohesive Zone Model (CZM) approach, in which fracture energies drive damage initiation and evolution behavior. The computational loading scenario focuses on quasi-static non-linear analysis.

To assess the influence of defects on joint load-carrying capability, three different classes of joining line are investigated, namely a brittle and a ductile adhesive for adhesive bonding application, and a thermoplastic polymer matrix for welding technology. Globally, all types of boltless joints experience ultimate strength reduction whenever

damage occurs in the joining line, but each material exhibits a different decreasing trend depending on its inherent mechanical properties. In addition, two methodological approaches, which exploit only the numerical outcomes of FE quasi-static analyses, are proposed as predictive methods for fatigue response. Fatigue limits for a constant fatigue life are predicted by exploiting the Similarity Principle of stress peaks distribution. Constant Life Diagrams (CLDs) are numerically calculated by following a reverse algorithm based on experimental fatigue data extrapolated from BOPACS test campaign. On the other hand, fatigue initiation loads and fatigue lifetime are predicted by exploiting the Fatigue Crack Growth (FCG) approach and numerical integration of Paris's law. Based on these investigations, it is finally concluded that predictions of fatigue response can be preliminarily assessed by exploiting numerical outcomes of quasi-static simulations, in conjunction with limited experimental data used as starting points.

Sommario

La ricerca presentata in questa tesi è incentrata sulla valutazione numerica dell'effetto di eventuali difetti su una giunzione longitudinale, senza elementi di fissaggio meccanici, fra pannelli di fusoliera, tipicamente identificata come High Load Transfer (HLT) joint.

Lo stato dell'arte della tecnica di giunzione utilizzata per strutture primarie in composito, quali i pannelli di fusoliera, è ancora oggi il fissaggio meccanico. Questo approccio convenzionale limita il pieno sfruttamento dei potenziali benefici in termini di riduzione di peso e costi, ottenibili dalle strutture composite. Pertanto, tecnologie di giunzione alternative, senza l'utilizzo di elementi di fissaggio meccanici, aprono nuove possibilità per migliorare ulteriormente il design della fusoliera di future generazioni di aeromobili. Due sono le tecniche principali attualmente oggetto di indagine: incollaggio e saldatura, rispettivamente impiegabili per unire laminati compositi a base termoidurente e termoplastica. Tuttavia, le difficoltà nel valutare la qualità della giunzione dopo la produzione limitano l'applicabilità di tali giunzioni a componenti strutturali non critici.

Scopo della ricerca è valutare numericamente l'effetto dei difetti indotti dalla produzione sulle prestazioni della giunzione strutturale. I giunti longitudinali della fusoliera dell'aeromobile Airbus A350-XWB sono utilizzati come design di riferimento, in quanto attualmente realizzati mediante fissaggio meccanico con semplice sovrapposizione. Nel software commerciale Abaqus, per simulare un giunto HLT, è implementato un modello agli elementi finiti di un provino denominato WSL (Wide Single Lap Shear) joint, precedentemente adottato durante il progetto BOPACS (Boltless assembling Of Primary Aerospace Composite Structures). La modellazione del danno sfrutta l'approccio basato sulla teoria della zona coesiva, in cui le energie di frattura determinano l'inizio del danno e la sua evoluzione. Lo scenario di carico utilizzato durante le simulazioni numeriche si concentra sull'analisi quasi statica non lineare.

Per valutare l'effetto dei difetti sulle prestazioni statiche, sono state analizzate tre diverse tipologie di materiali, in particolare un adesivo fragile ed uno duttile per le giunzioni incollate, e una matrice polimerica termoplastica per i giunti saldati. In generale, si verifica una diminuzione del carico di rottura causata dalla presenza del danno, ma caratterizzata da una diversa tendenza di riduzione in base alle proprietà meccaniche intrinseche del materiale. Inoltre, per analizzare la risposta a fatica di tali giunzioni, due diversi approcci, che sfruttano soltanto i risultati numerici delle analisi agli elementi finiti, sono proposti come metodi predittivi. La previsione dei limiti di fatica per un numero di cicli costante è basata sull'applicazione del principio di similitudine della distribuzione dei picchi di stress. I diagrammi a vita costante

(CLDs) sono calcolati numericamente seguendo un approccio inverso, basato su dati sperimentali di fatica estrapolati dalla campagna di test BOPACS. Invece, la previsione dei carichi critici e della durata della vita a fatica sfrutta l'approccio della crescita della cricca a fatica (FCG) e l'integrazione numerica della legge di Paris. Sulla base di queste indagini, si è infine concluso che per un'analisi preliminare, possono essere effettuate previsioni della risposta a fatica sfruttando solo i risultati numerici delle simulazioni statiche, in combinazione con limitati dati sperimentali utilizzati come punti di partenza.

Acknowledgments

I am sincerely grateful to my industrial supervisor Thomas Kruse-Strack for sharing his valuable knowledge and encouraging me during my experience. I would also like to extend my gratitude to Norbert Heltsch, who shared his expertise with me during the project. Being at Airbus has been a great experience for my professional and personal growth.

I would like to thank my supervisor at KTH, Stefan Hallström, who gave me the chance to gain experience in one of the major leading companies in the aerospace industry.

I owe my deepest gratitude to my supervisors at Polito, Enrico Cestino and Giacomo Frulla, for following my activities and for their continuous support during my thesis.

Special thanks also to Nicola Cersullo, who took me under his wing during my experience at Airbus. Although it was not his job, he followed the development of my thesis and continuously helped me. I will always keep in mind your spoons of knowledge.

There will never be enough words to express my sincerest thank to my family. My parents have always supported me in all my choices and encouraged me to pursue my dreams.

I also would like to thank all the amazing friends I met during these past years, in Avellino, in Turin, in Stockholm, and in Hamburg, who helped me become who I am now. I wouldn't have made it this far without your support.

Table of contents

List of figures	x
List of tables	xv
Nomenclature	xvi
1 Introduction	1
1.1 Motivation	2
1.2 Purpose of the project	2
1.3 Limitation	3
1.4 Outline	3
2 Background	5
2.1 Fuselage Assembly Concept: Longitudinal Joint	5
2.2 Boltless Joining Technologies	7
2.2.1 Thermoset Composites Adhesively Bonded Joints	8
2.2.2 Thermoplastic Composites Welded Joints	11
2.3 Effect of Defects on Joining Quality	13
2.3.1 Manufacturing-Induced Defects	14
2.3.2 Related Work	16
3 Structural Analysis of Joining Line of SLJ	20
3.1 Load Transfer Mechanism	21
3.1.1 Pristine Joining Line	23
3.1.2 Damaged Joining Line	23
3.2 Stress Distribution and Magnitude Evaluation	25
3.2.1 Analytical Analyses: Goland and Reissner Solution	25
3.2.2 Finite Element Analysis	29

4	Finite Element Modeling of Wide Single Lap Shear joint	30
4.1	Numerical Simulation Tools	30
4.2	Laminated Composite Adherends	31
4.3	Bondline and Weldline	33
4.3.1	Constitutive Response: Traction - Separation Law	33
4.3.2	Input Parameters for Cohesive Elements	36
4.3.3	Influence of mesh size	38
4.4	Constraints and Boundary Conditions	39
4.5	Validation of the FE WSLS reference design	40
5	Methodology	42
5.1	WSLS Joint Strength Analysis	42
5.1.1	Influence of disbond size	43
5.1.2	Influence of joining line mechanical properties	44
5.2	Fatigue Strength and Lifetime Analysis	44
5.2.1	Stress-life Approach	47
5.2.2	Fatigue Crack Growth Approach	54
6	Results	60
6.1	Comparative Evaluation of Strength Reduction	60
6.1.1	Thermoset WSLS bonded joint - Loctite EA 9395	61
6.1.2	Thermoset WSLS bonded joint - Scotch Weld 9323-B/A	65
6.1.3	Thermoplastic WSLS welded joint - PEKK matrix	69
6.1.4	Discussion	72
6.2	Fatigue Numerical Predictions	81
6.2.1	Constant Life Diagrams and Fatigue Strength	81
6.2.2	Energy Criterion and Fatigue Lifetime	91
6.2.3	Methodological Proposals for Welded Joints	95
7	Conclusions	97
7.1	Summary of Research Results	97
7.2	Proposals for Future Works	99
	References	101

List of figures

2.1	Fuselage sections subdivision of an A350-900 aircraft from the Airbus A350-XWB family. Adapted from [2].	6
2.2	Schematic illustration of a WSLs boltless joint configuration.	7
2.3	Schematic illustration of manufacturing bonding techniques commonly employed for thermosetting-based laminated composites.	9
2.4	Comparison of stress distribution in a typical joint employing fasteners and adhesive bonding. Adapted from [16].	10
2.5	Schematic illustration of a disbond in the joining area of a SLJ. Adapted from [3].	15
2.6	Schematic illustration of an impact in the joining area of a SLJ. Adapted from [3].	15
2.7	Schematic illustration of a weak bond in the joining area of a SLJ. Adapted from [3].	16
2.8	Schematic illustration of bonded lap joints with different types of disbonds.	18
3.1	Schematic illustration of a SLJ.	21
3.2	Formation of shear and normal stresses in the adhesive layer of a SLJ. .	21
3.3	Adhesive layer shear deformation during the load transfer.	22
3.4	Illustration of secondary bending effect in SLJ, which causes the occurrence of peel stresses in the adhesive layer.	22
3.5	Stress distribution along the joining line of a pristine WSLs joint. Solid line illustrates shear distribution, and dashed line shows peel stress. . .	23
3.6	Principle behavior of stress distribution in a boltless WSLs joint affected by an initial disbonded area in the joining line. Adapted from [41]. . . .	24
3.7	Geometrical configuration of the SLJ for analytical solutions.	27
4.1	Typical traction-separation law for a pure-mode constitutive response. .	34
4.2	Schematic illustration of mixed-mode response for cohesive elements. .	35

4.3	Length of cohesive zone.	38
4.4	Schematic 2D illustration of the applied boundary conditions.	40
4.5	Comparison between analytical (dashed line) and numerical (solid line) shear and peel stress distribution in the adhesive layer. Only one half of the overlap length is illustrated due to symmetry reasons.	41
5.1	Schematic illustration of a squared edges disbond located in the center of the joining line, with one of its edge always approaching the overlap edge. Disbond length and width are instead adjusted for investigative purposes.	44
5.2	Schematic illustration of a sinusoidal fatigue spectrum used for laboratory investigations.	46
5.3	Schematic example of a typical Wöhler's curve. Adapted from [53].	47
5.4	Schematic example of CLDs as cross plot from $S - N$ curves. Adapted from [56].	48
5.5	Schematic illustration of the Similarity Principle between notched and unnotched specimens, for $S_m = 0$. Adapted from [56].	50
5.6	Schematic illustration of the Similarity Principle between notched and unnotched specimen, for $S_m > 0$. Adapted from [56].	51
5.7	Example of fatigue strength prediction employing the Similarity Principle, with the application of K_t to both S_a and S_m . Adapted from [56].	51
5.8	Flowchart of proposed procedure for fatigue strength predictions.	53
5.9	Example of a typical fatigue crack propagation curve for adhesively bonded joints.	54
5.10	Normalized crack width increment measured by ultrasonic inspection as a function of number of k-cycles, for two WSLS bonded configurations characterized by an initial disbond area of 12% and 16%, respectively. Extrapolated from BOPACS test campaign.	57
5.11	Normalized crack growth rate as a function of number of k-cycles. Extrapolated from BOPACS test campaign.	57
5.12	Flowchart of proposed procedure for fatigue lifetime predictions.	59
6.1	Numerical estimates of load-displacement responses of WSLS bonded joints (Loctite EA 9395 adhesive) accounting for different widths of artificial disbonds characterized by a full-damaged overlap length, compared to the numerical prediction for a pristine configuration.	61

6.2	Normalized maximum failure loads comparison between numerical predictions for WSLS bonded joints (Loctite EA 9395 adhesive) and experimental results from BOPACS test campaign, according to different initial disbond areas. Exponential trendline is displayed.	62
6.3	Predicted load-displacement responses of WSLS bonded joints (Loctite EA 9395 adhesive) considering several disbonds characterized by different sizes of length and width.	63
6.4	Linear dependence of strength reduction on the increase in disbond length in the bondline of WSLS bonded joints (Loctite EA 9395 adhesive). Results extrapolated from FE numerical simulations.	64
6.5	Influence of increasing disbond width in the bondline on strength reduction of WSLS bonded joints (Loctite EA 9395 adhesive). Results extrapolated from FE numerical simulations.	64
6.6	Numerical estimates of load-displacement responses of WSLS bonded joints (Scotch Weld 9323-B/A adhesive) accounting for different widths of artificial disbonds characterized by a full-damaged overlap length, compared to the numerical prediction for a pristine configuration.	65
6.7	Normalized maximum failure loads numerically predicted for WSLS bonded joints (Scotch Weld 9323-B/A), according to different initial disbond areas. Exponential trendline is displayed.	66
6.8	Predicted load-displacement responses of WSLS bonded joints (Scotch Weld 9323-B/A adhesive) considering several disbonds characterized by different sizes of length and width.	67
6.9	Linear dependence of strength reduction on increase in disbond length in the bondline of WSLS bonded joints (Scotch Weld 9323-B/A adhesive). Results extrapolated from FE numerical simulations.	68
6.10	Linear dependence of strength reduction on increase in disbond width in the bondline of WSLS bonded joint (Scotch Weld 9323-B/A adhesive). Results extrapolated from FE numerical simulations.	68
6.11	Numerical estimates of load-displacement responses of WSLS welded joints (PEKK polymer matrix) accounting for different widths of disbonds characterized by a full-damaged overlap length, compared to the numerical prediction for a pristine configuration.	69
6.12	Normalized maximum failure loads numerically predicted for WSLS welded joints (PEKK polymer matrix), according to different initial disbond areas. Linear trendline is displayed.	70

6.13	Predicted load-displacement responses of WSLS welded joints (PEKK polymer matrix) considering several disbonds characterized by different sizes of length and width.	71
6.14	Comparison between numerical shear and peel stress distribution in the adhesive layer of Loctite EA 9395 (solid line) and Scotch Weld 9323-B/A (dashed line). Only one half of the overlap length is illustrated due to symmetry reasons, and results are normalized using as reference the average shear stress.	73
6.15	Normalized shear stress distribution in the adhesive layer of Loctite EA 9395 (solid line) and Scotch Weld 9323-B/A (dashed line) when a damage is present in the bondline, extrapolated from FE numerical simulations. The red line indicates the stress evaluation line.	74
6.16	Comparison between different shear stress redistributions in the adhesive layer of brittle Loctite EA 9395 adhesive caused by several damage sizes, for a specific applied load, extrapolated from FE numerical simulations. Red lines indicate the stress evaluation lines.	75
6.17	Comparative evaluation of normalized ultimate joint strength reduction as a function of increasing initial disbond area, extrapolated from FE numerical simulations.	76
6.18	Particular detail of joint strength reduction for an initial disbond area of 4%, for Loctite EA 9395 and Scotch Weld 9323-B/A adhesives, extrapolated from FE numerical simulations.	77
6.19	Comparative evaluation of normalized ultimate joint strength reduction as a function of increasing initial disbond area for WSLS bonded and welded joints, extrapolated from FE numerical simulations.	78
6.20	Normalized shear stress redistribution in the weldline of a WSLS joint as a function of several disbond sizes, extrapolated from FE numerical simulations.	80
6.21	Normalized shear stress redistribution in the bondline of WSLS joints affected by different full-length disbond sizes. Red lines represent normalized shear stress distribution for a healthy bondline. Extrapolated from FE numerical simulations.	82
6.22	Normalized shear stress redistribution in the bondline of WSLS joints affected by several disbond sizes, with different combination of length and width. Red lines represent normalized shear stress distribution for a healthy bondline. Extrapolated from FE numerical simulations. . . .	83

6.23	Stress concentration factors K_t for several WSLS joints affected by different initial disbond areas.	84
6.24	Estimation of CLDs for $N_f \approx 7 \cdot 10^5$ accounting for several disbond sizes, by exploiting the Similarity Principle between damaged and pristine structural components.	85
6.25	Fatigue strength predictions for both pristine and damaged WSLS bonded joints, for a fatigue lifetime of $N_f \approx 7 \cdot 10^5$ and $R = 0.1$, by exploiting the Similarity Principle.	86
6.26	Shear stress distribution at the overlap edge of two WSLS damaged configurations characterized by the same initial disbonded area, but different damage orientation within the bondline. Extrapolated from FE numerical simulations.	87
6.27	CLDs of adhesively bonded joints extrapolated from fatigue test results by means of both Goodman and Gerber analytical approximations exploited as predictive models.	88
6.28	Examples of CLDs with experimental fatigue strength data of notched and unnotched specimens. Blue dots refer to fatigue strength of unnotched specimens, whereas red dots to fatigue response of notched configurations. Data from Schijve [56].	89
6.29	Fatigue crack growth rate da/dN in the adhesive layer of a pristine WSLS bonded joint at 140 kN, which is the estimated no-growth load level.	91
6.30	Fatigue crack growth rate da/dN in the adhesive layer of two WSLS bonded configurations with initial disbonds at 110 kN, which represents the fatigue initiation load.	92
6.31	Fatigue lifetime prediction for WSLS bonded joints affected by initial disbonds of 12% and 16%, as a function of crack increment.	93

List of tables

3.1	Unified notation for SLJ model.	27
4.1	List of software and hardware used for the numerical investigation. . .	31
4.2	Input parameters for thermosetting-based laminated composite adherend.	32
4.3	Input parameters for thermoplastic-based laminated composite adherend.	32
4.4	Geometrical dimensions of the cohesive layer.	36
4.5	Input parameters for Loctite EA 9395 adhesive.	37
4.6	Input parameters for Scotch Weld 9323-B/A adhesive.	37
4.7	Input parameters for PEKK polymer matrix.	38
4.8	Summary of maximum shear and peel stresses in the adhesive layer predicted by Goland and Reissner analytical analysis and the proposed FE model.	40
6.1	Numerical results of ultimate joint strength for bonded and welded WSLS joints affected by different initial disbond areas.	79
6.2	Numerical evaluations of stress concentration factor K_t induced in the bondline of WSLS bonded joints due to the presence of initial disbonds.	84
6.3	Numerical results of fatigue strength predictions for a fatigue lifetime of $N_f \approx 7 \cdot 10^5$ and $R = 0.1$, computed by exploiting the Similarity Principle.	86

Nomenclature

Greek Symbols

β	Constant factor for Goland and Reissner analytical solutions
Δ	Change of any changeable quantity
δ	Displacement
η	B-K exponent for traction-separation law
η_{ci}	B-K exponent for Paris's law definition
γ	Constant factor for Goland and Reissner analytical solutions
λ	Constant factor for Goland and Reissner analytical solutions
ν	Adherends Poisson's ratio
ν_a	Adhesive Poisson's ratio
Ω	Constant factor for Goland and Reissner analytical solutions
σ	Normal stresses
τ	Shear stresses
ε	Strain

Latin Symbols

A	Constant factor for Goland and Reissner analytical solutions
a	Crack extension
B	Constant factor for Goland and Reissner analytical solutions

b	Adherends/Overlap width
c	Half of boltless joint overlap length
C_1, C_2	Paris's law constant parameters
$C_{i,I}, C_{i,II}$	Fitting parameters
da/dN	Fatigue crack/disbond growth rate
E	Adherends Young's modulus
E_a	Adhesive Young's modulus
f	Frequency
G	Adherends Shear modulus
G	Strain energy release rate
G^c	Critical fracture energy
G_a	Adhesive Shear modulus
K	Stress intensity factor
k	Non-linear bending moment factor
k'	Non-linear transverse force factor
K_f	Fatigue notch factor
K_t	Stress concentration factor
L	Overlap length
l	Adherends length
l_{cz}	Length of cohesive zone
M	Characteristic model parameter
N	Number of cycles
N_e	Number of element in the cohesive length direction
N_f	Number of cycles to failure

P	Tensile load
P_{max}	Maximum fatigue load
R	Stress ratio
S	Stress
S_e	Fatigue strength
S_f	Fatigue or endurance limit
t	Adherends thickness
t^0	Maximum traction stresses
t_a	Adhesive thickness
T_g	Glass-transition temperature
t_l	Lamina thickness
T_m	Melting temperature
u_2	Constant factor for Goland and Reissner analytical solutions
x	x-coordinate of the global coordinate system along the joint width
y	y-coordinate of the global coordinate system along the joint length
z	z-coordinate of the global coordinate system across the joint thickness

Subscripts/Superscripts

$(-)^{inst}$	Instantaneous value
$(-)_0$	Initial
$(-)_{1,2,3}$	Principal lamina coordinate system
$(-)_{ave}$	Average
$(-)_a$	Amplitude
$(-)_f$	Final
$(-)_t$	Full-length disbond

$(-)_max$	Maximum
$(-)_min$	Minimum
$(-)_m$	Mean
$(-)_n/nn$	Normal direction
$(-)_n$	Notched
$(-)_s/ss$	Longitudinal shear direction
$(-)_t/tt$	Transverse shear direction
$(-)_th$	Threshold
$(-)_un$	Unnotched
$(-)_u$	Ultimate
$(-)_w$	Width-oriented disbond
$(-)_x,y,z$	Global coordinate system
$[-]_s$	Layup with mid-plane symmetry

Acronyms

2D	Two dimensional
3D	Three dimensional
B-K	Benzeggagh-Kenane
BJ	Butt Joint
BOPACS	Boltless assembling Of Primary Aerospace Composite Structures
CAE	Computer-Aided Engineering
CFRP	Carbon-Fiber-Reinforced-Polymer
CLD	Constant Life Diagram
CO₂	Carbon dioxide
CZM	Cohesive Zone Model

DCB	Double Cantilever Beam
ENF	End-Notched Flexure
EU	European Union
FAL	Final Assembly Line
FCG	Fatigue Crack Growth
FEA	Finite Element Analysis
FE	Finite Element
HLT	High Load Transfer
HPC	High Performance Computing
LEFM	Linear Elastic Fracture Mechanics
MCA	Major Component Assembly
MDPE	Medium Density Polyethylene
MMR	Mix Mode Ratio
NDT	Non-Destructive Testing
NO_x	Nitrogen Oxides
PEEK	Polyetheretherketone
PEKK	Polyetherketoneketone
RTD	Room Temperature ambient
SLJ	Single Lap Joint
WSLS	Wide Single Lap Shear
XWB	eXtra Wide Body

Chapter 1

Introduction

Over the past decades, the aeronautical industry recorded increasing requests for improved aircraft performances. Innovation plays a crucial role in the development of more efficient airframe design, impacting quality, cost, and performance. Therefore, the achievement of a more lightweight structural design represents one of the primary objectives for aircraft designers to lower maintenance costs and to promote more eco-sustainable operations [1].

A significant weight reduction has already been accomplished with the introduction of carbon fiber-reinforced composite materials in the airframe design, where they are gradually replacing their metallic counterparts [2]. Nevertheless, the state-of-art joining technique for primary composite structures, such as fuselage panels, is still mechanical fastening. It limits the full exploitation of potential benefits achievable by composite materials in terms of weight and cost reduction [3]. Therefore, alternative *boltless* joining technologies open new possibilities to further improve the airframe design of future aircraft generations.

Two major technologies offer interesting perspectives for joining of primary composite structural components, namely adhesive bonding and welding, employable to join thermosetting-based and thermoplastic-based composites, respectively. Nonetheless, none of these techniques has been certified to be totally reliable and safe up to now. Indeed, one of the major challenges in implementing boltless joining technology for large structures lies in assessing the quality of the joining line after manufacturing or during in-service operation [4, 5]. Lack of adhesion or fusion in the joining area leads to unintended defects, which negatively affect joint load-carrying capability and fatigue response. Therefore, to achieve a future application of boltless joining technologies for primary composite aircraft structures, a full understanding of the effect of defects on the joint's overall performance has to be established. In particular, reliable testing methods

and numerical predictive modeling need to be developed to assess and demonstrate the structural integrity of this type of joints.

1.1 Motivation

As one of the major international leaders in the aerospace industry, Airbus has invested extensive efforts in designing and manufacturing more efficient and cost-effective aircraft. With the delivery of the A350-XWB (eXtra Wide Body) aircraft family, a reviewed and improved design has been achieved by offering a lightweight airframe made of 53% of composites. It enables a reduction of operating costs by 25% and more eco-efficient operations [2].

Currently, boltless joining technology such as adhesive bonding is employed for bonding stringers to fuselage and wing panels, or for elevators, ailerons, and spoilers [6]. Nevertheless, the use of boltless joints for primary composite structures is still limited due to current certification guidelines and design rules [3].

Within Airbus, the potential application of the adhesive bonding technique for primary structures has been investigated during BOPACS (Boltless assembling Of Primary Aerospace Composite Structures) project [7], which aimed to assess fatigue behavior of wide bonded joint affected by artificial disbond. On the other hand, the exploitation of welding technology for thermoplastic composites represents a “must” for future generations of aircraft fuselage, which is the focus of the project *Fuselage of Tomorrow* [8]. The final objective is to enable a faster and more efficient production rate at competitive levels.

The studies proposed in this thesis embrace both possibilities of alternative boltless joining technologies, and propose a further step towards a more comprehensive understanding of structural boltless joint behavior. This master thesis is conducted under the auspices of Airbus Operations GmbH located in Hamburg, Germany.

1.2 Purpose of the project

This thesis aims to numerically investigate the effect of manufacturing-induced defects in the joining line of bonded and welded joints on the overall performances of the structural configuration. Longitudinal joints of composite fuselage of the Airbus A350-XWB aircraft family are taken as reference to investigate a potential realistic application scenario of boltless joint for primary structures.

Through the implementation of suitable Finite Element (FE) models, fracture behavior of the joints is evaluated by exploiting numerical outcomes of quasi-static analysis to assess ultimate strength reduction induced by several different defects sizes. In addition, these investigations aim to provide a deeper understanding of the influence of mechanical properties of the different joining line on the joint behavior when a defect is artificially introduced in the model.

Finally, this thesis aims to propose suitable methodological approaches to predict fatigue behavior of boltless joints affected by process-induced defects by exploiting numerical outcomes of quasi-static analysis and available experimental test data. Similar studies are used as comparison according to their relevance for fatigue response predictions.

The comparative evaluation obtained through numerical investigations represents a preliminary assessment of the effect of defects on potential boltless longitudinal joints in terms of ultimate strength reduction and fatigue response.

1.3 Limitation

The work done in this thesis is limited to computational simulations carried out by commercial FE software, i.e. no specimens manufacturing or experimental testing has been conducted within the time frame of this study. The input data for FE analysis are based on preliminary experimental characterization of material properties performed during previous Airbus projects.

Numerical investigations proposed in this thesis are focused on a quasi-static loading scenario. Implementation of user-defined subroutines for cycling fatigue load simulation in commercial FE software is outside the scope of the work, which instead focuses on the potential exploiting of quasi-static analysis outcomes for fatigue prediction.

1.4 Outline

The manuscript is divided into three major sections: a global background, an overview of structural analysis techniques and proposed methodological approaches, and the results and discussion of the findings.

Chapter 2 provides the frame of reference for this study, delving into the main topics that establish the background. A suitable structural application scenario for primary boltless joint is introduced based on the current assembly concept for aircraft fuselage. A basic understanding of different joining technologies is provided along with

the description of difficulties arisen from the manufacturing process. A summary of previous researches concerning the effect of defects on joint performances is presented.

Chapter 3 delves into the structural behavior of Single Lap Joint (SLJ), in terms of stress distribution and magnitude, explaining the effect of defects on the load transfer mechanism. Stress analysis methods are introduced, focusing on the analytical solutions that are exploited to validate the proposed numerical model.

Chapter 4 describes the baseline FE model proposed for the simulation of a boltless longitudinal joint, focusing on the Cohesive Zone Model (CZM) theory used to simulate the mechanical behavior of the joining line.

Chapter 5 delves into the methodologies and approaches exploited to numerically assess the effect of defects on the performance of both bonded and welded joints in terms of load-carrying capability and fatigue response.

Chapter 6 provides the numerical results of computational quasi-static simulations. A comparative evaluation of ultimate joint strength reduction is presented, assessing the influence of several disbond sizes on different materials used to simulate the joining line. Numerical predictions of fatigue response in terms of fatigue strength and lifetime are presented for bonded joints, based on the available experimental data.

Chapter 7 summarizes the significant outcomes obtained from these studies, along with proposals and suggestions for future works to improve numerical predictive modeling of boltless structural joints.

Chapter 2

Background

This Chapter provides an outline of the main topics that establish the background of this thesis. An overview of one of the major components of the airframe, i.e. the fuselage, is introduced, and a potential realistic application scenario for a boltless primary joint is suggested, exploiting as benchmark the Airbus A350-XWB aircraft family. In addition, in-depth descriptions of the most widespread boltless joining technologies for composite materials, namely adhesive bonding, and welding, are presented, focusing on the differences between thermosetting- and thermoplastic-based composite materials. Although those joining technologies show significant advantages compared to the state-of-art joining technique, i.e. mechanical fastening, in terms of weight and cost reduction, their applications are still limited to non load-critical structures. It is mainly due to difficulties in assessing and inspecting bondline quality after manufacturing, which can induce unintended defects in the joining line. A literature overview of prior investigations concerning the effect of defects on joint performances, i.e. load-carrying capability and fatigue response, is proposed, pointing out similarities and differences with the studies carried out in the framework of this thesis.

2.1 Fuselage Assembly Concept: Longitudinal Joint

The central body of an airplane is the fuselage, which represents one of the Major Component Assembly (MCA) of an aircraft. It is designed to join and connect all the other components together, such as wings, empennage, and landing gears. In addition, the fuselage provides the space to safely accommodate passengers, crew members, cargo, and other equipment and controls [9].

The manufacturing of commercial aircraft fuselage relies on a classical sections assembly concept, and the complete joining of the fuselage is carried out in the Final

Assembly Line (FAL). Indeed, the main body of the aircraft is usually divided into several sections: nose section, forward fuselage, central fuselage, aft fuselage, and rear fuselage. Figure 2.1 illustrates fuselage sections breakdown, using as representative case an A350-900, which belongs to the Airbus A350-XWB family.

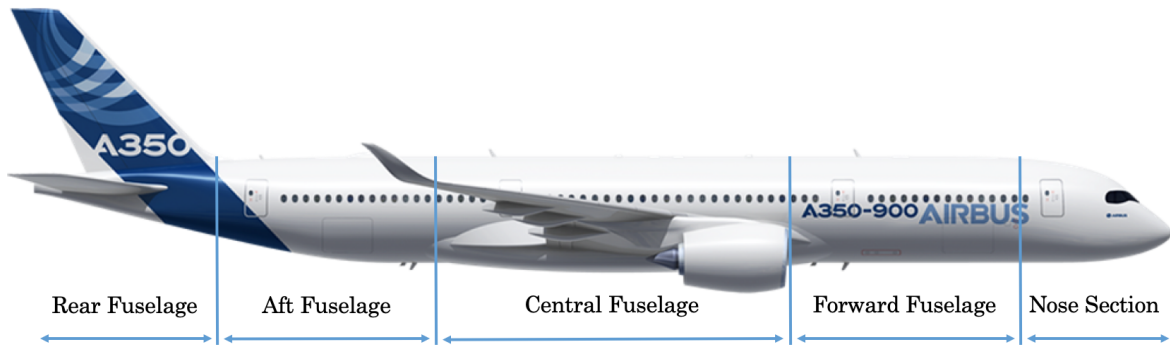


Figure 2.1 Fuselage sections subdivision of an A350-900 aircraft from the Airbus A350-XWB family. Adapted from [2].

In particular, Aft Fuselage and Forward Fuselage sections of the A350-XWB Family consist of four long panels joined together through bolted longitudinal joints [2]. For this aircraft family, the longitudinal joint can be carried out by either one panel simply overlapping the other, commonly called Single Lap Joint (SLJ), or two panels joined side-to-side, usually defined Butt Joint (BJ). Afterward, fuselage sections are joined together through circumferential joints, which can be either SLJ or BJ configuration.

Nowadays, the SLJ configuration is used for the longitudinal joints [10], and the state of the art joining method is mechanical fastening. From an industrial point of view, SLJ is an excellent combination of simplicity of manufacturing and efficiency in terms of mechanical strength. Among all the basic requirements for longitudinal joints, their main task is to ensure loading transfer between the panels. The primary loading acting on longitudinal joints is due to the differential pressure between the internal cabin value and the external atmosphere, which induces a cyclic tensile loading on the joint during each flight cycle. Therefore, longitudinal joints must be able to withstand both ultimate loads and in-service fatigue loading.

Within the scope of this thesis, longitudinal SLJ of fuselage panels is chosen as baseline to investigate a realistic application scenario of boltless joint configuration, i.e. joining of fuselage panels without any conventional mechanical fasteners. In particular, to ensure compatibility with future experimental investigations, a Wide Single Lap Shear (WSLS) joint is exploited as reference design to simulate a High

Load Transfer (HLT) joint such as longitudinal joints of fuselage panels [3]. Figure 2.2 provides a schematic illustration of a WSLs joint, consisting of two panels joined together by a simple overlay. Fuselage panels of A350-XWB are made of Carbon-Fiber-Reinforced-Polymer (CFRP) to achieve weight reduction and to exploit the flexibility of material application where structure robustness is required [2]. State-of-art A350-XWB bolted longitudinal joint provides the reference dimension for the overlap length in the boltless configuration [2]. By exploiting this layout, a direct comparison between the investigated configuration and state of the art would be feasible. Moreover, the geometrical matching of bolted and boltless overlap length keeps open the option of a bolted repair in case of damage in the overlap area.

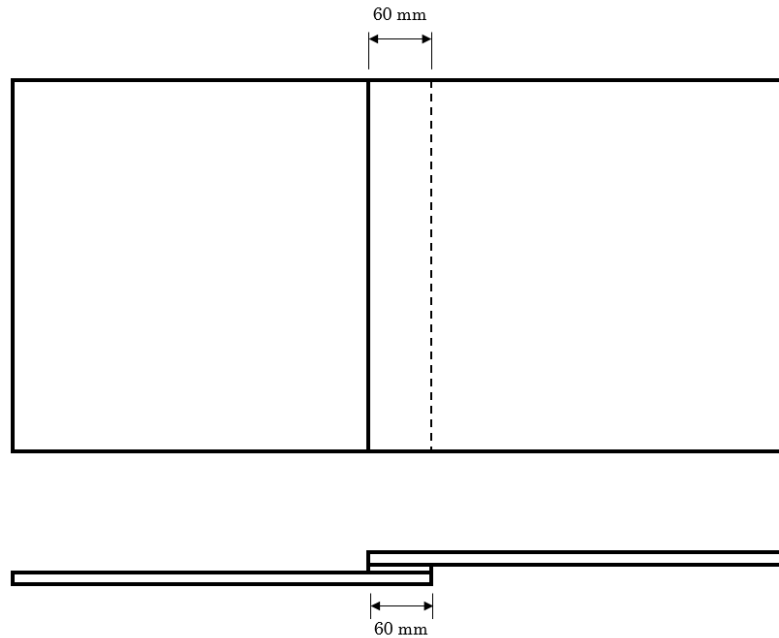


Figure 2.2 Schematic illustration of a WSLs boltless joint configuration.

2.2 Boltless Joining Technologies

Reducing operating costs has always been the main driving force of the aeronautical industry. It constantly aims to more efficient structural design to ensure lower maintenance costs, fuel consumption reduction, and eco-sustainable operations, which imply the decrease of CO₂ emissions per passenger per kilometer [1]. A major weight reduction has been achieved with the introduction of CFRP in the airframe design [4]. In particular, both thermoset and thermoplastic polymers can be used as binding matrix for CFRP. The resulting composites find extensive application in aerospace

structures, in which they are gradually replacing their metallic counterparts [11]. This increasing interest in composite materials is due to their higher specific mechanical properties, i.e. defined as the ratio of property value to material mass, in terms of strength and stiffness compared to metals. Nonetheless, one of the major limiting key issues for full exploitation of composite materials is represented by joining, and the possibility of *boltless joining* remains the most significant technical challenge for the scientific engineering community.

Nowadays, CFRP primary aircraft structures are mainly assembled by conventional mechanical fastening [1, 4]. According to current certification guidelines and design rules [3], joining of primary composite structures implies local thickening of the joint area due to thickness requirements for fasteners. Several rows of bolts are used to ensure airtight joint, to transfer loads between structural components, and to prevent premature failure modes. Nevertheless, mechanically fastened joints are subjected to particularly severe stress concentrations around the bolts because the load transfer mechanism only relies on a portion of the available joining area. Moreover, the load-carrying capability of CFRP structures is strongly affected by the presence of holes and cut-outs, which damage reinforcing fibers and represent potential sites for delamination [1]. Therefore, composite structures assembled by mechanical fasteners implies significant penalties in terms of weight and cost. Indeed, they reduce potential economic benefits resulting from the use of CFRP for airframe design [11].

Over the last decades, extensive research has focused on assessing reliable boltless joining technology for primary aircraft structures [1, 12, 13, 14]. Through experimental and numerical investigations, the aim is to achieve the potential weight reduction expected by CFRP structural components. In particular, two major joining technologies are widely under examination, namely adhesive bonding of thermosetting-based composites, and fusion bonding or welding of thermoplastic-based composites. Nevertheless, each technology exhibits different potential advantages and drawbacks, and safety considerations still limit a more widespread application of boltless joining technology for primary aircraft structures [5].

2.2.1 Thermoset Composites Adhesively Bonded Joints

Adhesive bonding is a joining process in which a thin layer of adhesive is placed in between two composite adherends, and as result of a hardening process, commonly called curing, a strong adhesively bond is secured at the interfaces [15].

Adhesives used for joining aeronautical structural components are frequently epoxy-based and are mainly exploited to bond thermosetting-based laminated composites

due to compatibility between adherends matrix and adhesive [5]. Indeed, epoxy is usually employed as a high-performance matrix among all thermoset resins since it is characterized by high strength and temperature resistance, excellent resistance to corrosive environments, in conjunction with relatively low curing temperature and low material cost.

In order to form durable solid laminates and joints, thermoset resin undergoes a curing process to enable 3D cross-links between the polymer chains [16]. This process is governed by chemical reactions induced by heating, which can be either produced by the reactions themselves or supplied from the outside, e.g. autoclave. Like all heat-driven processes, long cycle times are expected to cure thermosetting-based laminated composite and, consequently, epoxy-based adhesives. Nevertheless, once the resin is completely cured, the thermosetting-based composite materials can not be re-shaped, since the cross-linking process is irreversible. Due to that, recycling, reuse, and recovery of thermoset composites are extremely complicated and represent some of the major issues concerning environmental sustainability.

Three main bonding processes are currently employed to manufacture adhesively bonded joints of thermosetting-based laminated composites, namely co-curing, co-bonding, and secondary bonding [17]. Figure 2.3 provides a schematic illustration of these bonding techniques, which correspond to different levels of integration [3].

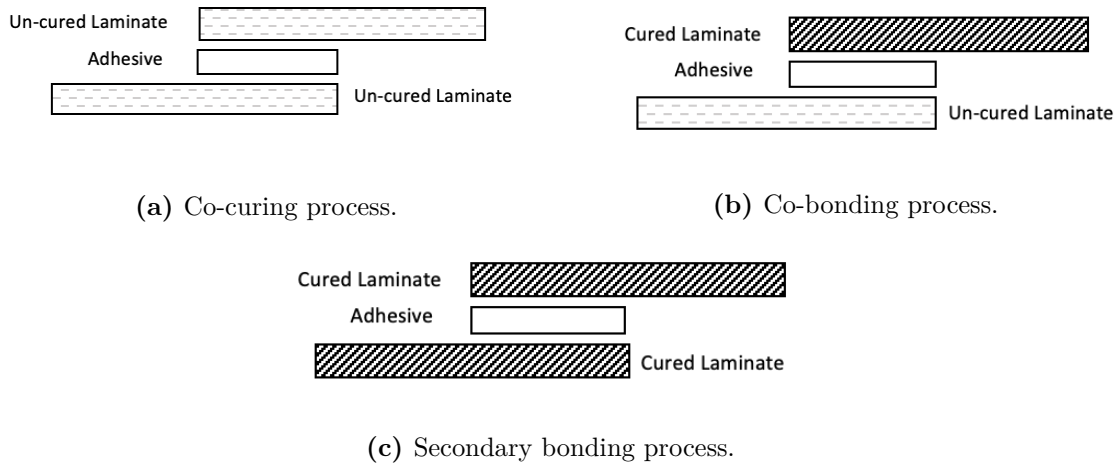


Figure 2.3 Schematic illustration of manufacturing bonding techniques commonly employed for thermosetting-based laminated composites.

In the co-curing process, the curing phase occurs for both composite adherends and adhesive simultaneously, resulting in a fully integrated structural component. Co-curing represents the highest stage of integration. Co-bonding defines an intermediate level of

integration, and the curing process affects only the adhesive and one adherend, which is still un-cured. Finally, during the secondary bonding process, the adhesive is placed in between two previously cured laminated composites, and thermal or chemical reactions occur only to cure the adhesive itself. This process represents the lowest stage of integration, but it is the most suitable process to join complex and large structures. On the contrary, since the number of curing cycles is reduced, co-curing and co-bonding are usually preferred for the repair of composite structural joints [17].

Adhesively bonded joints of thin-walled composite structures offer several advantages compared to conventional mechanical fastening [16]. More uniform stress distribution within the overlapping area is secured by reducing detrimental stress peaks concentration around the holes, as shown in Figure 2.4. By eliminating mechanical fasteners, fiber cuts and dust due to drilling are avoided, and a significant weight reduction is achieved [11]. In addition, adhesively bonded joints provide smooth external surfaces and a full seal from the external environment.

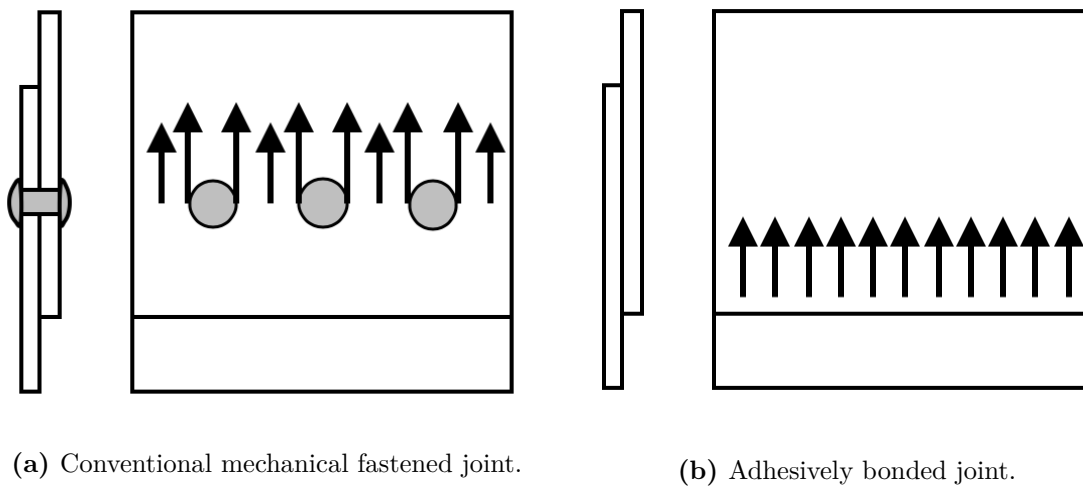


Figure 2.4 Comparison of stress distribution in a typical joint employing fasteners and adhesive bonding. Adapted from [16].

Nevertheless, adhesively bonded joints present some disadvantages over the conventional mechanical fastening process [16]. Firstly, adhesive bonding induces a permanent joint between structural components, which can not be easily disassembled without consequent damages of the adherends. Therefore, mechanical fastening is still required, for instance, to guarantee access to hidden substructures. In addition, adhesive performances are highly affected by harsh environmental conditions, in particular temperature and humidity. Irreversible chemical and physical changes may occur due to high-temperature exposure and moisture absorption, leading to reduced bond

strength and long-term durability. Thermosetting-based adhesives are also perishable, and proper refrigerated storage needs to be provided according to manufacturer's recommendations. Moreover, during the joining, chemical reactions take place between adherends and adhesive layer and suitable curing process in terms of time and temperature must be ensured to assemble the parts. However, the most crucial drawback of adhesively bonded joints lies in their sensitivity to surface preparation, which governs the quality of the bondline. Indeed, poor surface preparation leads to improper bonding of the adherends, causing premature failure of the joint.

Within Airbus, adhesive bonding of thermosetting-based composites has been investigated during BOPACS project [7]. The EU-funded FP7 project aimed to propose a rigorous road map for the use of adhesively bonded boltless joints in primary aircraft structures with compliance of airworthiness requirements. Currently, adhesive bonding is a common joining technology for bonding stringers to fuselage and wing panels, or for elevators, ailerons, and spoilers [6].

2.2.2 Thermoplastic Composites Welded Joints

To overcome the technical issues related to adhesive bonding of thermosetting-based composites such as unavoidable curing cycle, intensive manufacturing labor for surface preparation, and environmental sustainability, the demand for thermoplastic composite materials has continuously increased in the last decades [14]. In particular, advanced thermoplastic-based composites, such as carbon fiber reinforced PEEK and PEKK, have become a great promise as materials for future aircraft generations [18].

The main difference between thermoset and thermoplastic resins lies in the chemical structure of their polymer chains [16]. Thermoplastic resins are solid and fully reacted even before processing. Then, the melting process is induced by heating to allow fibers impregnation, and subsequently, pressure is applied to obtain the desired shape. During these processes, no chemical reactions occur, meaning that no permanent 3D cross-linking between polymer chains is created. Instead, only weak secondary bonds hold together polymer chains. For this reason, thermoplastic composites can be re-formed and re-processed by simply re-heating the component at the required process temperature.

Due to their inherent structure, thermoplastic composites offer several advantages in terms of mechanical performances compared to conventional thermosetting-based composites [14]. In particular, they exhibit higher fracture toughness since they are not characterized by a rigid 3D cross-linked configuration. Moreover, they show better performance in terms of damage tolerance and impact resistance compared to

untoughned thermosetting-based composites, along with low storage cost and infinite shelf life. Indeed, proper refrigeration and storage are not required for thermoplastic composites since their fabrication is not based on chemical reactions.

Since no curing is required, the manufacturing process of thermoplastic composites is potentially simpler and faster compared to thermoset counterparts [16]. Indeed, while curing cycles require hours, melting and subsequent consolidation of thermoplastic only take minutes. Nevertheless, higher temperature and pressure are required, which can lead to an increase in manufacturing costs. However, these processes can be easily automated by developing a reliable and cost-effective manufacturing technique that includes forming and joining of thermoplastic composites. This innovative fabrication procedure allows a high level of structural integration [14]. Therefore, the improvement of joining technology for thermoplastic composite structures is an essential step towards a faster pace of aircraft assembly to offset high raw-material and integration costs.

The most suitable joining technology for thermoplastic composites is fusion bonding, commonly known as welding [19]. Indeed, welding technology exploits the inherent capability of thermoplastic composites to be melted and consolidated without any physical or mechanical degradation. Moreover, this process can largely eliminate issues regarding detrimental stress concentration due to mechanical fastening, and polymers incompatibility for adhesive bonding. In principle, thermoplastic welding consists of heating polymer surfaces above a specific temperature, which is the melting temperature T_m for semi-crystalline polymers, and the glass-transition temperature T_g for amorphous polymers, to enable polymer chains mobility. Subsequently, their diffusion across the welding area is induced by pressure, which leads to a full entanglement of polymer chains. This results in the disappearance of joint interfaces in the welded area, which in turn develops the ability of loads transferring. In addition, pressure application is exploiting during the consolidation phase until complete cooling. Hence, the stress distribution within the welded area can be compared to the state that develops within the adhesive layer of a bonded joint (see Figure 2.4b). Indeed, after joining, the welding area shows a thin resin enriched film, in which no fibers reinforcement is present [20].

Based on how heat is generated at the joint surfaces, three main categories of thermoplastic welding technologies can be identified, namely friction welding, thermal welding, and electromagnetic welding [14].

In friction welding, frictional work generates the heat at welding interfaces under the application of pressure. In particular, ultrasonic welding gained much attention from the scientific and research community because it is deemed to be faster and cleaner than other techniques [13]. This process exploits high-frequency mechanical

vibrations to weld parts that are kept together by applying pressure and are subjected to ultrasonic oscillation. A combination of surface and intermolecular friction produce heating. Ultrasonic welding is a suitable technology for aerospace applications since it enables a high level of automation and production rates [21].

Thermal welding consists of two phases, namely the heating and the forging stage. The former involves direct heating supply at welding interfaces, whereas during the latter, the interfaces are forced together by pressure application. During the past decades, laser welding stands out from the other thermal welding technologies. Indeed, this method is characterized by contact-free energy introduction, which can be directed to a small specific area, resulting in advantageous opportunities over the other welding processes [22]. Moreover, laser welding is known as a fast and clean technique that is currently under investigation for future aerospace applications.

The last category is electromagnetic welding that involves inserts, such as stainless steel, graphite, or ceramic, between the parts to join. This insert material is heated by electromagnetic field of electrical current causing the melting of polymer interfaces. In this area, resistance welding appears to be the most promising technology, since it is simple, low cost, and adaptable to automation [19, 23]. So far, aerospace applications of resistance welding can be found in the fiberglass-reinforced thermoplastic J-nose leading edge on the Airbus A340-500/600 and A380 aircraft [24].

Within Airbus, thermoplastic welding technology represents the main focus of the project *Fuselage of Tomorrow*, which aims to achieve a “faster, greener, and more competitive production for future generation of European airliners” [8]. By using thermoplastic composites, the target objective is a fuselage weight reduction by a ton that results in a significant decrease of CO₂ and NO_x emissions, and recurring operational costs. One of the major deliverables of the project is the manufacturing of an 8-meter long full fuselage barrel by 2022 by exploiting the welding technology of large thermoplastic composite structures. Instead of riveting, potential industrial benefits of welding involve the possibility of high-speed joining technology, which can be easily automated, to enable a fast and efficient high volume production rate while reducing the overall manufacturing costs.

2.3 Effect of Defects on Joining Quality

Nowadays, the application of boltless joints, such as adhesive bonding or welding, for primary aerospace structures has not been certified yet as a totally reliable joining technology [3]. This is mainly due to difficulties in assessing and inspecting the

quality of the joining line after manufacture and during in-service operations [4, 5, 25, 26]. Lack of adhesion or fusion in the joining area represents a potential trigger for premature failure of the overall joint since defects negatively influence strength and fatigue response of the joint [3, 27]. Indeed, the presence of defects in the joining line induces a stress state alteration due to their inability to transfer loads between substrates. Local increase of stresses leads to joint strength reduction, which was not taken into account during the structural joint design. [28].

The quality of the joining line, i.e. bondline or weldline, is affected by several parameters, and in particular small inaccuracies during the manufacturing process can result in improper joining of the substrates. In the following Sections, the main types of manufacturing-induced bond and weld defects are described and for each one, the possible root causes are highlighted. In addition, a literature overview of prior investigations carried out on the effect of defects in composites joints is presented. Indeed, in order to achieve the future objective of boltless joints for primary aircraft structures, several evaluation and testing methods have to be developed to assess and demonstrate the structural integrity of this type of joints under realistic application scenarios.

2.3.1 Manufacturing-Induced Defects

Manufacturing-induced defects occur during the process of either adhesively bonding or welding two composite substrates together. Concerning the former type of joints, these defects can be induced by improper curing process parameters, surface contamination due to release agents, or level of moisture absorbed prior bonding [4]. Welding of thermoplastic composites is extremely sensitive to process setting parameters, such as insufficient or excessive supplied heating, welding rate, or improper parts design [29]. In the following, three main representative scenarios of manufacturing-induced defects are presented using a SLJ as reference model, and the potential root causes are highlighted for each one.

Disbond

A disbond represents a locally not-connected area between the two composite substrates, as illustrated in Figure 2.5. Possible contamination of the surface of the adherends is the main root cause for a disbond in adhesively bonded joints [3]. In contrast, incomplete welding caused by inappropriate setting parameters may induce a weld

disbond [25]. However, this type of defect can be detected by Non-Destructive Testing (NDT) methods, according to the minimum threshold detectable limit.

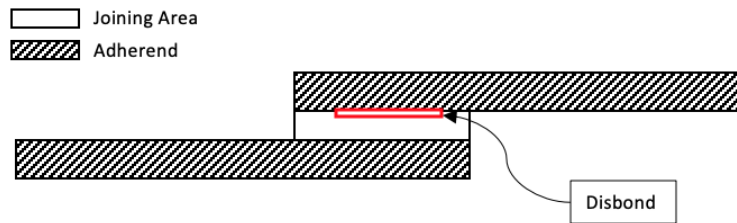


Figure 2.5 Schematic illustration of a disbond in the joining area of a SLJ. Adapted from [3].

Impact

Impact events can occur during the manufacturing or in-service and can cause initial damage in the substrates and the joining line [3]. Figure 2.6 provides an illustration of an impact on a SLJ. As before, NDT methods can detect this type of damage.

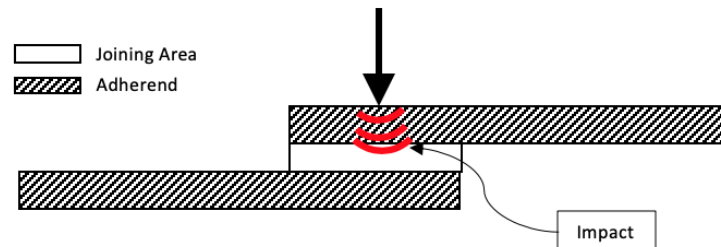


Figure 2.6 Schematic illustration of an impact in the joining area of a SLJ. Adapted from [3].

Weak bond

A weak bond is characterized by an area of strength reduction between the two substrates (see Figure 2.7), which may lead to premature failure of the joining line. For adhesively bonded joints, a possible root cause is an inadequate adhesion between adhesive and adherend, which can be the result of surface contamination or poor process conditions [3]. For welded joints, lack of fusion between the two laminates due to insufficient heating during the welding process may induce a weak bond in the weldline

[25]. Weak bonds are also called *kissing bonds* [3, 29]. This type of defect prevents the application of boltless joints for primary aircraft structures since no existing NDT techniques can detect them due to the absence of a detectable interface layer.

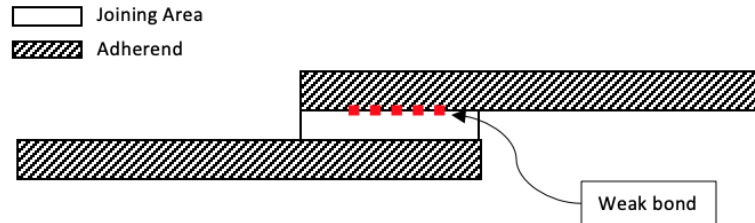


Figure 2.7 Schematic illustration of a weak bond in the joining area of a SLJ. Adapted from [3].

2.3.2 Related Work

The effect of inherent defects induced by manufacturing processes has been the focus of several numerical and experimental investigations, in particular regarding adhesively bonded joints. Indeed, it is fundamental to evaluate whether a joint affected by a bondline defect is still able to perform its tasks, or it needs to be repaired or even replaced [27].

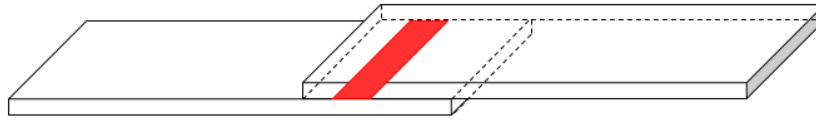
Early studies carried out by Wang et al. [30] investigated the effect of bonding defects on the strength of a SLJ characterized by a brittle epoxy-based adhesive. Circular defects placed in the middle of the bondline did not affect the joint strength, whereas rectangular-shaped defects arranged along the full width of the bondline caused a significant strength reduction. It was concluded that for a brittle adhesive, failure is mainly governed by the overlap edges. Schonhorn et al. [31] analyzed the effect of defects on the behavior of a ductile adhesive. It was shown that the strength of a SLJ with a relatively flexible adhesive, such as low-density polyethylene, is ruled by the bonded area rather than overlap leading edges. Olia et al. [32] developed a closed-form solution for adhesively bonded joint affected by centered symmetrical through-width gaps in the bondline. The analysis focused on a SLJ loaded in tension and bending, with both isotropic and orthotropic adherends. It was concluded that the far-field stress state is unaffected by a centered gap, whereas an increase up to 25% is predicted when the gap is sufficiently close to overlap ends. Chadegani et al. [33] analyzed the effect of voids and interfacial cracks in adhesively bonded joint employing the first-order shear

deformation plate theory. Analytical results showed a good agreement with Finite Element Analysis (FEA).

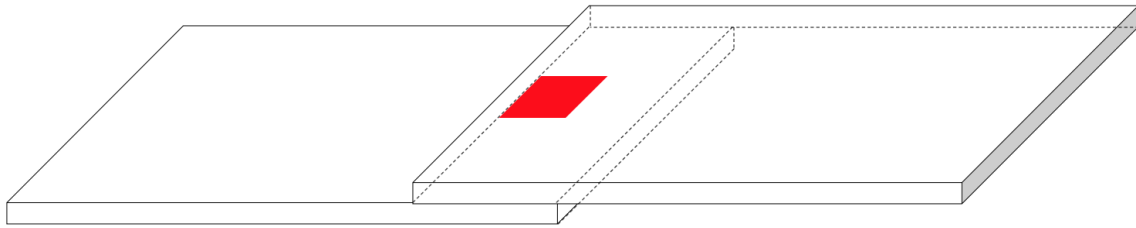
Beside theoretical models, numerical stress analyses of adhesively bonded joints have been carried out to assess the influence of defects, including non-linear material behavior and complex geometry. Ribeiro et al. [34] numerically evaluated the effect of different types of bondline defects, namely rectangular and circular, accounting for the influence of their position within the bondline. It was shown that the more the defect approaches to the ends of the overlap, the more the joint strength is negatively affected. Good agreement between numerical 3D models and experimental outcomes was found concerning ultimate failure loads for joints affected by defects. A numerical and experimental research was carried out by You et al. [35] to investigate the effect of different through-width gap lengths on the mechanical behavior of adhesively bonded double-lap joints. It was concluded that excluding the areas surrounding the gap, stress distribution was unaltered by small gaps. On the contrary, larger defects size strongly affected the load-carrying capability of the joint.

Further improvements in numerical modeling of bonded joints were achieved with the introduction of the Cohesive Zone Model (CZM), which stands out among all the approaches proposed to simulate the damage in the bondline [5]. A complete response of the joint, from damage initiation up to final failure, is enabled by CZM, which merges continuum mechanics concept and fracture mechanics approach. Typical mixed-mode fracture of adhesive joints is taken into account by CZM, by coupling tension and shear responses that occur in a real application scenario [36]. Riberio et al. [27] carried out numerical analyses of adhesively bonded joints by exploiting CZM to predict the influence of damage size on joint strength reduction, considering different type of adhesives. It was shown that the experimental characterization of adhesives mechanical properties is fundamental to calibrate CZM input parameters, which influence the evolution of the damage in the bondline. Good agreement with experimental outcomes was found, in particular, for a brittle adhesive.

All these works focused the attention on the reduction of the joint load-carrying capability resulting from the presence of defects. Nevertheless, defects were almost always considered as full strips of adhesive removed along the width of the joint, as shown in Figure 2.8a. This type of disbond does not represent a realistic scenario of manufacturing-induced defect [37]. Indeed, real structural joints are much wider than laboratory specimens, and they are affected by much smaller defects compared to the joint width, as illustrated in Figure 2.8b. Different behaviors are expected from an idealized through-width strip disbond and discrete defect.



(a) SLJ with through-width strip disbond.



(b) Wide SLJ with localized discrete defect.

Figure 2.8 Schematic illustration of bonded lap joints with different types of disbonds.

In the context of this thesis, the presence of defects within the joining line of wide boltless joints is extensively investigated by numerical simulation of artificial disbonds implemented in a FE model. In particular, defects are always located in the center of the overlap, never approaching the joint's free edges. The aim is to drive the damage propagation along the joint width, i.e. perpendicular to the applied load along the length direction, avoiding damage initiation at the free edges. Indeed, this represents a more realistic scenario for a full-size fuselage longitudinal joint, which is sufficiently wide and adequately supported by frames and stringer, which delays the propagation of damage at the edges.

Following this new point of view, the effect of localized discrete defects on the fatigue behavior of bonded joints has been experimentally investigated within the BOPACS project [7]. It aimed to investigate the potential use of design features, such as bolts, to slow down damage propagation under cyclic loading conditions. The crack stopping capabilities of fasteners was demonstrated through fatigue testing of WSLS joints affected by an initial rectangular artificial disbond embedded in the bondline. It was deemed with reasonable confidence that WSLS specimens could simulate a typical HLT joint, such as fuselage longitudinal joint [3]. Good fatigue performances of WSLS joints with and without crack arrestors resulted from the experimental investigations evaluated in terms of number of cycles to failure and damage growth.

Fatigue response of wide adhesively bonded joints affected by process-induced semi-circular defects was experimentally and numerically investigated by Liu et al. [37]. Crack growth was monitored by ultrasonic inspections every k -cycles, highlighting the different fatigue behavior of embedded cohesive disbond and artificial adhesive disbond. The latter presented a 40% reduction in fatigue life with respect to the former. In addition, fatigue lifetime predictions were proposed by exploiting fracture parameters evaluated through quasi-static numerical analysis and experimental fatigue crack growth data previously measured for the adhesive material.

In the context of this thesis, suitable methodologies for fatigue response predictions of bonded joints affected by manufacturing-induced defects are investigated by exploiting numerical outcomes of FE quasi-static analysis and available fatigue test results. In addition, since no experimental static or fatigue tests of longitudinal welded joints have been carried out yet, suggestions for future fatigue fracture testing and modeling validation are proposed for thermoplastic composites joints.

Chapter 3

Structural Analysis of Joining Line of SLJ

This Chapter delves into the principal behavioral characteristics of bonded SLJ, which is the type of joint configuration used nowadays for longitudinal fuselage joints. SLJ is commonly used in practice since it represents a good trade-off between simplicity of manufacturing and mechanical efficiency. Therefore, scientific investigations are mainly directed towards this type of joint.

Stress analysis plays a crucial role in the design of any structural components [38]. It provides an acceptable estimation of stress state in terms of magnitude and distribution, setting the basis for further improvement in structural design. Over the years, stress analysis of bonded SLJ has been carried out by either analytical models and numerical investigations. In this thesis, both methods are exploited to evaluate stress distribution in the joining line of boltless WSLJ joint configurations.

From a mechanical point of view, adhesively bonded joint and welded joints exhibit similar behavior [20]. The former is characterized by a thin layer of adhesive between two substrates, while the latter presents a thin film of polymeric matrix without any fibers reinforcement in the weldline. Either the bondline and the weldline show different mechanical properties compared to the adherends, and they represent the weak link of the joint. The studies presented in this thesis focus on the fracture behavior of the thin layer between the composite adherends when the joint is subjected to a prescribed loading scenario and boundary conditions. Hence, in the following Chapters, the adhesive layer plays the role of both bondline and weldline, and the heading bonded joint incorporates also welded joint.

3.1 Load Transfer Mechanism

A SLJ consists of an adhesive layer placed between two separate substrates called adherends. In a structural bonded joint, the adhesive's primary function is to transfer the load from one member to another. In order to ensure the transmission, the two adherends are overlapped, as shown in Figure 3.1.

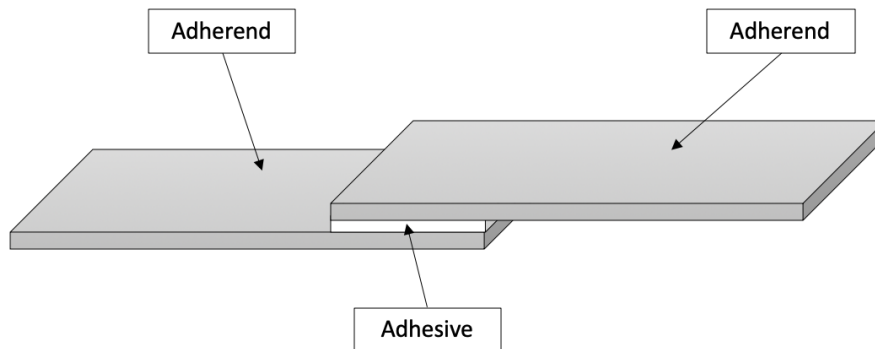


Figure 3.1 Schematic illustration of a SLJ.

Regardless of the loading scenario to which the joint is subjected to, the stress distribution in a structural bonded joint can be divided into a shear stress component τ , and a normal stress component σ , as shown in Figure 3.2. The former is caused by forces acting perpendicular to the structure, whereas the latter is induced by parallel forces [38]. In a SLJ subjected to axial tensile forces, the load transfer mechanism between the two adherends is ensured via shear distribution τ_{yz} in the adhesive layer.

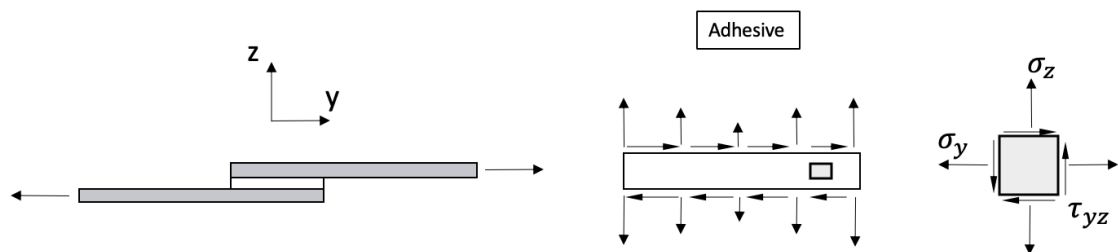


Figure 3.2 Formation of shear and normal stresses in the adhesive layer of a SLJ.

The load is gradually transmitted from the upper substrate to the lower one. In the upper adherend, this results in a stress reduction and, accordingly, strains γ , towards

the right end of the substrate, as illustrated in Figure 3.3. The distribution is reversed in the lower adherend. Since the adhesive and the adherends necessarily deform in a consistent way, this leads to shear stress concentrations at the edges of the bondline [39].

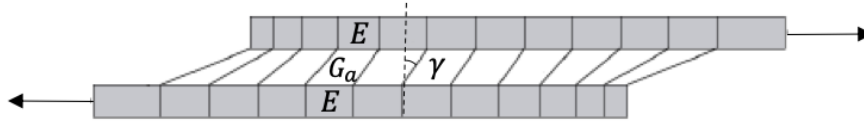


Figure 3.3 Adhesive layer shear deformation during the load transfer.

In addition, a secondary bending effect arises as a result of the eccentricity of the loading since the two adherends are not aligned, as illustrated in Figure 3.4. To counteract the bending moment in the adherends, through-thickness forces arise in the adhesive layer, which is the so-called peel stresses σ_z . They exhibit a change of direction along the bondline to ensure a self-balancing behavior.

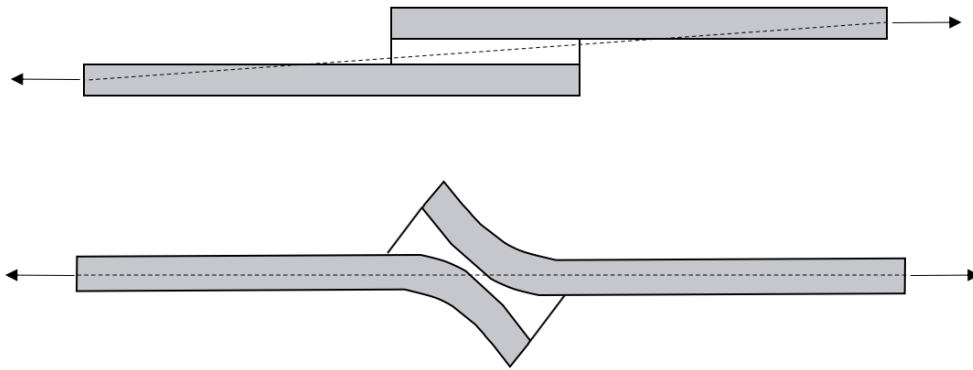


Figure 3.4 Illustration of secondary bending effect in SLJ, which causes the occurrence of peel stresses in the adhesive layer.

The last stress acting in the adhesive layer is the longitudinal direct stress σ_y , which is the result of the elongation of the joint subjected to a tensile load. Nevertheless, this stress is usually neglected because the tensile stress distribution in the adhesive layer is less critical compared to the adherends [40]. Indeed, since the adherends are usually characterized by a higher Young's modulus E , they deform less easily compared to the adhesive layer and exhibit higher σ_y [35].

Hence, the two main stress components that determine the boltless joint's behavior are shear and peel stresses that develop in the adhesive layer as a consequence of the applied load. Nevertheless, presence of disbond in the joining line prevents load transfer between the adherends, and an alternative transmission path needs to be found. In the following, a brief description of the theoretically expected structural behavior is given in terms of stress distributions for a pristine adhesive layer, which contains no defect, and for a damaged adhesive layer, with an initial disbonded area.

3.1.1 Pristine Joining Line

The pristine adhesive layer ensures a perfect adhesion between the two adherends. Hence, an ideal load transfer between the substrates can be achieved. Along the overlap length, the shear stress is expected to exhibit a relatively uniform distribution in the central section of the joining line, and an increase towards the overlap edges. Due to the simple overlapping configuration, peel stresses arise and peak at adhesive edges due to the load path eccentricity. This stress state is schematically illustrated in Figure 3.5.

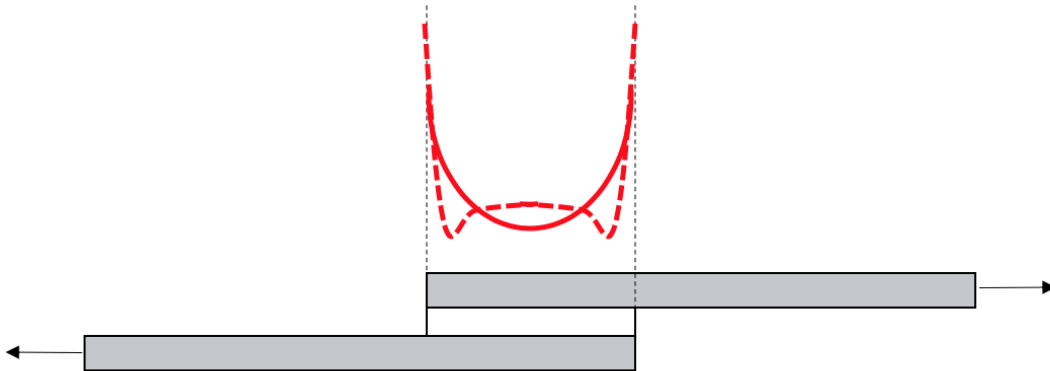


Figure 3.5 Stress distribution along the joining line of a pristine WSLS joint. Solid line illustrates shear distribution, and dashed line shows peel stress.

3.1.2 Damaged Joining Line

An alteration of the stress distribution along the joining line is expected due to the presence of defects, which interrupt the load transfer between the adherends. Consequently, adjacent alternative paths are used to transfer the load, leading to stress increases in the areas surrounding the damage. Principle behavior of a WSLS joint

characterized by an initial disbonded area in the joining line is schematically illustrated in Figure 3.6.

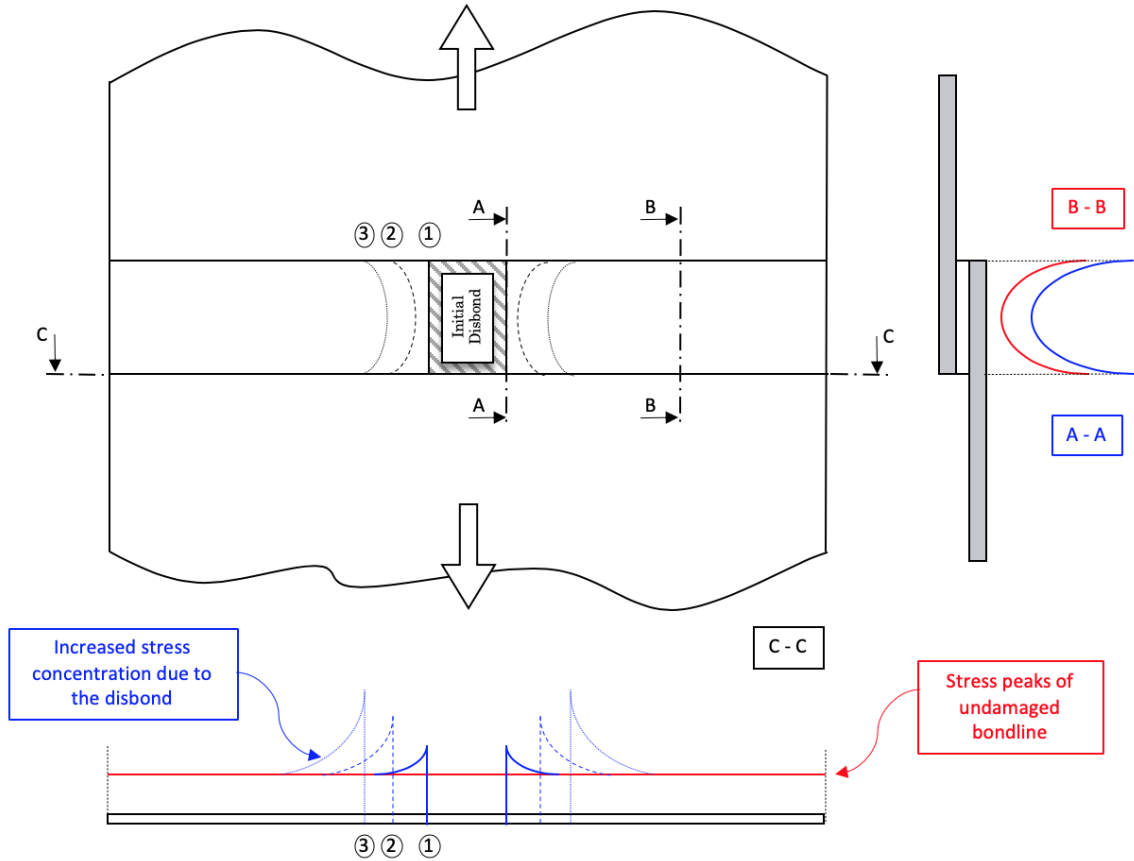


Figure 3.6 Principle behavior of stress distribution in a boltless WSLS joint affected by an initial disbonded area in the joining line. Adapted from [41].

The presence of a disbond markedly influences stress concentration at the overlap edges (see Figure 3.6, position 1). Either increasing the applied load or applying a cyclic loading affect the severity of stress peaks, causing an increase of the stress concentration at the disbond roots (see Figure 3.6, positions 2, and 3). This stress field triggers an early damage initiation and accelerates damage propagation in the joining line, finally leading to premature rupture of the joint.

On the contrary, the stress state in the undamaged bondline might or might not be affected by the damage's presence, depending on the joint width. For the purpose of this thesis, the joint has to be wide enough to ensure an unaltered stress state in the far-field compared to the healthy joining line of a pristine joint. This consideration is fundamental to guarantee a disbond propagation starting from the location of the

disbond in the center of the adhesive layer and perpendicularly to the applied load direction. Therefore, in the undamaged joining line, an increase in the stresses in the far-field is not desired to avoid damage initiation and propagation at the joint's free edges. Indeed, this would not occur in a full-size fuselage longitudinal joint where frames and stringers adequately support the skin.

3.2 Stress Distribution and Magnitude Evaluation

Stress analysis aims to provide reasonable and acceptable predictions in terms of magnitude and distribution of the stress field that develops in a given structure, considering specific loading scenarios and boundary conditions. In particular, stress analysis of boltless joints represents a complex engineering task because of inhomogeneous material interfaces, joint configuration, and non-linear behavior. Two main techniques can be selected to analyze this type of joints, namely analytical and numerical.

Many researchers proposed analytical analyses for determining the stress distribution of bonded joints. By exploiting force equilibrium and deformation compatibility, closed-form solutions derive from solving differential equations. All these theories are based on simplified assumptions concerning the structural behavior of the joint. On the other hand, numerical investigations are usually performed employing commercial FE software. They can provide an in-depth analysis of stress and strain distributions along with the possibility of handling complex geometry and non-linear material responses.

3.2.1 Analytical Analyses: Goland and Reissner Solution

Throughout the 20th century, many studies have been conducted on bonded joints to analyze their stress state. The choice of a proper analytical model to assess the behavior of the structure under examination is fundamental. Due to the complexity of bonded joints configuration, an exact solution to the problem is not available. Hence, in order to simplify the analysis, different approximate solutions have been proposed. In the following, a brief literature review of the existing analytical solutions for a SLJ configuration is presented.

In 1938, Volkersen [42] proposed a simplified model to study a mechanically fastened joint, assuming continuous properties for the fasteners in the longitudinal direction. Later on, this simple shear lag model was applied for the analysis of bonded joints along with the introduction of the *differential shear* concept. In this model, adhesive layer deforms in shear, whereas the adherends in tension. Nevertheless, this analysis

neglects the secondary bending effect due to the eccentricity of the load in a SLJ, and do not account for the peel stresses acting on the adhesive layer.

The analysis of Goland and Reissner (1944) [43] accounts for the eccentricity of the load path, and both shear and peel stress are predicted. A transverse force factor k' and a bending moment factor k were introduced to show the effect of the adherends large bending deformations. In this model, stresses are considered constant across the thickness of the adhesive layer.

In 1973, Hart-Smith [44] proposed an improvement to the classical approach of Goland and Reissner, including the adhesive plasticity in the analysis, and an alternative non-linear bending factor was proposed. In addition, individual deformation of the adherends is considered to straddle the bondline.

The previous theories represent the classical analytical models for determining the stress distribution in a SLJ. They neglect the stress variation across the adhesive layer and predict the shear peaks at the overlap ends. This is a violation of the free edge condition, which means a zero-shear condition at the free surfaces of the adhesive layer [35]. Allman (1977) [45] and Renton and Vinson (1977) [46] proposed two analyses that satisfy the free edge condition and provide a more plausible stress distribution within the adhesive layer.

Nevertheless, for the purpose of this thesis, the model of Goland and Reissner is selected as the analytical classic analysis method to evaluate stress distribution and magnitude in the adhesive layer of boltless joints. The reasons that led to this choice are explained in Section 3.2.2.

Assumptions

The analytical solutions proposed by Goland and Reissner is based on the following assumptions [35]:

- The SLJ problem is considered as two dimensional,
- The joint is subjected to axial tensile load, and the edges are simply supported,
- The joint is symmetrical with identical adherends,
- The width of the joint is large compared to the adherend thickness,
- All materials are linear elastic with homogeneous properties,
- No stress variation across the thickness of the adhesive layer is taken into account.

Analytical Solutions

Figure 3.7 and Table 3.1 provide a unified notation for the joint geometrical configuration, applied loads, and material properties.

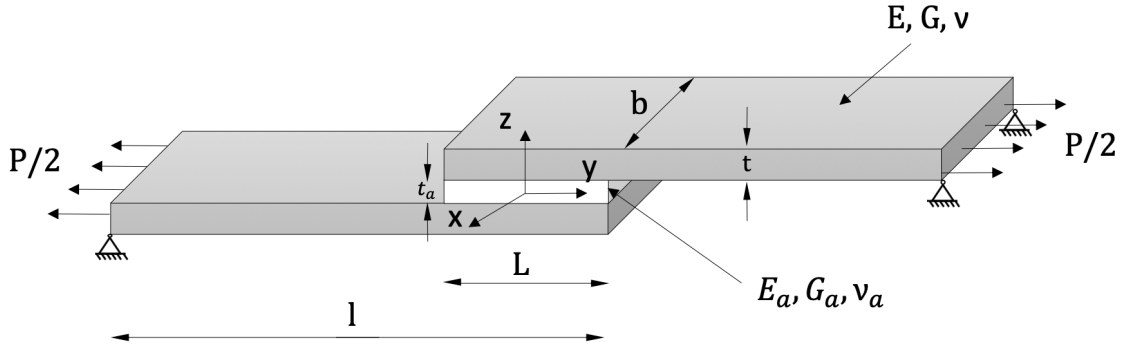


Figure 3.7 Geometrical configuration of the SLJ for analytical solutions.

Table 3.1 Unified notation for SLJ model.

Symbol	Declaration	Unit
P	Applied tensile load	N
\bar{P}	Applied tensile load per unit width	N/mm
L	Overlap length	mm
c	Half of the overlap length	mm
b	Adherends/Overlap width	mm
t	Adherends thickness	mm
t_a	Adhesive thickness	mm
E	Adherends Young's modulus	MPa
G	Adherends Shear modulus	MPa
ν	Adherends Poisson's ratio	-
E_a	Adhesive Young's modulus	MPa
G_a	Adhesive Shear modulus	MPa
ν_a	Adhesive Poisson's ratio	-

In the adhesive layer of a SLJ, the shear stress distribution τ proposed by Goland and Reissner can be expressed as follows:

$$\tau = -\frac{1}{8} \frac{\bar{P}}{c} \left\{ \frac{\beta c}{t} (1 + 3k) \frac{\cosh\left(\frac{\beta c x}{t}\right)}{\sinh\left(\frac{\beta c}{t}\right)} + 3(1 - k) \right\} \quad (3.1)$$

with

$$k = \frac{\cosh(u_2 c)}{\cosh(u_2 c) + 2\sqrt{2} \sinh(u_2 c)}$$

$$u_2 = \frac{1}{t} \sqrt{\frac{3(1 - \nu^2)}{2} \frac{\bar{P}}{tE}}$$

$$\beta^2 = 8 \frac{G_a t}{Et_a}$$

The distribution of peel stress σ in the adhesive layer is given by:

$$\sigma = \frac{1}{\Omega} \frac{\bar{P} t}{c^2} (A + B) \quad (3.2)$$

where

$$A = \left(R_2 \lambda^2 \frac{k}{2} + \lambda k' \cosh(\lambda) \cos(\lambda) \right) \cosh\left(\frac{\lambda x}{c}\right) \cos\left(\frac{\lambda x}{c}\right)$$

$$B = \left(R_1 \lambda^2 \frac{k}{2} + \lambda k' \sinh(\lambda) \sin(\lambda) \right) \sinh\left(\frac{\lambda x}{c}\right) \sin\left(\frac{\lambda x}{c}\right)$$

$$k' = \frac{k c}{t} \sqrt{3(1 - \nu^2) \frac{\bar{P}}{tE}}$$

$$\lambda = \gamma \frac{c}{t}$$

$$\gamma^4 = 6 \frac{E_a t}{Et_a}$$

$$\Omega = \frac{1}{2} (\sin(2\lambda) + \sinh(2\lambda))$$

The bending moment factor and the transverse force factor are k and k' , respectively. Indeed, Goland and Reissner's model takes into account the effect of the load eccentricity by introducing these non-linear factors that link the applied tensile load to the bending moment and the transverse force.

3.2.2 Finite Element Analysis

Finite Element Analysis (FEA) is a common technique applied in engineering sciences for structural components analysis and design. This methodology is based on the subdivision of complex structures into small regions, commonly called finite elements, characterized by supporting points, i.e. the nodes. Simplified form functions represent the deformed state of each node, and element deformation is calculated by nodal solutions interpolation. FEA allows modeling of components with complex geometrical features along with the possibility to account for non-linear material behavior. Nevertheless, by exploiting this numerical technique to evaluate the stress field in a structural component, it is fundamental to ensure that it calculates a sufficiently accurate approximation of nodes deformation concerning the selected type of elements and the mesh size.

In this thesis, numerical simulations of bonded and welded joints with pristine and damaged joining lines are performed to assess the influence of defects on the joint's overall performance. In particular, stress distribution within a pristine joining line can find a direct comparison with the analytical solutions. Therefore, to validate the FE model, described in Chapter 4, by proving that it calculates a sufficiently accurate adhesive stress state, analytical stress evaluations are compared to the numerical shear and peel stress distributions extrapolated from FEA. For this purpose, Goland and Reissner's method is selected as the analytical reference solution. Indeed, it is deemed that it provides the best correspondence with the numerical behavior of finite elements used for the adhesive layer modeling, described in Section 4.3. Firstly, the selected type of finite element assumes a uniform stress distribution across the thickness; hence free edge condition is not satisfied. Secondly, the material behavior of the adhesive is assumed to be elastic, followed by damage initiation and propagation; hence no plasticity is taken into account [47]. Results of this validation process are provided in Section 4.5.

Chapter 4

Finite Element Modeling of Wide Single Lap Shear joint

This Chapter describes the numerical modeling exploited for the simulation of a Wide Single Lap Shear (WSLS) joint, which is selected as reference design of a fuselage longitudinal joint. The baseline model consists of two laminated composite panels joined together by a thin layer of adhesive. It simulates either the bondline of an adhesively bonded joint and the weldline of a welded joint. These studies mainly focus on debonding failure between the adhesive layer and substrates, namely cohesive failure. Hence, the proposed model does not account for failure modes of composite adherends, such as intralaminar and interlaminar failures. Quasi-static non-linear analysis of WSLS joints aims to assess the damage spreading behavior in the adhesive layer up to failure, and to evaluate how the overall performance of the joint is affected by the presence of disbond in the joining line.

4.1 Numerical Simulation Tools

Table 4.1 summarizes the equipment and the tools available for the numerical investigations in terms of software and hardware. Within the scope of this thesis, Abaqus FEA is employed as modeling software. In particular, the first stage of modeling, or *pre-processing*, is carried out through Abaqus/CAE. The actual finite element analysis, or *processing*, is performed by Abaqus/Explicit. Finally, the output results are visualized through Abaqus/CAE for the final *post-processing* stage. The Explicit solver has been selected over the implicit method to simulate quasi-static analysis. Indeed, Abaqus/Explicit shows a considerable saving in computational cost when the model size increases and requires a smaller memory usage than implicit analysis. In order

to obtain a proper static response, appropriate adjustments of the required time have been accounted for, based on the lowest natural frequency of the structure [47].

A laptop was available for modeling and output data analysis. In addition, in order to handle large calculations due to the analyzed structure, the use of High Performance Computing (HPC) clusters provided by Airbus is enabled.

Table 4.1 List of software and hardware used for the numerical investigation.

Software and Hardware	
Pre-processing	Abaqus/CAE
Processing	Abaqus/Explicit
Post-processing	Abaqus/CAE
Abaqus/CAE Version	2016
Laptop	HP ZBook 17 G3

4.2 Laminated Composite Adherends

Continuum shell elements are used to model the laminated composite adherends because of their ability to discretize a whole 3D body in which one dimension, i.e. adherend thickness, is considerably smaller than the other dimensions, i.e. adherend length and width. In Abaqus Reference Guide [47], these elements are classified as general-purpose shells. They are suitable for non-linear geometrical analysis since they account for finite membrane deformation and allow large rotations.

Composite laminates consist of different plies, and each of them is characterized by unique thickness and material orientation. For continuum shell elements, a single element that includes multiple plies is defined across the thickness. Then, for each ply, material properties, fiber orientation, thickness, and stacking sequence is defined.

In the context of this thesis, numerical investigations focus on two different laminated composite materials, namely thermosetting- and thermoplastic-based. Thermosetting-based composite adherends model the substrates of an adhesively bonded joint, and the selected material is a carbon-epoxy prepreg named Hexcel 8552/IM7. Thermoplastic-based laminated composites simulate the adherends of a welded joint, and the material used is a carbon-polyetherketoneketone prepreg named PEKK-HTS45. Thermoset and thermoplastic composites have different lamina mechanical properties, plies thickness, and layup stacking sequences. Tables 4.2 and 4.3 provide a summary of both geometrical

and mechanical input parameters used for the definition in the FE model of thermoset and thermoplastic adherends, respectively.

Table 4.2 Input parameters for thermosetting-based laminated composite adherend.

Hexcel 8552/IM7	Property	Value	Unit
Geometrical Parameters	l	500	mm
	b	500	mm
	t	2	mm
Lamina Properties	t_l	0.125	mm
	E_1	164	GPa
	E_2	12	GPa
	ν_{12}	0.32	-
	G_{12}	4.69	GPa
	G_{13}	4.69	GPa
	G_{23}	4.69	GPa
Layup Sequence	[45/90/135/0] _{2s}		

Table 4.3 Input parameters for thermoplastic-based laminated composite adherend.

PEKK-HTS45	Property	Value	Unit
Geometrical Parameters	l	500	mm
	b	500	mm
	t	2.208	mm
Lamina Properties	t_l	0.184	mm
	E_1	125	GPa
	E_2	9.2	GPa
	ν_{12}	0.35	-
	G_{12}	4.34	GPa
	G_{13}	4.34	GPa
	G_{23}	4.34	GPa
Layup Sequence	[45/135/90/0/135/45] _s		

4.3 Bondline and Weldline

Numerical modeling of the thin layer between the adherends is based on the implementation of the Cohesive Zone Model (CZM), which represents the most widespread FE modeling technique used for bonded joints [48]. It is considered the most accepted approach to model the damage behavior of adhesive layers, which is the main interest of these studies.

CZM is based on both continuum mechanics concept and fracture mechanics approach. From the continuum approach, it inherits the use of stresses, which are subsequently exploited in the CZM to establish whether or not the damage initiates. On the contrary, the damage propagation is driven by energetic principles like in fracture mechanics [48]. Hence, the special-purpose cohesive elements are used to model the bondline in adhesively bonded joints and the weldline of welded joints.

In order to fully describe the behavior of cohesive elements, the mechanical constitutive response of the adhesive in the bondline and the polymer matrix in the weldline has to be specified. Depending on the specific application, Abaqus/CAE offers three different methods to describe cohesive behavior [47]. The most suitable modeling approach for bonded interfaces is based on the definition of the traction-separation law. It models the initial loading, the subsequent damage initiation, and the final damage evolution, which leads to the failure of the thin layer between the adherends. This approach fully describes the expected behavior of WSLs joints, and in the following, a detailed description of this model is introduced.

4.3.1 Constitutive Response: Traction - Separation Law

Defining the constitutive response of cohesive elements directly in terms of traction-separation law is especially addressed for bonded interfaces separated by a negligible thickness [47]. The traction-separation law provides a relationship between stresses and displacements of cohesive elements. An initial linear elastic behavior is enabled up to damage initiation, and it is followed by a linear softening of mechanical properties to simulate the damage propagation up to total failure. This response is also defined as bi-linear traction-separation law, and an example is illustrated in Figure 4.1. The area underneath the traction-separation law corresponds to the critical fracture energy G^c , which is dissipated during failure.

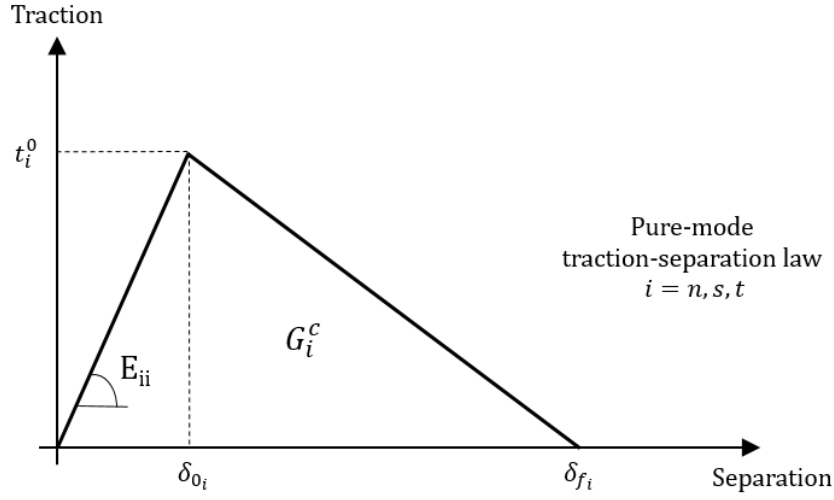


Figure 4.1 Typical traction-separation law for a pure-mode constitutive response.

An elastic constitutive matrix \mathbf{E} is the link between strain $\boldsymbol{\varepsilon}$ and stress \mathbf{t} vectors. Considering an uncoupled behavior, the stress-strain relation can be expressed as follows [47]:

$$\mathbf{t} = \begin{Bmatrix} t_n \\ t_s \\ t_t \end{Bmatrix} = \begin{bmatrix} E_{nn} & & \\ & E_{ss} & \\ & & E_{tt} \end{bmatrix} \begin{Bmatrix} \varepsilon_n \\ \varepsilon_s \\ \varepsilon_t \end{Bmatrix} = \mathbf{E}\boldsymbol{\varepsilon} \quad (4.1)$$

where the subscripts n , s , and t refer to normal, longitudinal shear, and transverse shear direction, respectively. Strains are defined as the ratio between the relative displacement of faces and initial thickness. A default unitary value is set for the thickness to ensure a direct correspondence between strain and displacement. Therefore, interface thickness has to be taken into account in the definition of elastic constitutive parameters [47]. After reaching a certain stress state condition, damage initiates in the cohesive element.

Damage initiation

Damage initiation represents the starting point of the degradation process of mechanical properties. It begins when a specific damage initiation criterion is satisfied, and in this thesis, the quadratic nominal stress criterion is selected. This criterion can be expressed as [47]:

$$\left\{ \frac{\langle t_n \rangle}{t_n^0} \right\}^2 + \left\{ \frac{t_s}{t_s^0} \right\}^2 + \left\{ \frac{t_t}{t_t^0} \right\}^2 = 1 \quad (4.2)$$

t_n^0 , t_s^0 , and t_t^0 refer to maximum traction stresses in case of deformation in purely normal, longitudinal shear and transverse shear directions, respectively, and represent the interfacial strengths. Macaulay brackets $\langle \rangle$ indicated that a purely compressive stress state does not initiate damage, but only tensile stress contributes to damage initiation.

Damage evolution

After meeting the damage initiation criterion, material stiffness is linearly reduced to zero according to a specific law. Damage propagation law has to account for the mode mix of the deformation state, which defines the relative weight between shear and normal deformation [47]. An example of mixed-mode response is provided in Figure 4.2.

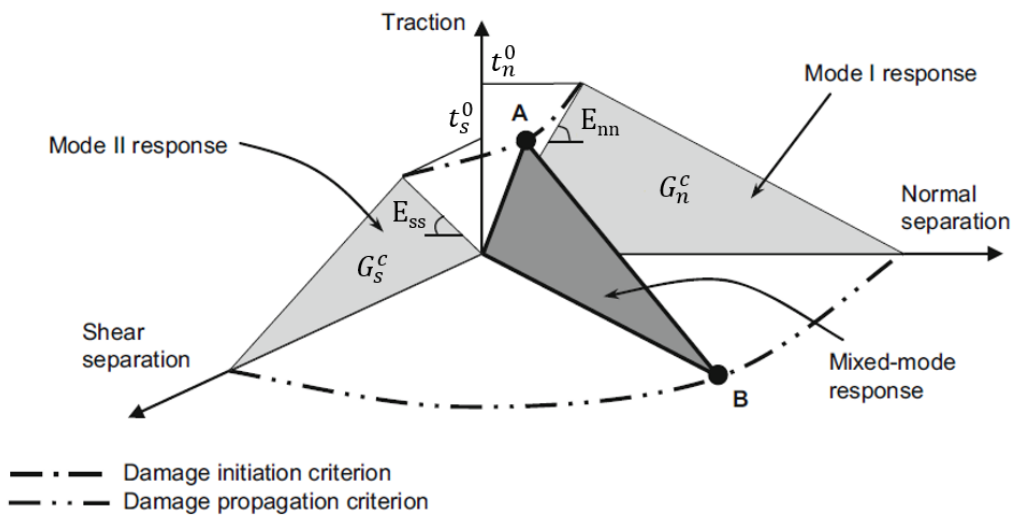


Figure 4.2 Schematic illustration of mixed-mode response for cohesive elements.

In the context of this thesis, the mixed-mode behavior is based on energy evaluations. Two different definitions are used to describe the mode mix, depending on the material under examination:

- Benzeggagh-Kenane (B-K) form, which provides an analytical description between fracture energy G^c and mix mode ratio MMR . This criterion is particularly suitable when the same critical fracture energy is required for purely deformation in the longitudinal and transverse shear direction, i.e. G_s^c and G_t^c respectively

[47]. B-K law is defined as follows:

$$G_n^c + (G_s^c - G_n^c)(MMR)^\eta = G^c \quad (4.3)$$

$$MMR = \frac{G_S}{G_T} \quad (4.4)$$

where $G_S = G_s + G_t$, $G_T = G_n + G_S$, and η is a material parameter.

- Tabular form, in which the dependency between the fracture energy and MMR is directly provided as a table [47].

4.3.2 Input Parameters for Cohesive Elements

In the context of this thesis, the numerical investigations for WSLs bonded joints are carried out considering two different types of adhesive, namely Loctite EA 9395 and Scotch Weld 9323-B/A, which exhibit completely different behavior. On the contrary, for WSLs welded joints, the cohesive elements model the PEKK polymer matrix used for the composite adherends. Table 4.4 is a summary of the geometrical parameters for the cohesive layer. Tables 4.5, 4.6 and 4.7 provide a summary of input parameters used for the definition of cohesive elements in the FE model for Loctite EA 9395 adhesive, Scotch Weld 9323-B/A adhesive, and PEKK polymer matrix, respectively.

Table 4.4 Geometrical dimensions of the cohesive layer.

Symbol	Value	Unit
L	60	mm
b	500	mm
t_a	0.1	mm

Table 4.5 Input parameters for Loctite EA 9395 adhesive.

Loctite EA 9395	Property	Value	Unit
Elastic Properties	E_{nn}	2577	MPa
	E_{ss}	976	MPa
	E_{tt}	976	MPa
Damage Initiation	t_n^0	59	MPa
	t_s^0	44.68	MPa
	t_t^0	44.68	MPa
		MMR	G^c [N/mm]
Damage Evolution		0	1.01852
		0.2	0.93578
		0.6	1.6068
		0.85	3.44714
		1	0.78341

Table 4.6 Input parameters for Scotch Weld 9323-B/A adhesive.

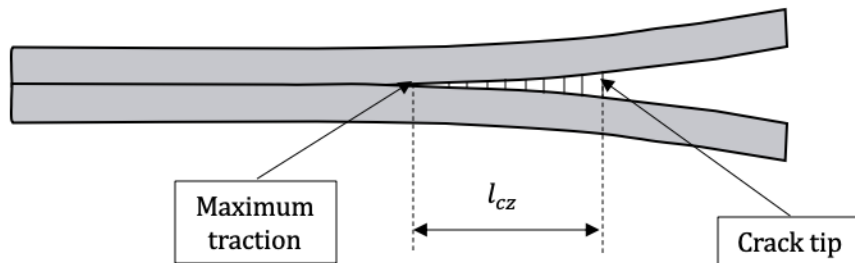
Scotch Weld 9323-B/A	Property	Value	Unit
Elastic Properties	E_{nn}	2110	MPa
	E_{ss}	460.5	MPa
	E_{tt}	460.5	MPa
Damage Initiation	t_n^0	21.9	MPa
	t_s^0	24.2	MPa
	t_t^0	24.2	MPa
Damage Evolution: B-K	G_n^c	0.449	N/mm
	G_s^c	7.53	N/mm
	G_t^c	7.53	N/mm
	η	1.35	-

Table 4.7 Input parameters for PEKK polymer matrix.

PEKK matrix	Property	Value	Unit
Elastic Properties	E_{nn}	4000	MPa
	E_{ss}	1500	MPa
	E_{tt}	1500	MPa
Damage Initiation	t_n^0	25	MPa
	t_s^0	60	MPa
	t_t^0	60	MPa
Damage Evolution: B-K	G_n^c	1.2	N/mm
	G_s^c	2.4	N/mm
	G_t^c	2.4	N/mm
	η	1	-

4.3.3 Influence of mesh size

A single layer of cohesive elements across the thickness is used to discretize either the bondline and the weldline, in order to produce accurate results according to Abaqus Reference Guide [47]. Nevertheless, to ensure successful numerical modeling of cohesive elements, appropriate elements mesh size has to be adopted. Indeed, the size of each finite cohesive element needs to be smaller than the cohesive zone length. As discussed in Section 4.3.1, damage initiation is reached when a specific criterion, expressed in terms of normal and shear maximum tractions, is fulfilled. Then, damage propagates if the critical fracture energy G^c is reached. According to Turon et al. [49], the distance between the crack tip and the location of maximum stress determines the length of the cohesive zone l_{cz} , as shown in Figure 4.3.

**Figure 4.3** Length of cohesive zone.

Many studies have been carried out about the definition of l_{cz} , and a widespread expression to estimate it is given as follows [49]:

$$l_{cz} = ME \frac{G^c}{(t^0)^2} \quad (4.5)$$

where E is the Young's modulus of the material, t^0 is the maximum interfacial strength of the material, and G^c is the related fracture toughness. M is a characteristic parameter of the model under examination. In Hillerborg's model [50], the parameter M is exactly equal to unity, and it represents the most adopted choice in the literature. Hence, in the following, M is considered to be one.

In addition, a proper number of elements N_e in the cohesive zone is required in order to ensure a correct representation of the fracture energy. The minimum required N_e is not well defined, and it may vary depending on specific models. According to Turon et al. [49], three elements in the cohesive zone can be considered sufficient. The required mesh size l_e in the crack propagation direction can be calculated as follows:

$$l_e = \frac{l_{cz}}{N_e} \quad (4.6)$$

Hence, for each data set of cohesive elements described in Section 4.3.2, the minimum mesh size required for the numerical modeling is calculated according to Eq. 4.6.

4.4 Constraints and Boundary Conditions

In order to simulate the adhesion between the adhesive layer and substrates, surface-based tie constraints are defined between cohesive elements and neighboring adherends interfaces [47].

To faithfully simulate a realistic test set-up, fully clamped boundary conditions are applied at one edge of the model to simulate the clamping of the tensile machine crosshead. Instead, at the opposite end of the specimen all transverse degrees of freedom are restrained except for the displacement in the loading direction. Figure 4.4 schematically illustrates the boundary conditions previously described in a 2D model.

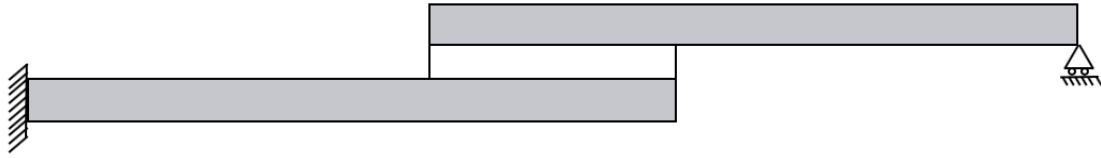


Figure 4.4 Schematic 2D illustration of the applied boundary conditions.

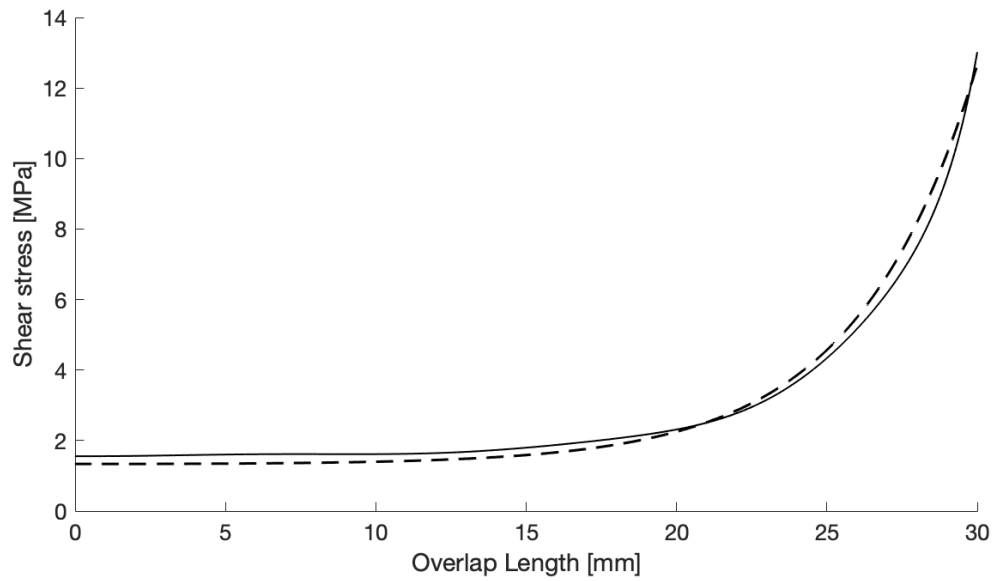
4.5 Validation of the FE WSLS reference design

In order to validate the numerical model of WSLS reference design, shear and peel stress distributions in the cohesive layer are compared with the analytical solutions proposed by Goland and Reissner described in Section 3.2.1.

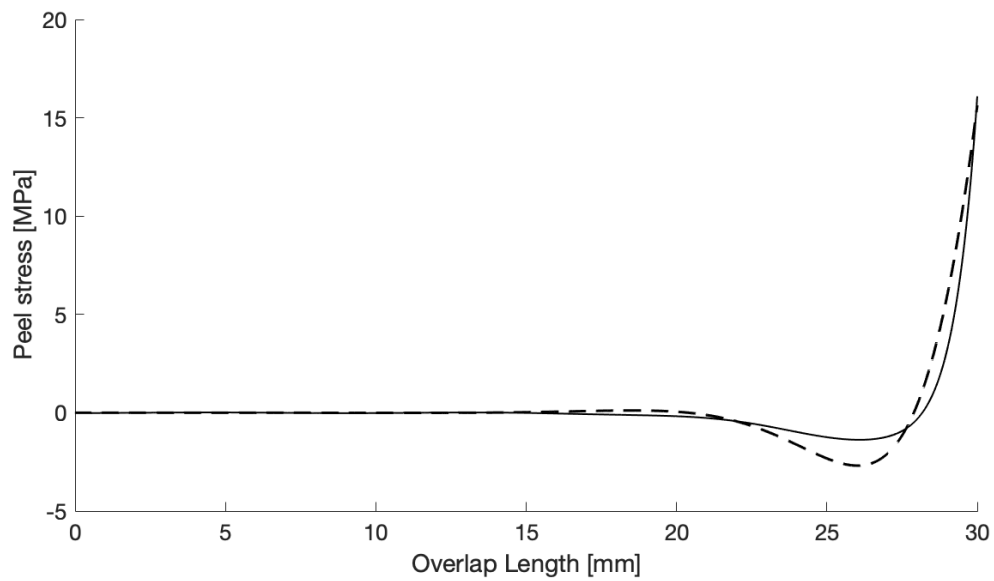
Figure 4.5 illustrates the stress state in the cohesive layer obtained by FE analysis compared with the analytical investigations. In general, both shear and peel stress distributions show a quite good agreement with Goland and Reissner's predictions. Concerning the shear distribution, a slight deviation from the theoretical stress is found in the central region of the overlap length, as shown in Figure 4.5a. Peel stress distribution (see Figure 4.5b) exhibits a deviation from the analytical solution in the compressive region towards the edges of the overlap. Table 4.8 provides the values of the maximum shear and peel stresses for both analytical and numerical investigations, and the percentage difference between the two methods is only about 3%. Hence, it is deemed that the FE WSLS reference model provides a sufficiently accurate stress state in the cohesive layer, representing a suitable way to predict the joint's real behavior.

Table 4.8 Summary of maximum shear and peel stresses in the adhesive layer predicted by Goland and Reissner analytical analysis and the proposed FE model.

	Shear stress [MPa]	Peel stress [MPa]
Goland and Reissner	12.66	15.63
FEA	13.02	16.12



(a) Shear stress distribution in the adhesive layer.



(b) Peel stress distribution in the adhesive layer.

Figure 4.5 Comparison between analytical (dashed line) and numerical (solid line) shear and peel stress distribution in the adhesive layer. Only one half of the overlap length is illustrated due to symmetry reasons.

Chapter 5

Methodology

This Chapter delves into the methodologies and approaches exploited to numerically assess the effect of defects in the joining line of adhesively bonded and welded joints. Although boltless configurations enable a more lightweight structural design, their application for primary aerospace structure is still limited due to difficulties in evaluating the joining quality after manufacturing [3].

In this thesis, numerical outcomes obtained through FE quasi-static analysis are exploited to investigate the influence of several disbond sizes on the load-carrying capability of bonded and welded WSLS joints. Different behaviors are expected, depending on the properties of the material used to simulate the joining line. Two methodological approaches are proposed to predict the effect of disbonds on the fatigue response of bonded joints, by combining numerical results extrapolated from FE analysis and available experimental data from fatigue testing.

5.1 WSLS Joint Strength Analysis

The presence of defects in the joining line of bonded and welded joints, due to poor-quality interface treatment or inaccurate process parameters, can dramatically affect the mechanical behavior of the joint by leading to bond strength reduction. Hence, it is necessary to determine and quantify this effect by predicting the residual strength of initially damaged joints.

Disbonds prevent load transfer between the adherends. Therefore, forces find an alternative transmission path, i.e. by converging towards the closest healthy portion of the joining line, compensating for the lack of adhesion between adhesive and substrate at the defect location. As a result, stresses increase in the areas surrounding the damage, locally causing higher stress peaks, which are responsible for the joint's strength

reduction. Therefore, it is fundamental to evaluate how sensitive the structural joint is to the presence of damages, in order to assess whether the damaged configuration is still able to perform its tasks, or whether proper repair or replacement is necessary.

A comparative static strength analysis is proposed to investigate the effect of disbonds in the joining line on the fracture behavior of WSLS joints. The attention is focused on the influence of both disbond size and different mechanical properties of the joining line. A suitable FE model of WSLS joint is developed using Abaqus/CAE, as described in Chapter 4. Quasi-static non-linear analyses are numerically performed to evaluate the joint strength reduction systematically.

5.1.1 Influence of disbond size

Many studies have been carried out on the influence of removing an adhesive strip along the width of bonded joints. It is well-established that the closer the strip is to overlap edges, the more the joint's behavior is negatively affected. Indeed, in a simply overlapped joint, stress peaks concentrate towards joining line edges, and a more severe strength reduction is expected in this scenario.

The proposed numerical investigations deal instead with a discrete squared edges disbond located in the center of the joining line of a WSLS joint. To account for the worst-case scenario, at least one edge of the defect always approaches the overlap ends. The main focus of the study is the influence on the joint's behavior of damage dimensions, namely the length and the width, as illustrated in Figure 5.1. Hence, a parametric comparative study is carried out to assess and quantify, in terms of strength reduction, the influence of both damage width increase with a fixed damage length and vice versa.

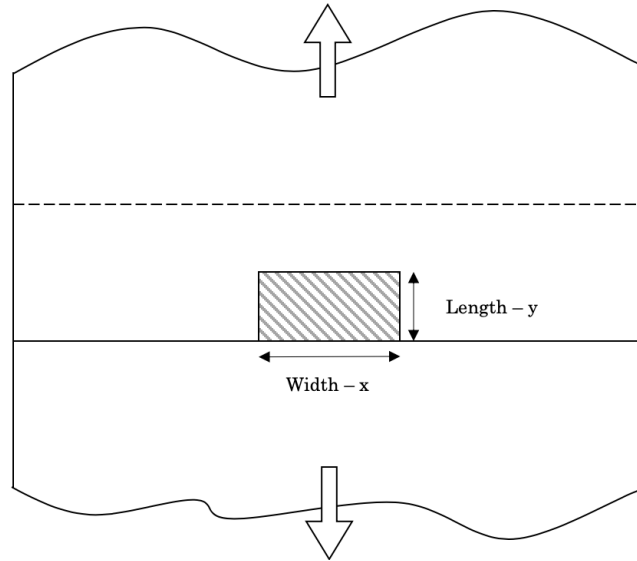


Figure 5.1 Schematic illustration of a squared edges disbond located in the center of the joining line, with one of its edge always approaching the overlap edge. Disbond length and width are instead adjusted for investigative purposes.

5.1.2 Influence of joining line mechanical properties

Stress distribution assumes a key role in the mechanical behavior of a joint. The strength reduction of an initially damaged joint strongly depends on how a specific adhesive layer handles stress increases due to the presence of damage. Three different types of overlapping materials are subjected to numerical analyses to assess the influence of their mechanical properties on the fracture behavior of WSLs joints. For thermosetting-based composites bonded joints, two adhesives are investigated, namely EA 9395, which shows a brittle behavior, and Scotch Weld 9323-B/A, which exhibits, on the contrary, more ductile characteristics. For thermoplastic welded joints, a thin layer of pure PEKK polymer matrix simulates the joining line. It is deemed that damages induce different stress redistribution within the overlap area, depending on the material under examination.

5.2 Fatigue Strength and Lifetime Analysis

In real-life applications, many structural components are subjected to a cyclic loading scenario. Continuous application of stresses leads to the weakening of materials, which may undergo a progressive damage evolution up to final structural integrity loss. This

phenomenon is called fatigue, and it undoubtedly represents the most common cause of structural failure [51]. When subjected to a fatigue loading scenario, a structural component may fail at loads far smaller than those experienced during quasi-static failure. Hence, fatigue behavior has to be taken into account during the design phase for structural members exposed to cyclic loading conditions during their in-service life. However, assessment of fatigue analysis and predictive methods represent one of the major challenges for the scientific engineering community.

In particular, dealing with bonded and welded joints of composite adherends implies an additional complication due to the coexistence of different materials interface. However, boltless joints generally exhibit a higher fatigue resistance than classical joining techniques, such as mechanical fastening [51], because there are no additional stress concentrations. Therefore, extensive research efforts need to be focused on predicting the fatigue response of this type of joints.

A crucial step towards a more comprehensive understanding of boltless joints fatigue behavior is the collection of experimental data. Afterward, predictive models can be proposed based on experimental results and exploited for fatigue response predictions [52]. Indeed, testing is often expensive in terms of cost and time, and predictive numerical models may assist engineers in designing structural components, reducing experimental effort.

In general, literature proposes two major models for fatigue analysis and lifetime predictions of boltless joints, namely the Stress-life approach and the Fatigue Crack Growth (FCG) approach [52]. The Stress-life approach usually aims to design structural components that are meant to survive a fixed in-service time before replacement. This methodology strongly relies on experimental testing of the component subjected to different levels of cyclic loading. Experimental data are used to build Wöhler's curve, i.e. the plot of the applied load versus the number of cycles to failure. In FCG approach, the structural components are assumed to be affected by an inherent defect since the beginning of their in-service life. This method aims to understand and quantify the rate at which the crack will grow by identifying its relationship with specific material properties.

The purpose of this thesis is to evaluate whether or not predictions on fatigue behavior of structural joint can be carried out by only means of numerical quasi-static simulations, e.g. by analyzing the stress state distribution in the joining line. Therefore, outcomes of numerical investigations are exploited to propose predictions of WSLS joints fatigue response when an initial disbond is present in the joining line. As previously explained, some experimental data are needed to fit reality into a numerical

model. Therefore, since no experimental data are available for the thermoplastic WSLs welded joint, the following Sections only deal with adhesively bonded joints.

Experimental Fatigue Spectra

Rather complex fatigue spectra may affect structural components in a real in-service scenario. Nonetheless, during experimental investigations, fatigue is usually defined in terms of a sinusoidal curve with a constant amplitude, as shown in Figure 5.2.

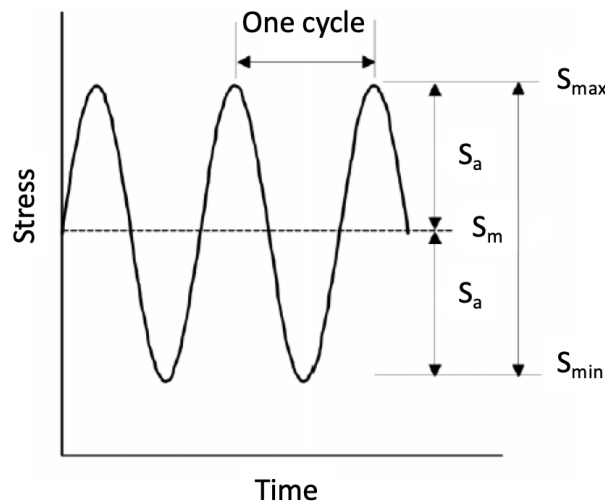


Figure 5.2 Schematic illustration of a sinusoidal fatigue spectrum used for laboratory investigations.

To describe the fatigue spectrum, some parameters are required:

- Maximum stress: S_{max}
- Minimum stress: S_{min}
- Mean stress: $S_m = (S_{max} + S_{min})/2$
- Stress amplitude: $S_a = (S_{max} - S_{min})/2$
- Stress ratio: $R = S_{max}/S_{min}$

To fully characterize a constant amplitude fatigue spectrum, only two of the previous parameters are necessary, in addition to the frequency f . Since adhesively bonded joints are mainly employed in tension loading scenarios, experimental setup usually

involves positive mean stress and R ratio greater than zero, generally between 0.1 and 0.5 [15].

In the following Sections, stress parameters will be consistently mentioned according to the presented nomenclature to describe the proposed methodologies.

5.2.1 Stress-life Approach

The stress-life approach aims to characterize fatigue behavior through the Wöhler's curve, also known as the $S - N$ curve. It is derived from experimental tests of pristine structural components that undergo a constant amplitude cyclic load until complete failure for different load levels. Figure 5.3 provides an example of a typical $S - N$ curve.

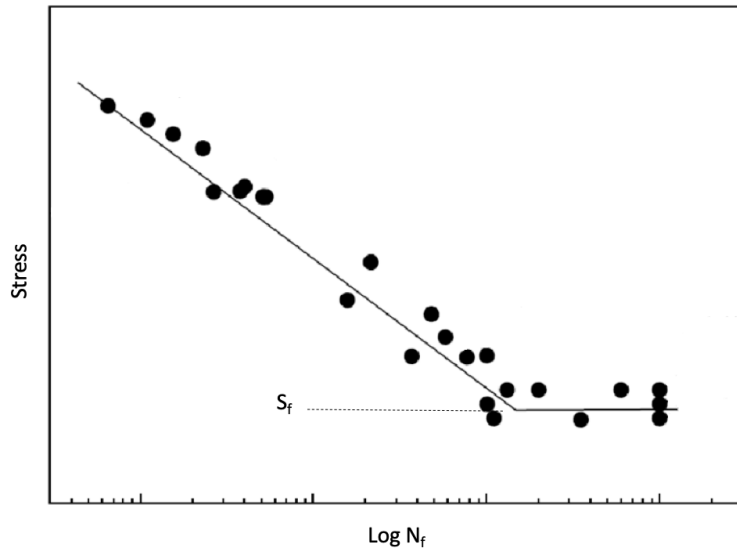


Figure 5.3 Schematic example of a typical Wöhler's curve. Adapted from [53].

The stress S may refer to nominal stress, stress amplitude, or average stress. For adhesively bonded joints, it is a common practice to use as stress reference the ratio between the applied load and the total bonded area [15]. The number of cycles to failure N_f is usually plotted in a logarithmic scale. Increased fatigue life is expected for lower stress levels. For a high number of cycles, almost infinite fatigue life is reached for an asymptotic value of stress S_f , which usually represents the fatigue, or endurance, limit. For adhesively bonded joints, this limit generally varies between 15% and 40% of the joint's static strength. [15, 54, 55].

The $S - N$ curves are a useful tool to predict component life up to failure, but also expensive in terms of experimental data requested. Moreover, it would be impracticable to apply this method to examine the influence of several loading parameters on fatigue life. Indeed, experimental investigations should be repeated for any other loading spectrum. Therefore, experimental outcomes of primary loading conditions, such as constant amplitude fatigue spectrum, are exploited to appropriately model and predict fatigue behavior under different cyclic loading scenarios [52].

Well-known predictive tools are the Constant Life Diagrams (CLDs), which enable fatigue assessment of structural components in different loading conditions for which no experimental tests have been carried out. CLDs illustrate the combined effect of stress amplitude and mean stress on the examined structural component, for a fixed fatigue lifetime. These diagrams are drawn starting from all the available test results for a fixed N_f , as illustrated in Figure 5.4. Two stress parameters uniquely identify each point on the $S - N$ curve, for instance, stress amplitude and mean stress, from which all the others can be derived, using mathematical formulations provided in Section 5.2.

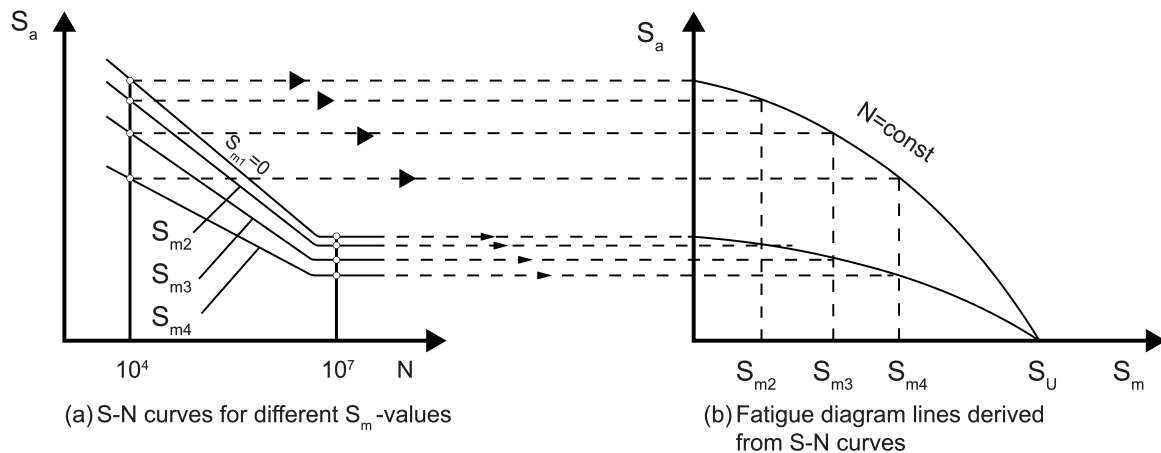


Figure 5.4 Schematic example of CLDs as cross plot from $S - N$ curves. Adapted from [56].

In literature, two simple equations have been proposed to fit CLDs, namely a linear approximation or a parabolic one. The former is commonly known as *Goodman equation*, whereas the latter as *Gerber parabola*, and they can be expressed

as follows [15]:

$$\text{Goodman equation: } \frac{S_a}{\bar{S}_a} + \frac{S_m}{S_u} = 1 \quad (5.1)$$

$$\text{Gerber parabola: } \frac{S_a}{\bar{S}_a} + \left(\frac{S_m}{S_u}\right)^2 = 1 \quad (5.2)$$

where \bar{S}_a is the value of stress amplitude for mean stress equals to zero, which means $R = -1$, and S_u is the ultimate strength of the structural component. Indeed, as shown in Figure 5.4, all CLDs converge towards S_u . This commonly accepted simplified assumption is due to the lack of knowledge about fatigue response when stress amplitude is zero. This loading condition cannot be defined as a cyclic loading scenario, but it rather consists of a constant static load applied to structural members over a short or long period of time, which is also known as creep [52].

CLDs are usually used to assess the effect of different R ratios and mean stresses on the fatigue life estimation of structural components. Nonetheless, in this thesis, CLDs formulations are exploited as a predictive tool for maximum fatigue strength assessment of WSLS bonded joints affected by different initial disbonds. The Similarity Principle for notched and unnotched components is used as a guideline for the proposed methodology, which allows basic fatigue prediction by only exploiting FE quasi-static numerical investigations.

Proposed methodology for fatigue limits predictions: Similarity Principle

Wöhler's curves refer to specific fatigue test setup of pristine structural components, i.e. in which no defects are intentionally produced. Nonetheless, real structures are affected by the presence of some irregularities, commonly identified as stress raisers, such as notches, holes, or corners. They induce stress redistribution in the remaining structure, with particular high stress peaks at the root of the damage [56]. This stress field allows an expansion of the applicability domain of specific fatigue test data employing the Similarity Principle between notched and unnotched specimens, as illustrated in Figure 5.5.

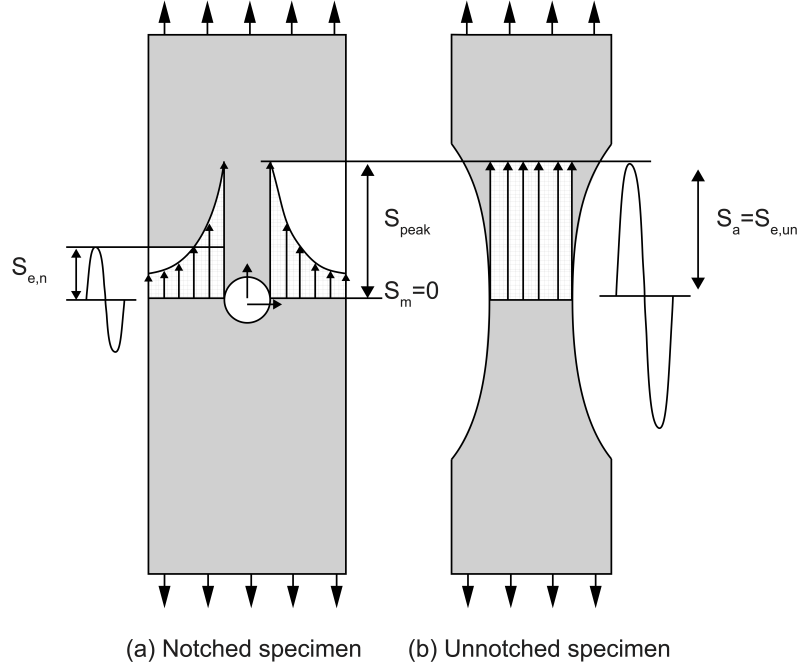


Figure 5.5 Schematic illustration of the Similarity Principle between notched and unnotched specimens, for $S_m = 0$. Adapted from [56].

Assuming that a microcrack is induced in the unnotched specimen when subjected to a cycle characterized by a stress amplitude S_a , and $S_m = 0$, the same cycle that causes a stress peak S_{peak} in the notched configuration should also induce a microcrack at the notch roots. Therefore, if S_a represents the fatigue strength $S_{e,un}$ for the unnotched specimen, in the notched configuration S_{peak} is reached when its fatigue strength $S_{e,n}$ is applied [56]. The application of the Similarity Principle leads to the following relations:

$$S_{peak} = K_t S_{e,n} = S_{e,un} \longrightarrow S_{e,n} = \frac{S_{e,un}}{K_t} \quad (5.3)$$

where K_t is the stress concentration factor, defined as the ratio of the stress peak of notched configuration to nominal uniform stress of unnotched specimen. Hence, the fatigue strength of the notched configuration is obtained by dividing the fatigue strength of the pristine specimen by the stress concentration factor.

Nevertheless, when a positive mean stress is applied, i.e. $S_m > 0$, both S_{max} and S_{min} increase accordingly to K_t , as shown in Figure 5.6. Consequently, stress amplitude S_a and mean stress S_m for the notched configuration need to be multiplied by a factor K_t . Also in this case, according to the Similarity Principle, the same fatigue response occurs when both notched and unnotched configurations reach the same stress peaks.

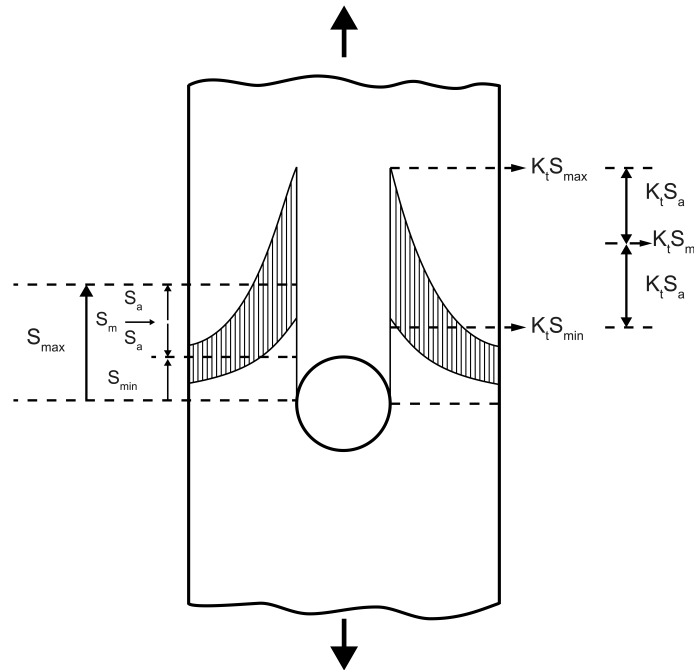


Figure 5.6 Schematic illustration of the Similarity Principle between notched and unnotched specimen, for $S_m > 0$. Adapted from [56].

Figure 5.7 provides an example of fatigue strength prediction employing the Similarity Principle, with the application of K_t to both S_a and S_m . This method basically consists of translating CLDs, initially derived from experimental tests of a pristine structural component, in order to predict fatigue strength of damaged configurations of the same component.

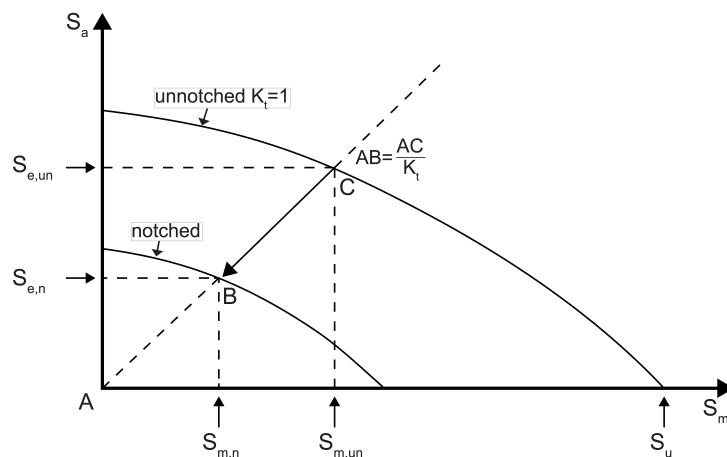


Figure 5.7 Example of fatigue strength prediction employing the Similarity Principle, with the application of K_t to both S_a and S_m . Adapted from [56].

In this thesis, the Similarity Principle is exploited to predict fatigue strength of damaged WSLs bonded configurations, extrapolating experimental test results from BOPACS test campaign. Nevertheless, during this experimental investigation, pristine WSLs bonded joint configuration has not been fatigue-tested up to failure, and no experimental fatigue strength is available. Therefore, a reverse approach is proposed, and a flowchart is provided in Figure 5.8.

A WSLs specimen with an initial artificial disbond of 16% has been subjected to a fatigue test with a maximum load level $P_{max} = 90$ kN and $R = 0.1$. The configuration failed at $N_f \approx 7 \cdot 10^5$, which represents the constant life in terms of number of cycles to failure employed as reference for CLDs predictions. The stress concentration factor K_t is extrapolated from the FE numerical investigations by analyzing shear stress redistribution that takes place in the bondline due to the disbond. Then, by combining the mathematical relationships provided in Section 5.2, it is possible to obtain the applied mean stress S_m and stress amplitude S_a required to draw a point in the CLDs plot. The maximum applied load P_{max} is normalized with respect to the initial bonded area of the WSLs specimen to calculate the maximum stress. The ultimate tensile stress S_u of the pristine WSLs bonded joint is also extrapolated from BOPACS experimental outcome of static testing. Then, by solving Eq. 5.1 and 5.2 for \bar{S}_a , and substituting the following definition of S_a and S_m , respectively:

$$S_a = \left(\frac{1 - R}{2} \right) S_{max} \quad (5.4)$$

$$S_m = \left(\frac{1 + R}{2} \right) S_{max} \quad (5.5)$$

\bar{S}_a can be calculated as follows:

$$\bar{S}_a = \frac{S_{max}(1 - R)/2}{1 - \left(\frac{S_{max}(1 + R)}{2S_u} \right)^m} \quad (5.6)$$

where $m = 1$ for Goodman linear approximation, and $m = 2$ for Gerber parabola. Indeed, any combination of S_a and S_m on CLDs can be used to calculate the corresponding reversed load point, i.e. $R = -1$. Then, CLDs for pristine joint and several damaged configurations with different initial disbonded area are built exploiting both Goodman and Gerber equations. Finally, fatigue strengths are predicted, assuming the same test setup that was used during BOPACS experimental campaign, i.e. $R = 0.1$.

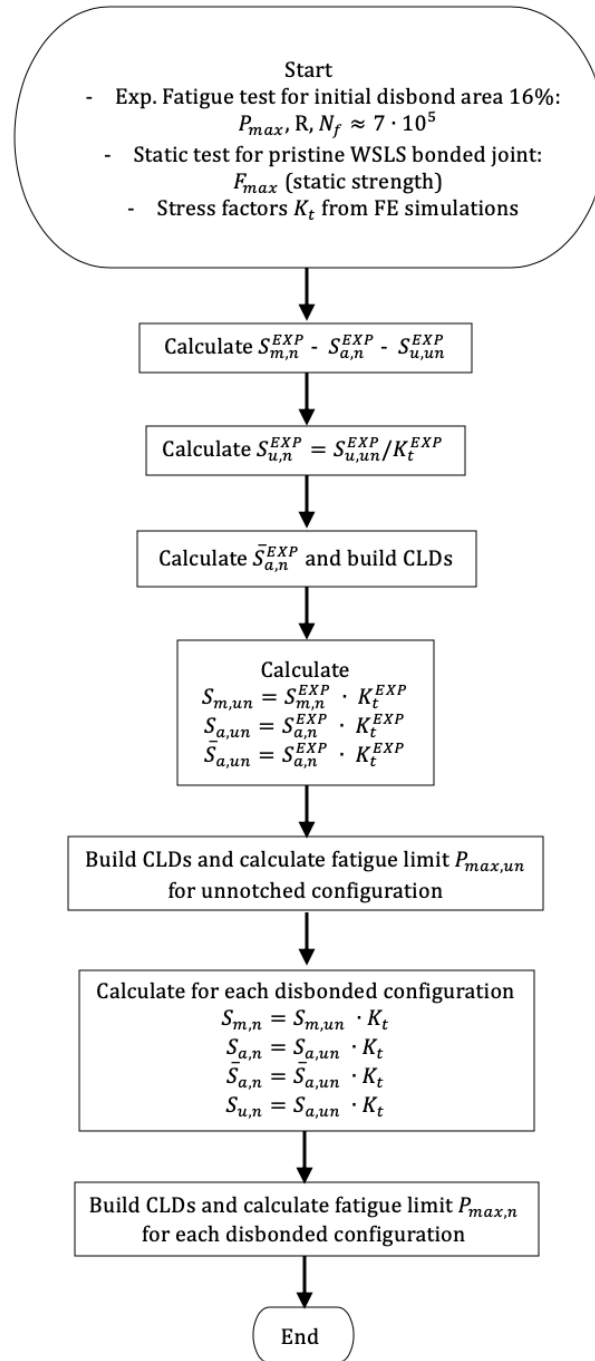


Figure 5.8 Flowchart of proposed procedure for fatigue strength predictions.

5.2.2 Fatigue Crack Growth Approach

The Fatigue Crack Growth (FCG) approach aims to correlate the fatigue crack growth rate da/dN due to cyclic loading to a fracture mechanics parameter to define a propagation curve. Evaluating fracture parameters is based on local stress and displacement fields in the structural component in which the crack is propagating.

For metals, the stress field at a crack tip is related to the stress intensity factor K . A good correlation between da/dN and the stress intensity factor range ΔK has been experimentally proven. This relationship leads to FCG curves characterized by a sigmoidal shape in a bi-logarithmic plot.

Many researchers have investigated cyclical debonding of adhesively bonded joints, and the correlation between fatigue debond growth rate da/dN and the strain energy release rate amplitude ΔG results in the same sigmoidal curve obtained for metals fatigue crack propagation [57, 58, 59]. However, both parameters G and K are only valid under the assumption of Linear Elastic Fracture Mechanics (LEFM) [15]. Figure 5.9 provides an example of a fatigue crack propagation curve for adhesively bonded joints in a bi-logarithmic diagram, which empathizes the typical sigmoidal shape.

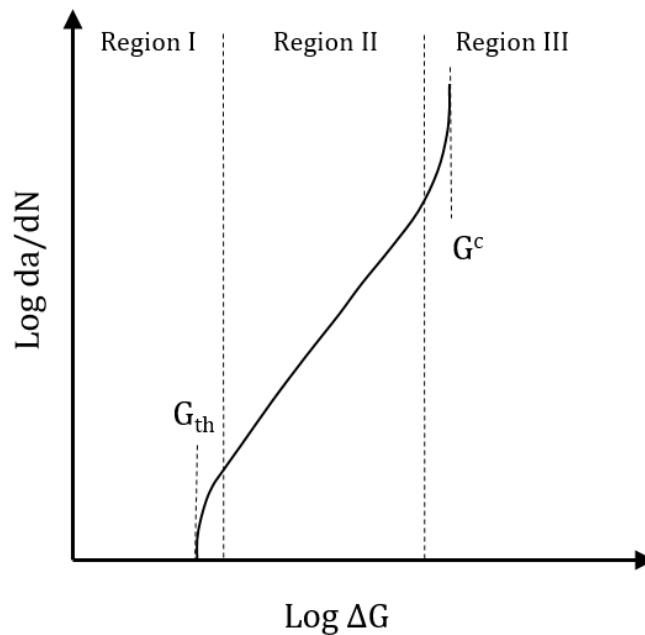


Figure 5.9 Example of a typical fatigue crack propagation curve for adhesively bonded joints.

Three different regions are usually identified in this curve. Region I is characterized by the fatigue threshold G_{th} , below which no measurable crack growth occurs. Region

II identifies a linear or steady phase of crack propagation, which can be mathematically fitted by Paris's law, expressed as follows:

$$\frac{da}{dN} = C_1 \Delta G^{C_2} \quad (5.7)$$

where C_1 and C_2 can be considered as material properties, extrapolated from experimental data fitting. Region III represents an unstable and fast crack growth phase reached when the maximum strain energy release rate G_{max} approaches the critical fracture energy G^c , which is the critical strain energy release rate in a static loading scenario [15]. Therefore, an estimation of the fatigue lifetime of the adhesively bonded joints can be assessed if the correlation between the crack extension a and ΔG is known.

In this thesis, by exploiting the outcomes of FE quasi-static numerical investigations, fracture mechanics energy-based criterion is used as a predictive tool for fatigue lifetime estimates of adhesively bonded joints. In particular, predictions are carried out for bonded joints characterized by ductile adhesive Scotch Weld 9323-B/A, for which Paris's law parameters have been experimentally assessed during Airbus internal project.

Proposed methodology for fatigue lifetime prediction: Energy Criterion

Compared to the Stress-life approach based on $S - N$ curves, the FCG approach allows an estimation of the crack extension Δa as a function of fatigue life expressed as number of cycles N . Therefore, the FCG curve can be potentially exploited to predict crack propagation in structural components. The starting point of the proposed methodology is the selection of fatigue crack growth law, which is obtained by fitting experimental fatigue test results. In the context of this thesis, Paris's law is used as a fatigue crack propagation curve, as defined in Eq. 5.7, and consequently, investigations are limited to Region II.

Strain energy release rate amplitude ΔG is derived from FE numerical simulations, by exploiting the following equation:

$$\Delta G = \left(\sqrt{G_{max}^{inst}} - \sqrt{G_{min}^{inst}} \right)^2 = (1 - R)^2 G_{max}^{inst} \quad (5.8)$$

where G_{max}^{inst} represents the instantaneous strain energy release rate related to the maximum applied fatigue load. The definition of ΔG presented in Eq. 5.8 is equivalent to use ΔK , and this definition is based on linear superposition principles for stresses that is the focus point of LEFM [60].

The value of G_{max}^{inst} is calculated by numerical integration of the traction-separation law adopted to define the constitutive response of the adhesive layer in Abaqus, as described in Section 4.3.1, and it can be expressed as follows:

$$G_{max}^{inst} = \int_0^{\delta_n^{max}} t_n d\delta_n + \int_0^{\delta_s^{max}} t_s d\delta_s + \int_0^{\delta_t^{max}} t_t d\delta_t \quad (5.9)$$

where the members of the right-side of the equation represent the contribution in terms of maximum instantaneous strain energy release rate of normal peel stress, longitudinal and transverse shear stresses, respectively, for a fixed maximum load level.

Paris's law parameters C_1 and C_2 depends on material properties, and loading mode expressed through MMR . Experimental tests conducted on Scotch Weld 9323-B/A adhesive proved that a B-K fitting curve can be used to described the influence of MMR on C_1 and C_2 , which are given by:

$$C_i = C_{i_I} + (C_{i_{II}} - C_{i_I})MMR^{\eta_{ci}} \quad i = 1, 2 \quad (5.10)$$

where C_{i_I} , $C_{i_{II}}$ and η_{ci} are fitting constants.

Finally, the crack growth rate da/dN can be locally calculated for each finite element of the adhesive layer employing the Paris's law, as expressed in Eq. 5.7. In order to assess whether or not a finite element fails due to the selected maximum load level applied during FE quasi-static simulations, the calculated da/dN has to be compared to a threshold value $(da/dN)_{th}$.

For a pristine WLS joint, $(da/dN)_{th}$ is fixed at $1 \cdot 10^{-6}$ mm per cycle, i.e. 1 mm for 1 million cycles, representing an acceptable crack growth for a lifetime of almost 10 airframe lifetime [41]. The main outcome of this analysis is the definition of the no-growth level, which is the maximum applicable load level in a cyclic fatigue loading scenario that does not induce a crack in the bondline. For adhesively bonded joints, this limit generally varies between 15% and 40% of the static strength of the joint [15, 54, 55].

For WLS configurations with disbond in the bondline, $(da/dN)_{th}$ is defined by exploiting experimental fatigue test results obtained within BOPACS campaign. During this project, two WLS disbanded configurations have been tested for fatigue, characterized by an initial disbond area of 12% and 16%, respectively. Figure 5.10 provides crack width increments measured by non-destructive ultrasonic inspections every k-cycles. Each increment a is normalized according to the maximum crack width a_{max} measured during the last inspection before the final rupture.

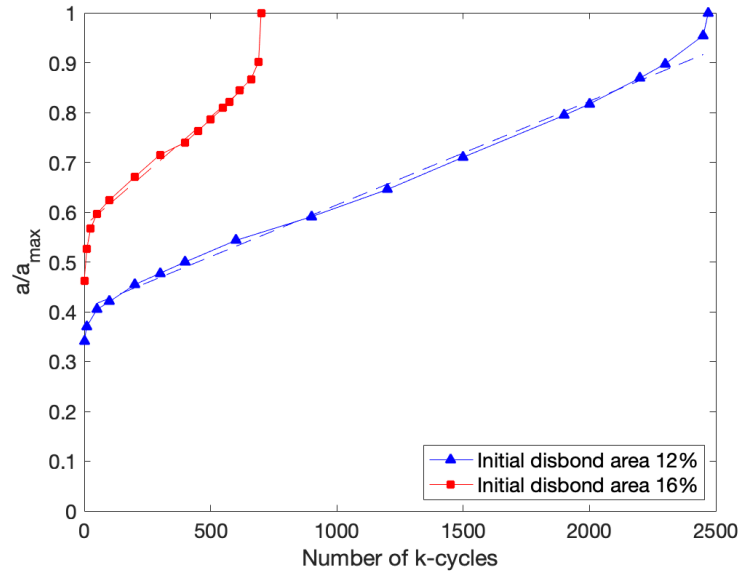
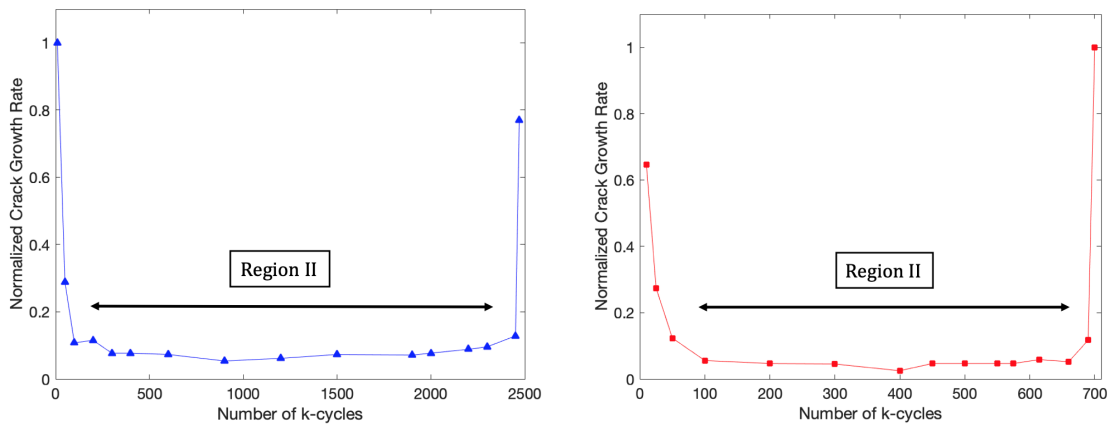


Figure 5.10 Normalized crack width increment measured by ultrasonic inspection as a function of number of k-cycles, for two WSLs bonded configurations characterized by an initial disbond area of 12% and 16%, respectively. Extrapolated from BOPACS test campaign.

For both configurations, a steady-state of stabilized constant crack growth rate was found. Experimental outcomes are shown in Figure 5.11, in which the previously defined Region II is highlighted. The crack growth rate is normalized according to the maximum registered value.



(a) Initial disbonded area of 12%.

(b) Initial disbonded area of 16%.

Figure 5.11 Normalized crack growth rate as a function of number of k-cycles. Extrapolated from BOPACS test campaign.

In order to apply the proposed methodology, experimental values of constant crack growth rate are selected as $(da/dN)_{th}$ for WSL configurations characterized by the same initial disbond area. This assumption allows an estimate of the maximum applicable load to ensure starting of fatigue crack growth for the two configurations under examination.

The next step is the lifetime predictions, expressed as the number of cycles needed to grow the disbond up to a critical condition. Indeed, a relatively simplified procedure can simulate the crack growth when the structural component is subjected to a constant stress amplitude load [56, 61]. A flowchart of the proposed numerical procedure is summarized in Figure 5.12.

The procedure starts by assuming an initial crack extension a_0 , which, in this context, refers to the width of the disbond along the overlap edges. FE quasi-static analysis is performed, applying the maximum load determined previously. Then, the maximum strain energy release rate is calculated according to Eq. 5.9. If G_{max}^{inst} exceeds G^c , it means that the Region II has been crossed and no more simulations are required. Otherwise, for the current state, the crack growth rate da/dN is calculated for each finite element, compared to the threshold $(da/dN)_{th}$ to determine if the element failed. Then, the incremental growth of the disbond width Δa is given by adding all the failed elements. Finally, the number of cycles ΔN for the current step is calculated as follows:

$$\Delta N = \frac{\Delta a}{(da/dN)_{min}} \quad (5.11)$$

where $(da/dN)_{min}$ represents the last failed element's crack growth rate in the current step, in case of more than one element failure. The new crack size a_1 is then calculated as the sum of a_0 and Δa , and another FE quasi-static simulation is performed with a new disbond size with a width equals to a_1 . The disbond size is grown until a finite element reaches the critical condition in terms of maximum strain energy release rate. Once the rupture criterion is met, the predicted lifetime of the structural component corresponds to the total number of cycles needed to grow the disbond up to the critical size.

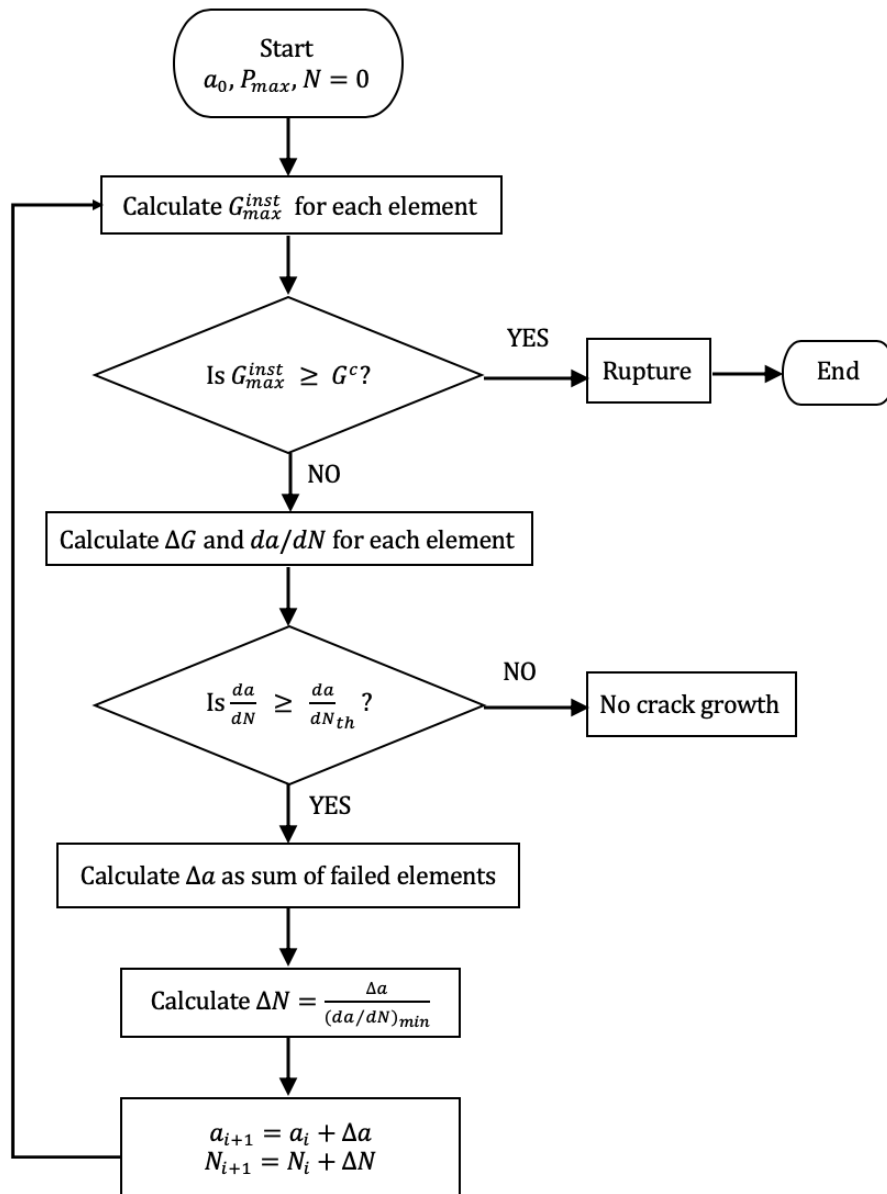


Figure 5.12 Flowchart of proposed procedure for fatigue lifetime predictions.

Chapter 6

Results

In this Chapter, numerical results are presented and classified in two major Sections. Section 6.1 describes the comparative numerical assessment of joint static strength reduction due to the presence of disbonds, whereas in Section 6.2, numerical fatigue predictions are proposed.

6.1 Comparative Evaluation of Strength Reduction

This Section delves into the numerical results of strength reduction obtained from FE quasi-static analysis of different WSLs configurations with embedded disbonds in the joining line. In the following, the numerical investigation outcomes are initially presented for each material data set, as described in Section 5.1.1, to highlight the influence of disbond size on the joint strength. Afterward, a detailed discussion about the influence of material properties is suggested, as explained in Section 5.1.2. Whenever possible, a comparison between numerical investigations and experimental results is provided to validate the proposed FE modeling design.

A uniform notation is applied in the following Sections to define disbond sizes to ease the interpretation of the results. Each damage is identified by two dimensions: the width x and the length y . The reference system is illustrated in Figure 5.1. For each material, numerical predictions of maximum failure loads are normalized using as reference the maximum ultimate load for the corresponding pristine joint. The initial disbonded area is evaluated as the percentage of the pristine joining area without any artificial disbond.

6.1.1 Thermoset WSLS bonded joint - Loctite EA 9395

The FE models of WSLS bonded joints consisting of thermoset laminated composite adherends and Loctite EA 9395 adhesive simulate the specimens employed during BOPACS test campaign [41].

Figure 6.1 provides numerical estimates of load-displacement responses of WSLS bonded joints affected by different disbond widths and fixed length equal to the total overlap length of 60 mm. The curves are compared to the numerical prediction for a pristine WSLS configuration, in which no damage is present in the bondline. These numerical investigations are especially carried out to compare numerical outcomes with available test data extrapolated from BOPACS campaign.

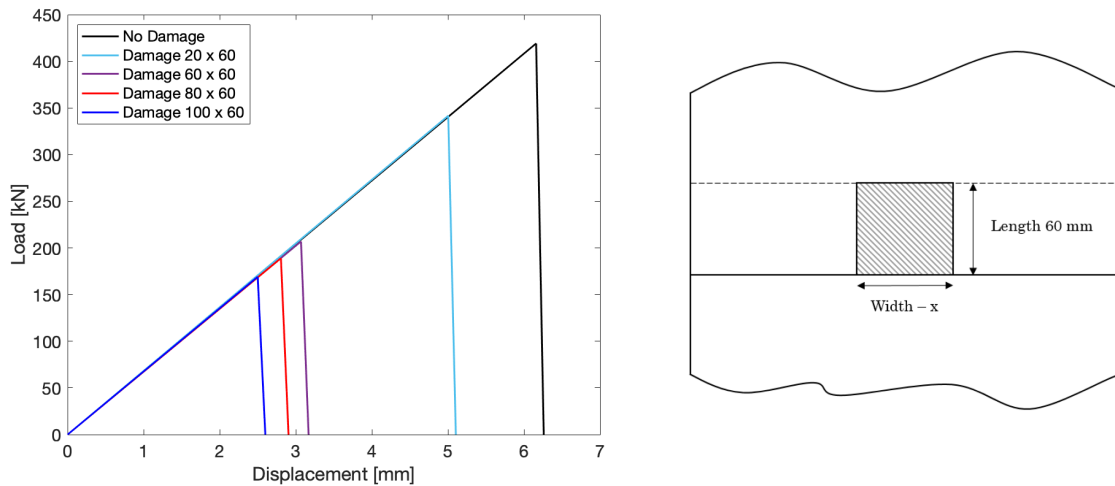


Figure 6.1 Numerical estimates of load-displacement responses of WSLS bonded joints (Loctite EA 9395 adhesive) accounting for different widths of artificial disbonds characterized by a full-damaged overlap length, compared to the numerical prediction for a pristine configuration.

Figure 6.2 compares numerical predictions and experimental results of maximum failure loads depending on different initial disbond areas. Predicted loads are normalized according to the experimental maximum static strength found during BOPACS test campaign. Good agreement is obtained between FE numerical outputs and experimental data. The exponential trend fits the overall joint strength reduction quite well when the disbond approaches both edges of the overlap.

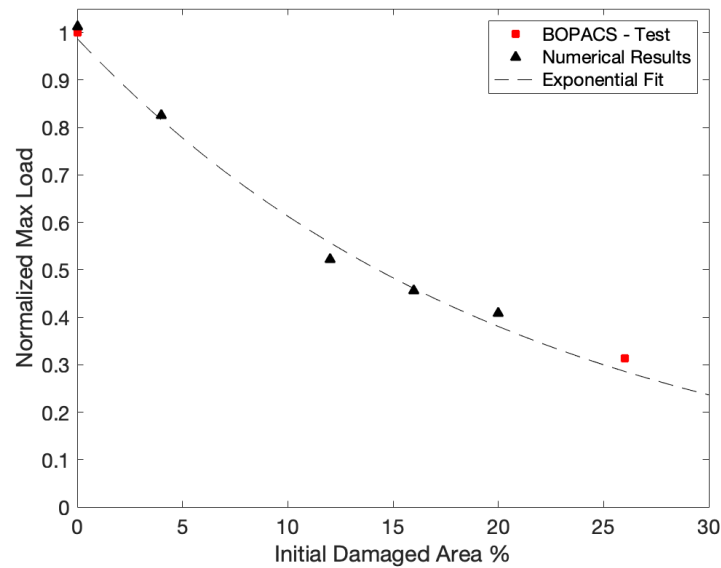
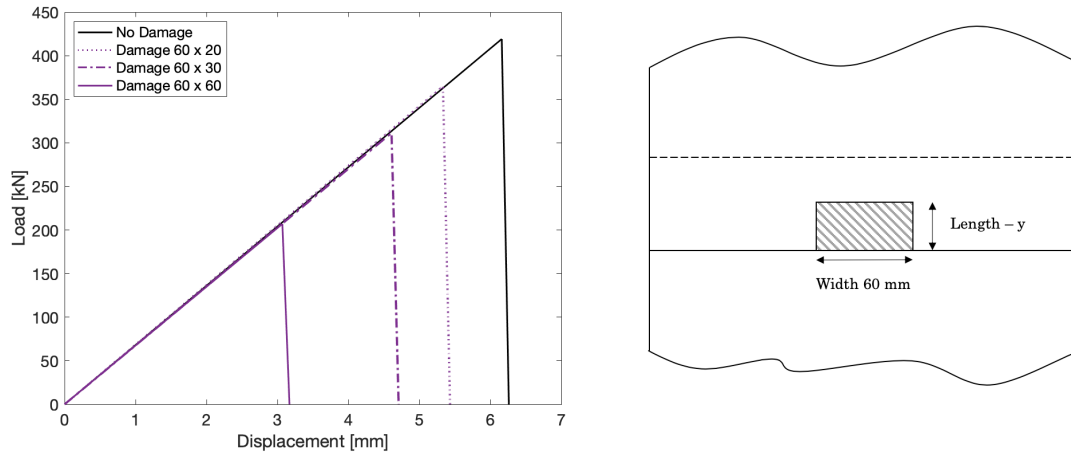
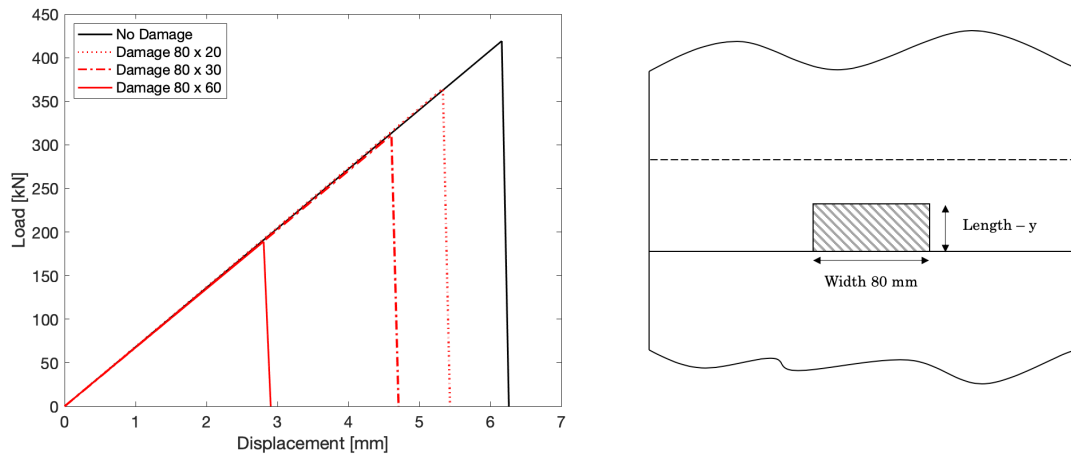


Figure 6.2 Normalized maximum failure loads comparison between numerical predictions for WLS bonded joints (Loctite EA 9395 adhesive) and experimental results from BOPACS test campaign, according to different initial disbond areas. Exponential trendline is displayed.

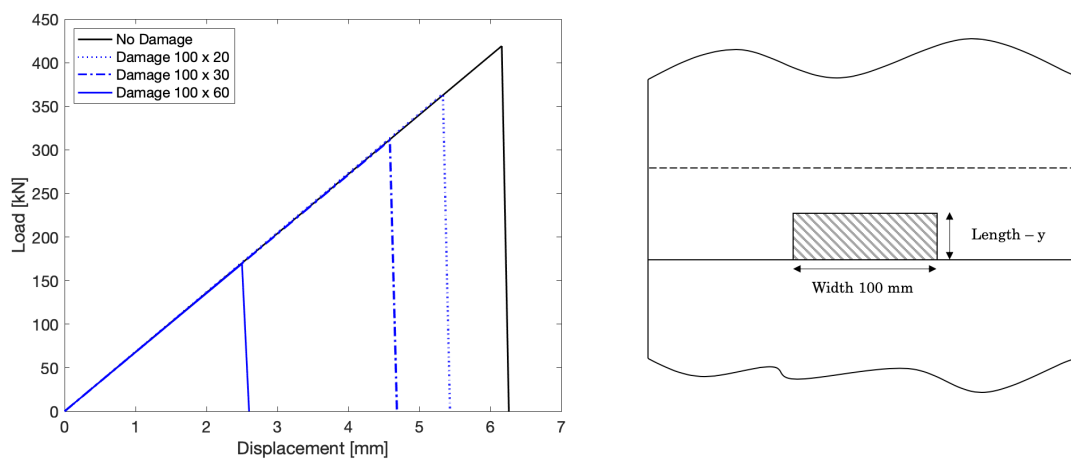
In order to deeper understand the dependence of the load carrying-capability on disbond dimensions, subsequent analyses aim to investigate the influence of both disbond length and width. Figures 6.3a, 6.3b, and 6.3c provide predicted load-displacement responses for artificial damaged WLS bonded joints with variable damage length in the loading direction, and damage width of 60 mm, 80 mm, and 100 mm, respectively. Regarding the damage length, besides the full-length removal previously considered, two other configurations are investigated, i.e. disbond length equals to 30% and 50% of the total overlap length.



(a) Damages with fixed width of 60 mm, and variable length.



(b) Damages with fixed width of 80 mm, and variable length.



(c) Damages with fixed width of 100 mm, and variable length.

Figure 6.3 Predicted load-displacement responses of WSLs bonded joints (Loctite EA 9395 adhesive) considering several disbonds characterized by different sizes of length and width.

An almost linear dependence between strength reduction and increase of damage length characterizes the joint's behavior, as illustrated in Figure 6.4. Moreover, regardless of the increasing disbond widths, bonded joints show almost the same strength for a specific damage length, as illustrated in Figure 6.5. Hence, although the initial bonded area decreases due to an increase of initial disbond, the joint strength is almost constant. This behavior suggests that, for this joint configuration, the reduction of load carrying-capability may be the consequence of partial removal of leading edges in the bondline, which is discussed in Section 6.1.4.

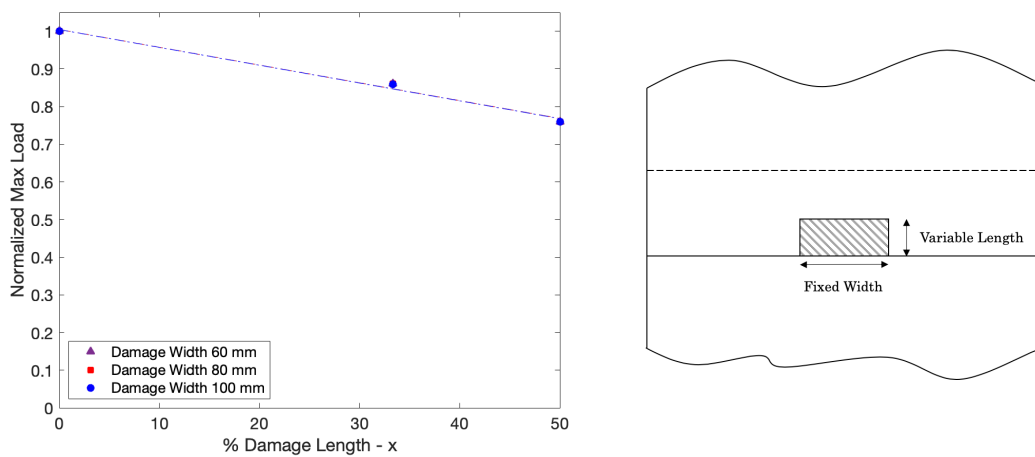


Figure 6.4 Linear dependence of strength reduction on the increase in disbond length in the bondline of WSLs bonded joints (Loctite EA 9395 adhesive). Results extrapolated from FE numerical simulations.

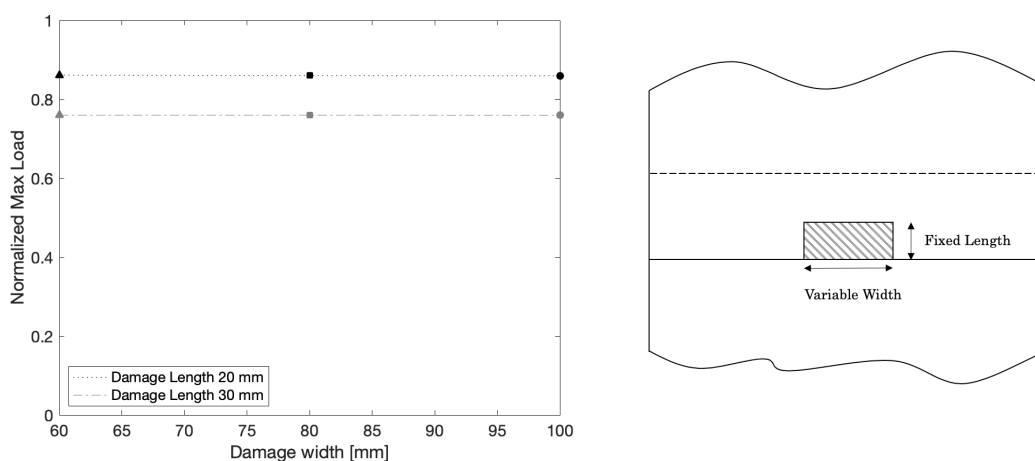


Figure 6.5 Influence of increasing disbond width in the bondline on strength reduction of WSLs bonded joints (Loctite EA 9395 adhesive). Results extrapolated from FE numerical simulations.

6.1.2 Thermoset WSLs bonded joint - Scotch Weld 9323-B/A

In the following, numerical strength analysis of WSLs bonded joint consisting of thermoset laminated composite adherends and Scotch Weld 9323-B/A adhesive is introduced. For this joint configuration, no experimental data are available for validation purposes of numerical predictions.

Figure 6.6 provides numerical estimates of load-displacement responses for WSLs bonded joints for different width sizes of disbands, which are characterized by a length equal to the total overlap length of 60 mm. The curves are compared to the numerical prediction for a pristine WSLs configuration, in which no damage is present in the bondline.

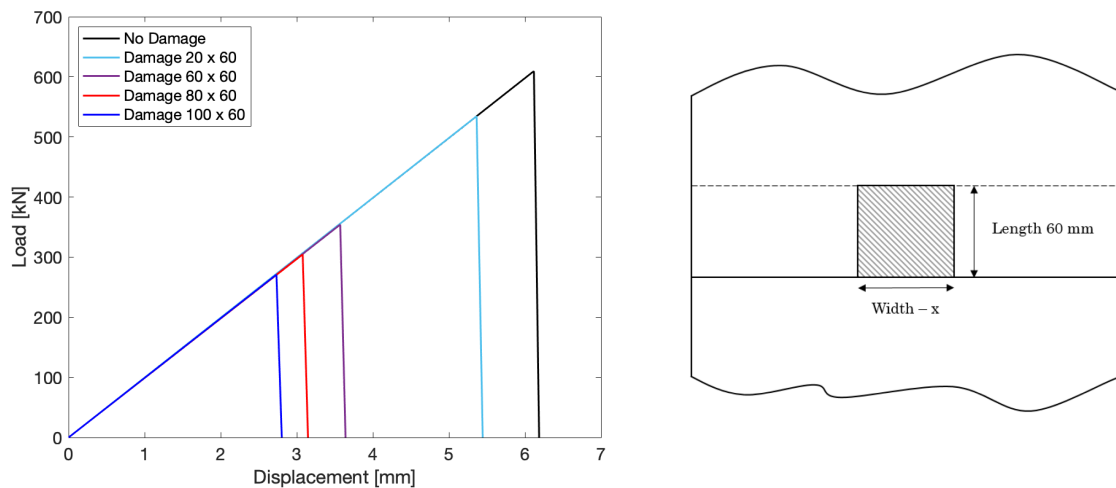


Figure 6.6 Numerical estimates of load-displacement responses of WSLs bonded joints (Scotch Weld 9323-B/A adhesive) accounting for different widths of artificial disbands characterized by a full-damaged overlap length, compared to the numerical prediction for a pristine configuration.

Also in this case, the exponential trendline is in good agreement with the joint strength reduction trend when disbands extend from one overlap edge to the other, as shown in Figure 6.7.

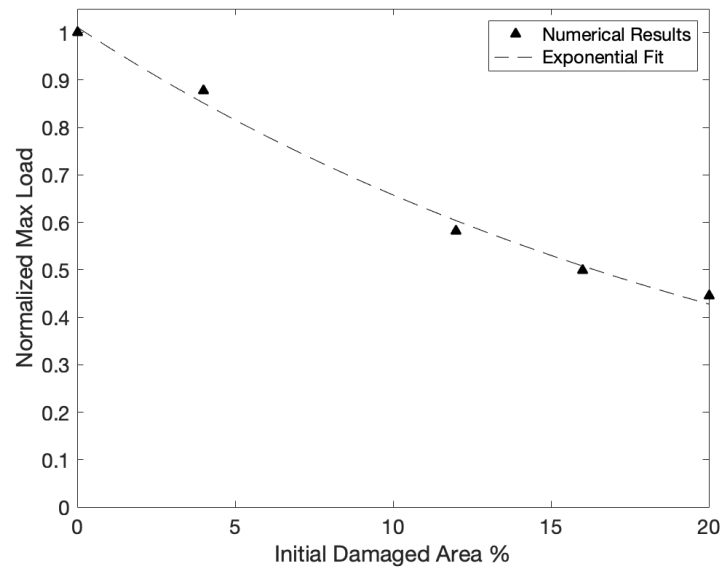
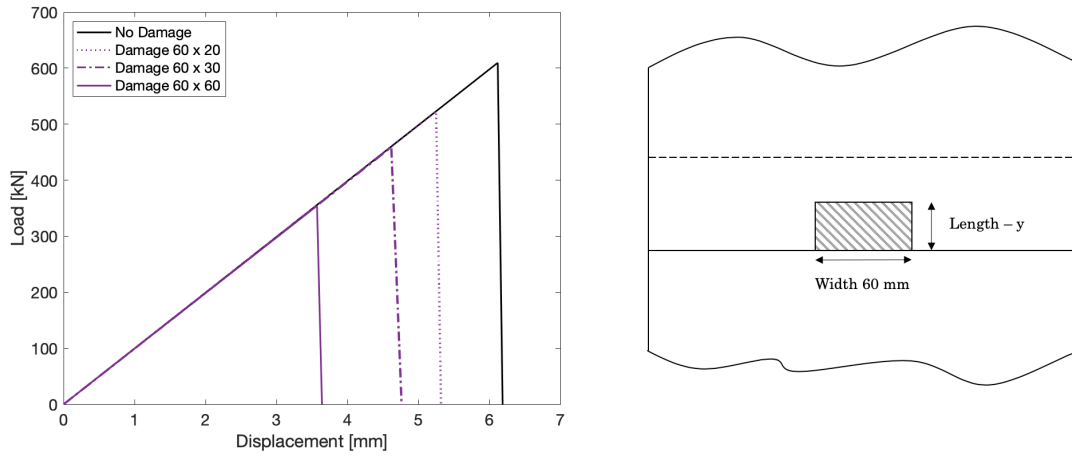
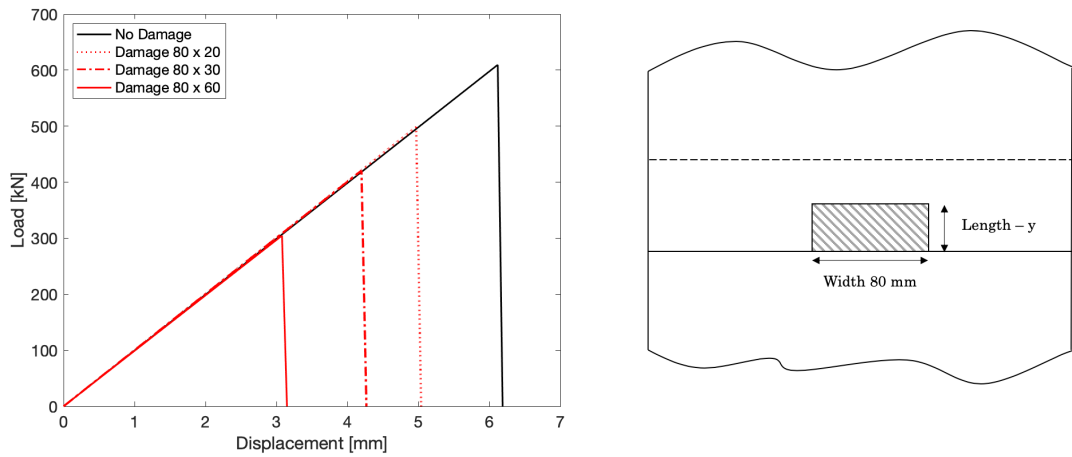


Figure 6.7 Normalized maximum failure loads numerically predicted for WSLs bonded joints (Scotch Weld 9323-B/A), according to different initial disbond areas. Exponential trendline is displayed.

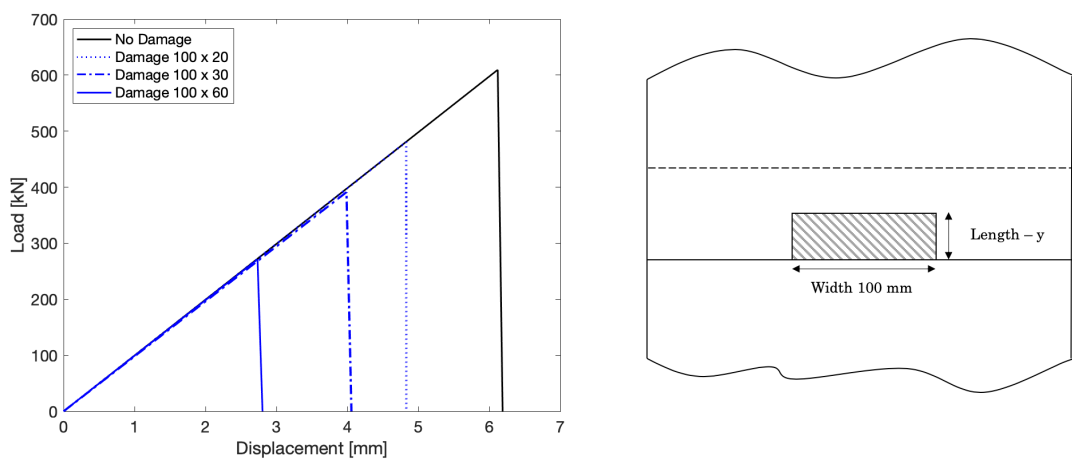
Numerical investigations are carried out to delve into the influence of disbond dimensions. They lead to different results when Scotch Weld 9323-B/A properties are used to simulate the adhesive layer of WSLs bonded joint. Figures 6.8a, 6.8b, and 6.8c provide predicted load-displacement responses for artificial damaged WSLs bonded joints with variable damage length in the loading direction, and damage width of 60 mm, 80 mm, and 100 mm, respectively. Like before, regarding the damage length, three configurations are investigated, namely disbond length equals to 30%, 50%, and 100% of the total overlap length.



(a) Damages with fixed width of 60 mm, and variable length.



(b) Damages with fixed width of 80 mm, and variable length.



(c) Damages with fixed width of 100 mm, and variable length.

Figure 6.8 Predicted load-displacement responses of WSLs bonded joints (Scotch Weld 9323-B/A adhesive) considering several disbonds characterized by different sizes of length and width.

Figures 6.9 and 6.10 aim to assess whether the influence of either disbond length and width may lead to different behaviors. An almost linear decrease of joint strength is obtained depending on both damage length and width. It is clear that the more the initial bonded area decreases due to an increase in artificial damage size, the more the joint strength reduces. The continuous reduction of load carrying-capability may suggest that the initial amount of bonded area assumes a key role for this joint configuration.

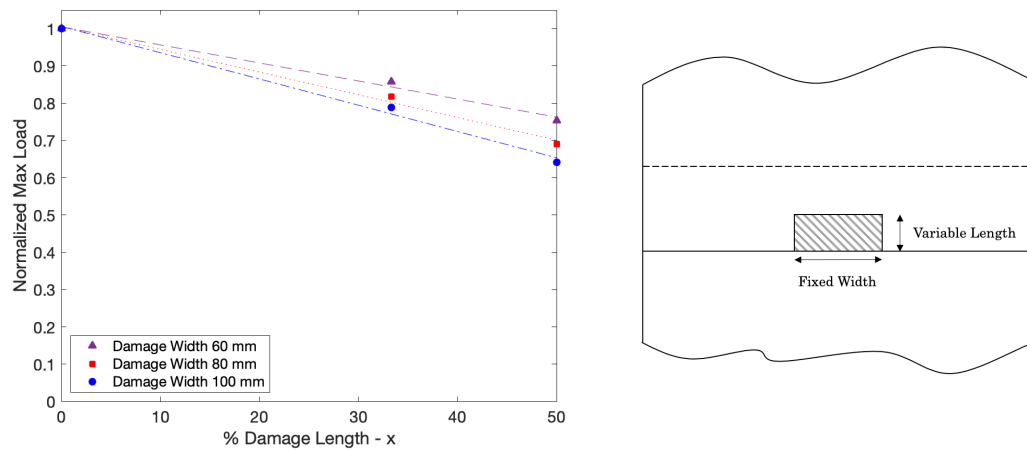


Figure 6.9 Linear dependence of strength reduction on increase in disbond length in the bondline of WSLS bonded joints (Scotch Weld 9323-B/A adhesive). Results extrapolated from FE numerical simulations.

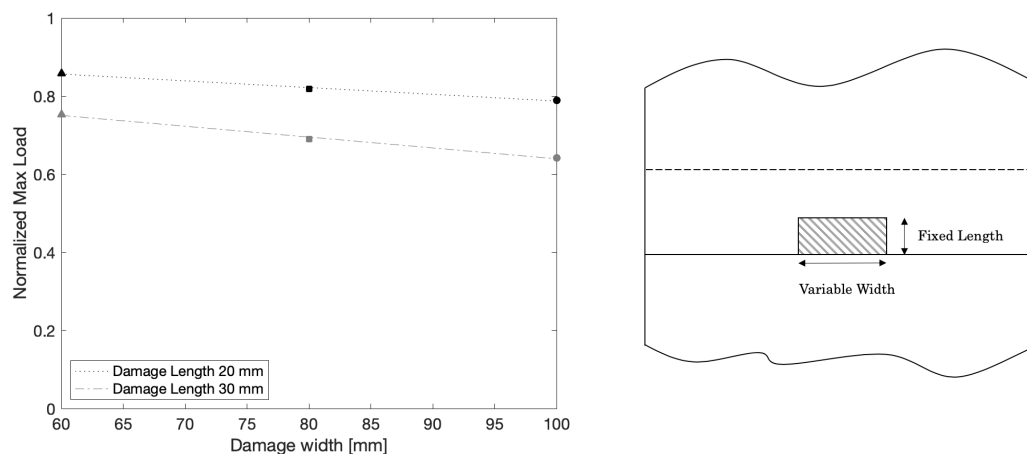


Figure 6.10 Linear dependence of strength reduction on increase in disbond width in the bondline of WSLS bonded joint (Scotch Weld 9323-B/A adhesive). Results extrapolated from FE numerical simulations.

Whenever damage is present in the bondline, WSLs bonded joints with Scotch Weld 9323-B/A adhesive behave differently from the configurations analyzed in Section 6.1.1, in which Loctite EA 9395 material data were used to model the adhesive layer. It is deemed that the adhesive's properties highly influence the joint strength. Indeed, the stress redistribution, which takes place in the bondline around the damaged area, strongly depends on the adhesive's mechanical response. For instance, peaks stress increases are not well supported by a brittle adhesive, whereas ductile adhesives accommodate a more uniform stress state within the bondline. More in-depth insight and understanding into these peculiar behaviors are provided in Section 6.1.4.

6.1.3 Thermoplastic WSLs welded joint - PEKK matrix

The joining line of thermoplastic WSLs welded joints is assumed to consist of a thin layer of PEKK polymer matrix, which results from the welding process. This joining technique is still under research within Airbus, and no experimental data are available as a benchmark for the proposed numerical investigations.

By following the same outline proposed in Sections 6.1.1 and 6.1.2, numerical estimates of load-displacement responses for a WSLs welded joints are illustrated in Figure 6.11, accounting for different widths of disbands characterized by a full-damaged overlap length of 60 mm. The overall trend of strength reduction follows a more straight pattern, i.e. the maximum failure load linearly decreases as the initial disbonded area increases, as shown in Figure 6.12.

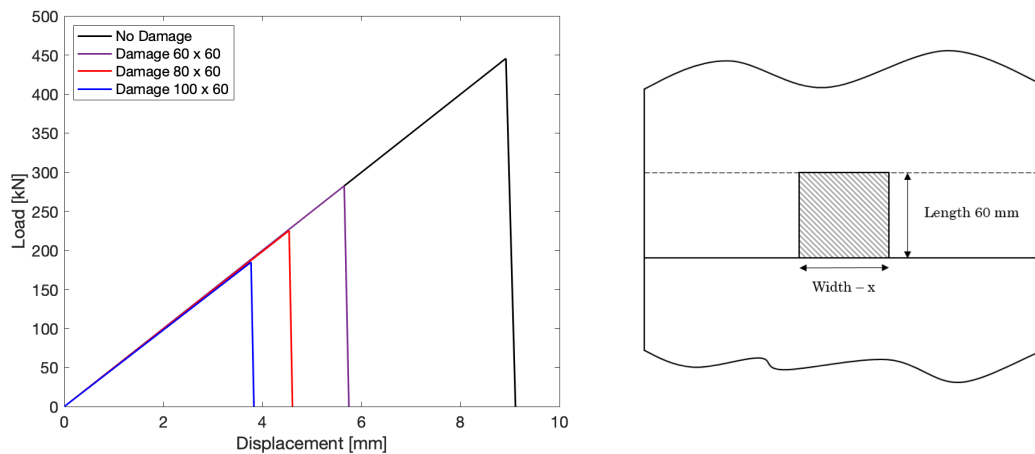


Figure 6.11 Numerical estimates of load-displacement responses of WSLs welded joints (PEKK polymer matrix) accounting for different widths of disbands characterized by a full-damaged overlap length, compared to the numerical prediction for a pristine configuration.

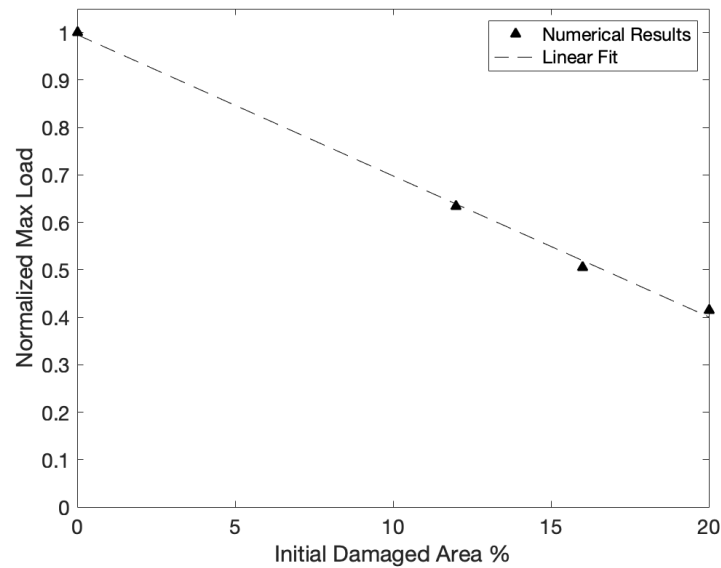
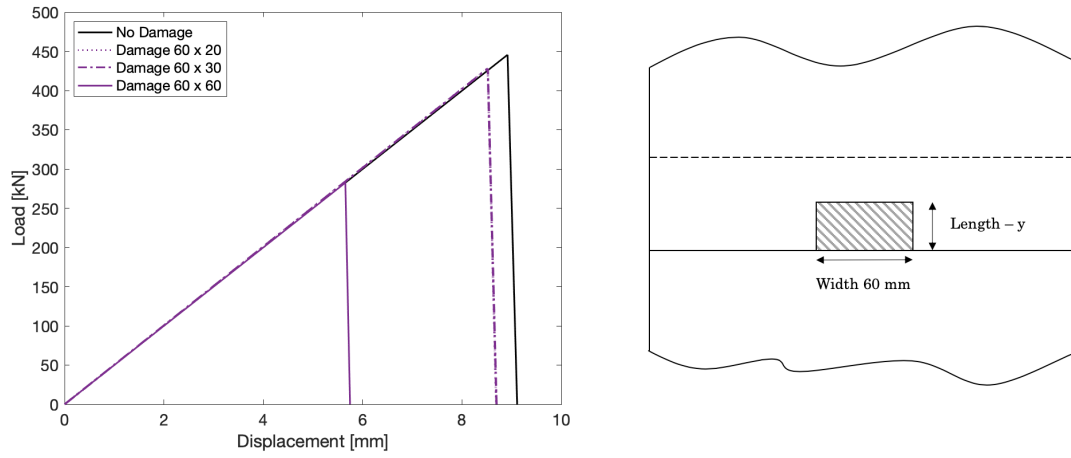
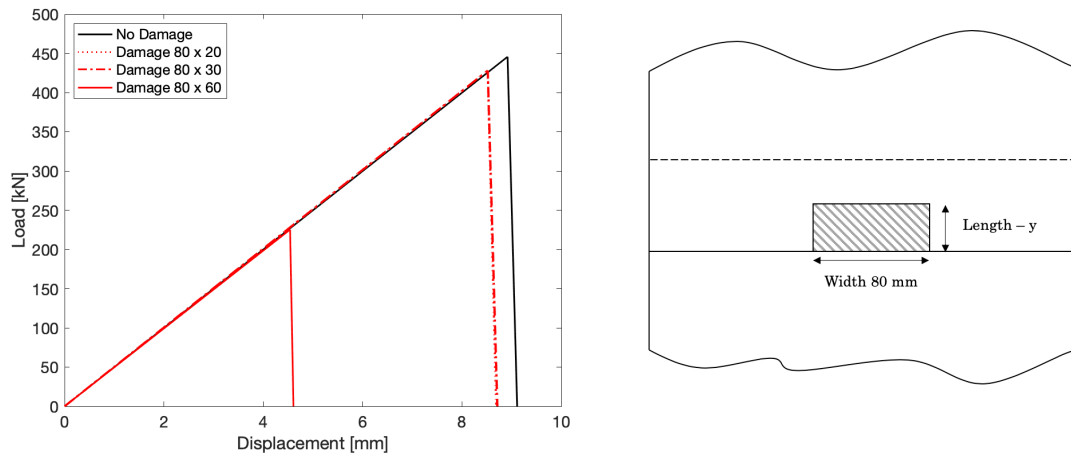


Figure 6.12 Normalized maximum failure loads numerically predicted for WSLS welded joints (PEKK polymer matrix), according to different initial disbond areas. Linear trendline is displayed.

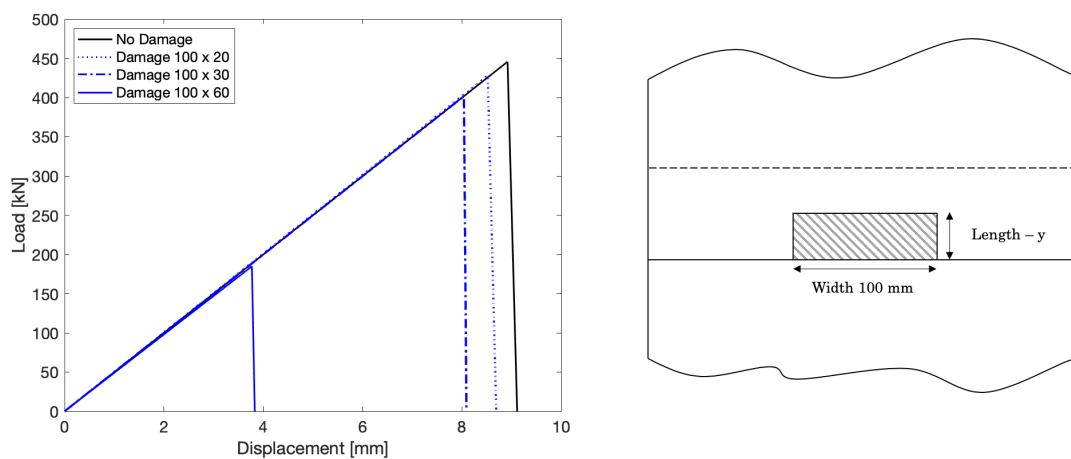
To assess the influence of disbond sizes, Figures 6.13a, 6.13b, and 6.13c provide predicted load-displacement responses for artificial damaged WSLS welded joints with variable damage length, namely 30%, 50%, and 100% of the total overlap length, and width, namely 60 mm, 80 mm, and 100 mm. It is interesting to note that regardless of the damage's width if the disbond affects only a percentage of the overlap length, no substantial reduction in the joint strength is experienced. In particular, load-displacement responses coincide for damage length of 30% and 50% in Figures 6.13a and 6.13b, whereas a slight decrease is found for wider damage, as shown in Figure 6.13c.



(a) Damages with fixed width of 60 mm, and variable length.



(b) Damages with fixed width of 80 mm, and variable length.



(c) Damages with fixed width of 100 mm, and variable length.

Figure 6.13 Predicted load-displacement responses of WSLs welded joints (PEKK polymer matrix) considering several disbonds characterized by different sizes of length and width.

6.1.4 Discussion

For the numerical comparison, two different adhesive datasets were used to model the bondline of WSLS bonded joints. In contrast, a thermoplastic polymer matrix simulated the weldline in the welded reference model.

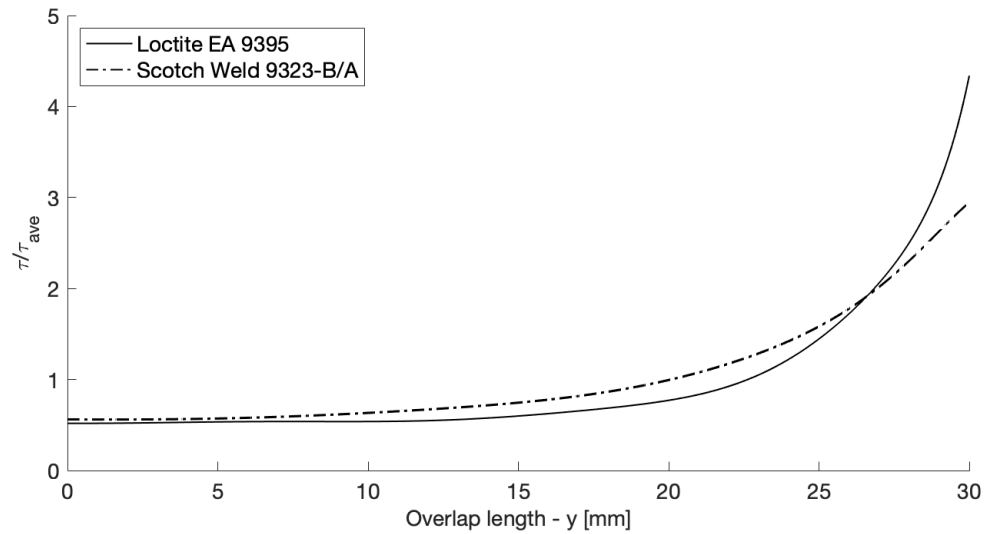
Globally, numerical results indicate a reduction of joint strength whenever a disbond occurs in the joining line. Nonetheless, each material exhibits a different reduction trend depending on the disbond size. As explained in Section 5.1, load transfer between the adherends of the joint is interrupted when a disbond is present in the joining line. Consequently, stress peaks around the damaged area increase because the loads concentrate toward the closest healthy portion of the joining area, which surrounds the damage. However, stress increases are handled in different ways, depending on the joining line properties.

In the following, the different behaviors of WSLS bonded joints are discussed. Moreover, some considerations about welded joints are made to propose a step forward in this new field of research.

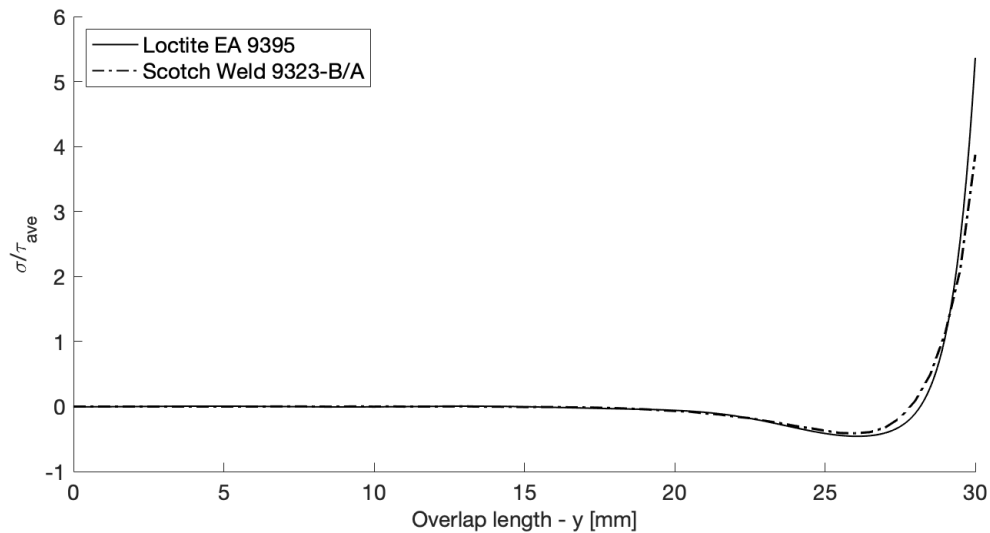
Thermoset WSLS bonded joints: influence of adhesive properties

Concerning material properties, Loctite EA 9395 and Scotch Weld 9323-B/A adhesives exhibit completely a different response to deformation. Therefore, they can be classified into two different material categories, namely brittle and ductile.

According to Wang et al. [30], at the bondline ends of a SLJ, a brittle adhesive experiences higher stress peaks than a ductile adhesive. Figure 6.14 provides typical stress distributions that develop in the undamaged bondline of a WSLS joint, considering both Loctite EA 9395 and Scotch Weld 9323-B/A adhesives, for a specific applied load. Stresses are normalized according to the bondline average stress τ_{ave} , defined as the ratio between the applied load and the bonded area. Loctite EA 9395 shows much severe stress peaks at the overlap ends, as expected from a brittle adhesive. On the contrary, Scotch Weld 9323-B/A accommodates a slightly more effective stress distribution within the bondline, which proves a higher grade of ductility.



(a) Comparison of shear stress distribution in the joint bondline.



(b) Comparison of peel stress distribution in the joint bondline.

Figure 6.14 Comparison between numerical shear and peel stress distribution in the adhesive layer of Loctite EA 9395 (solid line) and Scotch Weld 9323-B/A (dashed line). Only one half of the overlap length is illustrated due to symmetry reasons, and results are normalized using as reference the average shear stress.

The presence of a disbond in the bondline enhances these different behaviors, as shown in Figure 6.15. The stress gradients caused by the presence of the disbond for Loctite EA 9395 and Scotch Weld 9323-B/A adhesives are equal to 2.7 and 1.6, respectively. According to Ribeiro et al. [27], a higher stress gradient is a typical response of a brittle adhesive, whereas ductile adhesive exhibits less sharp stress

increase. These different ways of redistributing stresses around the damaged area in the bondline inevitably lead to a diverse joint strength reduction as the damage size increases.

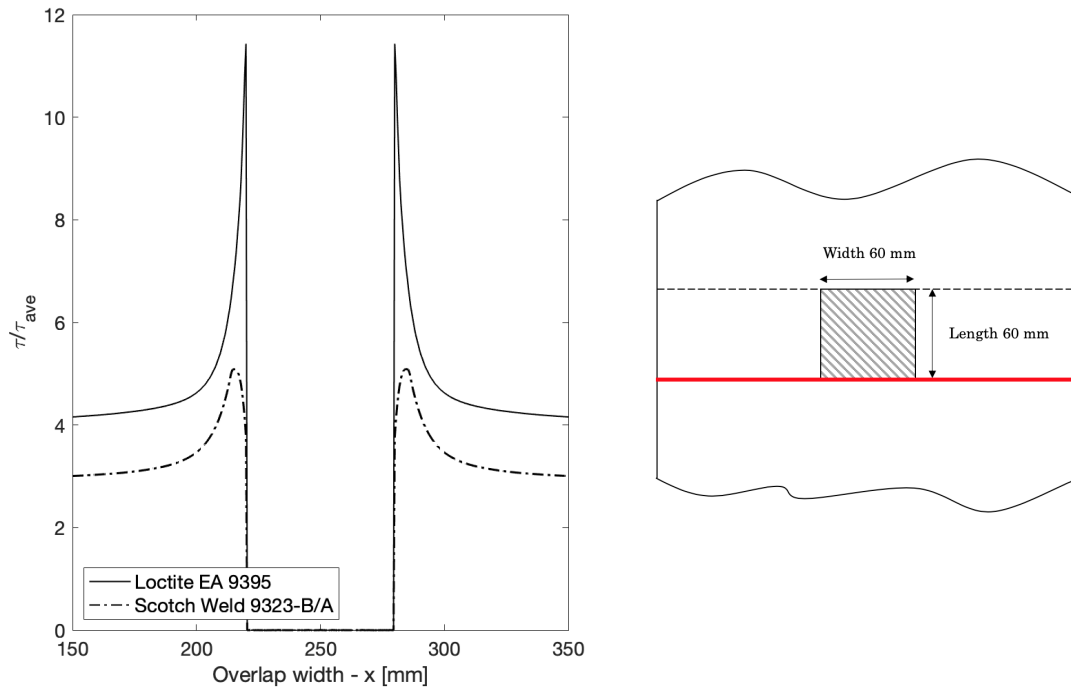
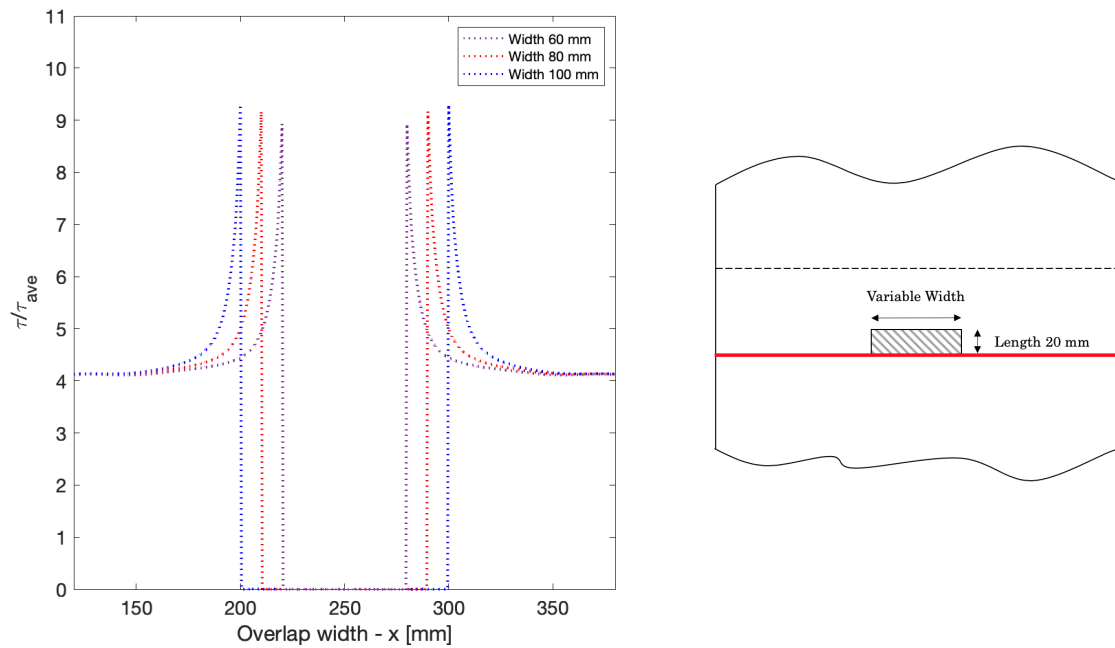
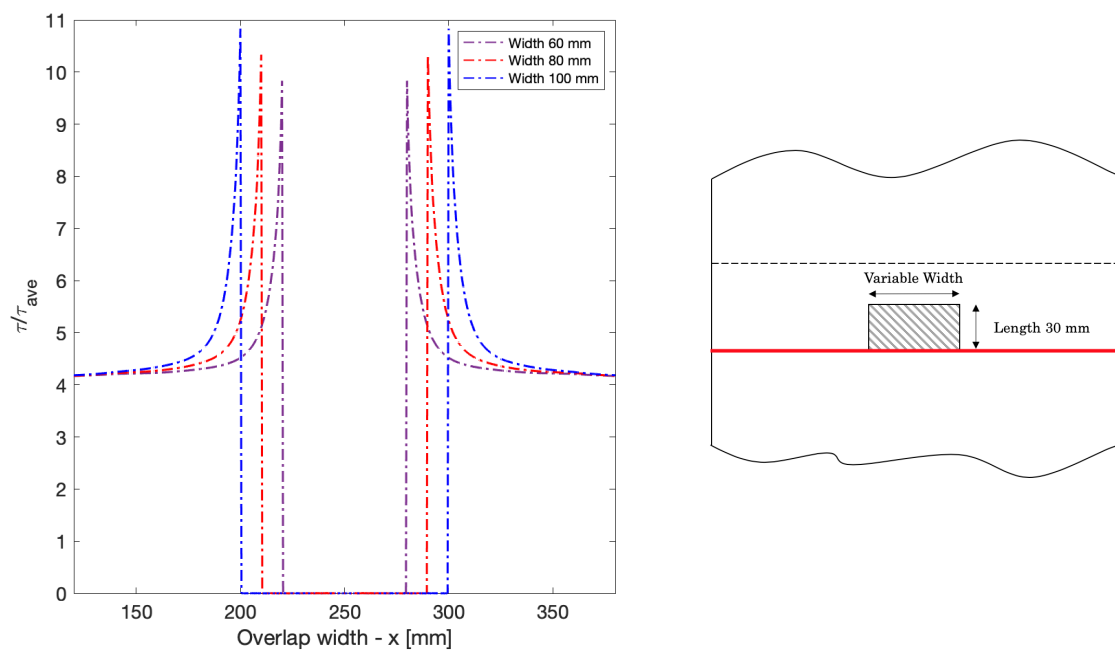


Figure 6.15 Normalized shear stress distribution in the adhesive layer of Loctite EA 9395 (solid line) and Scotch Weld 9323-B/A (dashed line) when a damage is present in the bondline, extrapolated from FE numerical simulations. The red line indicates the stress evaluation line.

In particular, since in a brittle adhesive the stress concentrates toward the overlap edges, the joint strength reduction is mainly driven by the ends of the bondline [30]. Therefore, when a disbond does not approach both overlap leading edges, the joint's load-carrying capability is not markedly reduced. This effect is illustrated in Figure 6.4, i.e. the strength linearly decreases while the damage approaches towards the opposite overlap edge. In addition, for Loctite EA 9395, numerical investigations highlighted an almost constant value of maximum failure load when only a percentage of the overlap length is affected by the disbond, regardless of the damage width (see Figure 6.5). This outcome results from the stress redistributions that occur in the adhesive layer when a disbond is present, which are shown in Figure 6.16.



(a) Shear stress redistribution in damaged bondline, considering disbonds with fixed length of 20 mm.



(b) Shear stress redistribution in damaged bondline, considering disbonds with fixed length of 30 mm.

Figure 6.16 Comparison between different shear stress redistributions in the adhesive layer of brittle Loctite EA 9395 adhesive caused by several damage sizes, for a specific applied load, extrapolated from FE numerical simulations. Red lines indicate the stress evaluation lines.

The stress peaks do not exhibit a very high increase as the damage gets wider, for a fixed damage length. The difference between the maximum and minimum stress values in Figures 6.16a and 6.16b is equal to 1 MPa at most. Since the joint strength reduction for a brittle adhesive is driven by stress concentration at overlap ends, quite similar stress distributions lead to a similar reduction of joint load-carrying capability.

On the contrary, according to Schonhorn et al. [31], ductile adhesive shows high sensitivity to edge effects. Whenever a disbond occurs in the bondline, additional free edges are introduced in the adhesive layer, leading to joint strength reduction. Therefore, a continuous reduction of the joint load-carrying capability is expected when a ductile adhesive is used in a bonded joint. This effect is illustrated in Figures 6.9 and 6.10, i.e. the more the residual bonded area decreases, the more the ultimate joint strength reduces.

Finally, a global comparison between the two adhesives is provided in Figure 6.17, which highlights the different influence of disbond size in the two bondlines in terms of load-carrying capability reduction.

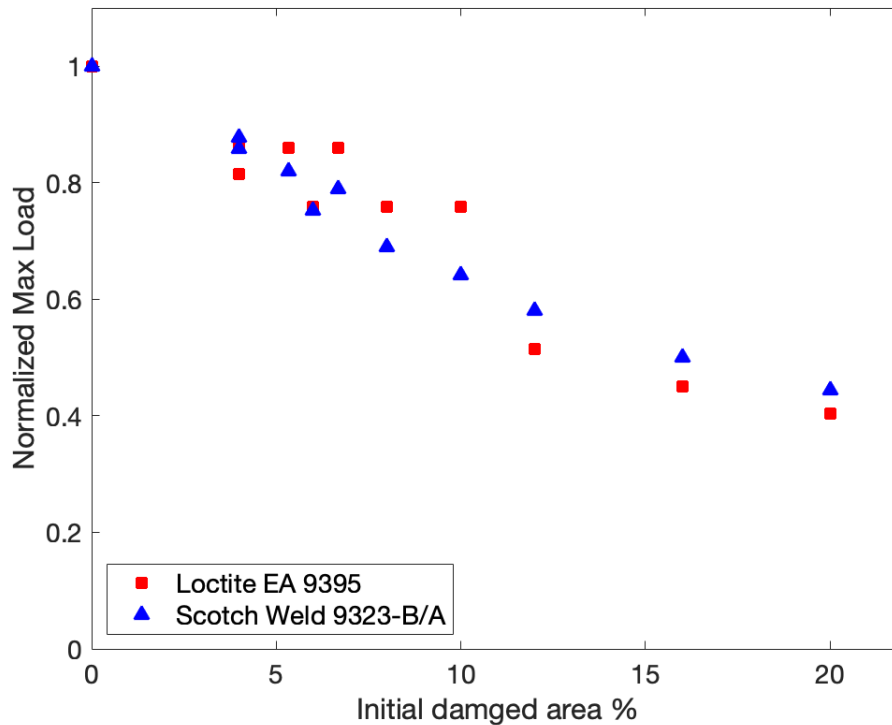


Figure 6.17 Comparative evaluation of normalized ultimate joint strength reduction as a function of increasing initial disbond area, extrapolated from FE numerical simulations.

The overall trend is a reduction of joint strength as the disbond increases. As confirmed by the experimental investigation of Engerer et al. [62], WSLs bonded joints characterized by a more brittle adhesive can withstand the same maximum load, although the initial damage increases. On the contrary, an almost continuous decrease is exhibited by a more ductile adhesive.

An interesting detail is shown in Figure 6.18, where the numerical results of the initial disbond area of 4% are pointed out. Indeed, different behavior is estimated for the adhesives.

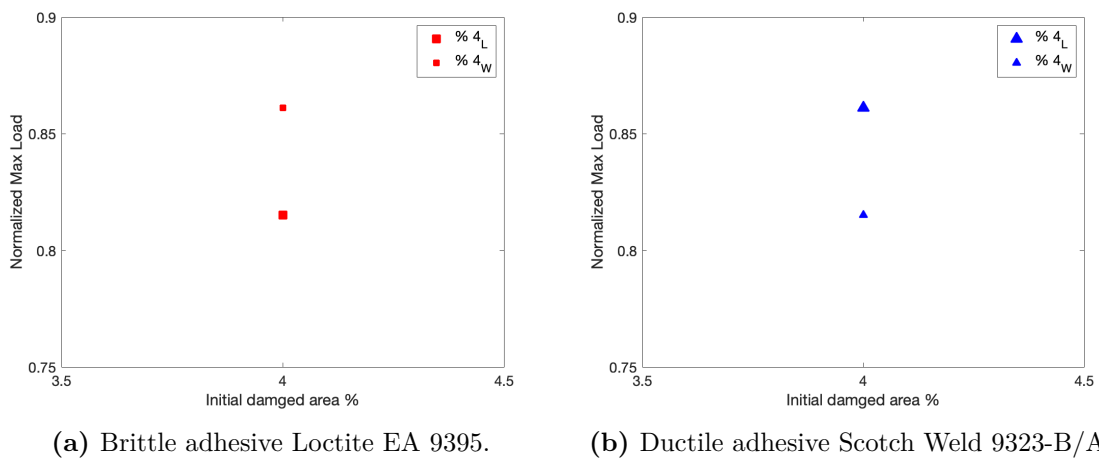


Figure 6.18 Particular detail of joint strength reduction for an initial disbond area of 4%, for Loctite EA 9395 and Scotch Weld 9323-B/A adhesives, extrapolated from FE numerical simulations.

Figure 6.18a highlights that for a brittle adhesive a full-length damaged bondline, i.e. disbond size 20x60 ($4_l\%$), is more critical than a wider but shorter disbond with the same initial damaged area, i.e. 60x20 ($4_w\%$). This confirms that the driving force of joint strength reduction for a brittle adhesive is the overlap leading edge. On the contrary, for a ductile adhesive (see Figure 6.18b) a wider but shorter disbond ($4_w\%$) has more severe consequence for the joint strength. This reduction results from ductile adhesive sensitivity to additional new edges in the bondline, which are deleterious for the bonded joint's load-carrying capability.

Thermoplastic WSLs welded joints

Over the past years, the possibility of replacing thermosetting-based composites with thermoplastic-based ones has been the focus of constant research effort in the aeronautical industry. In particular, the assessment of the thermoplastic welded longitudinal

joint is the major target for the project *Fuselage of Tomorrow*, of which Airbus is the leader. The numerical results presented in this thesis represent a small step forward in this field of research.

Unlike adhesively bonded joints, no extensive literature about thermoplastic welded joints is available to compare numerical estimates with experimental data, and the Lap Shear test campaign promoted by Airbus to specifically investigate welded longitudinal joints has not started yet. Nevertheless, some considerations can be made exploiting similarities with adhesive materials and results extrapolated from different types of thermoplastic-based composites welded configurations.

Figure 6.19 exploits the outcomes of numerical investigations to compare thermoplastic welded behavior to adhesively bonded configurations, in terms of strength reduction due to disbond presence in the joining line of WSLs reference joints. Table 6.1 provides a summary of the numerical outcomes.

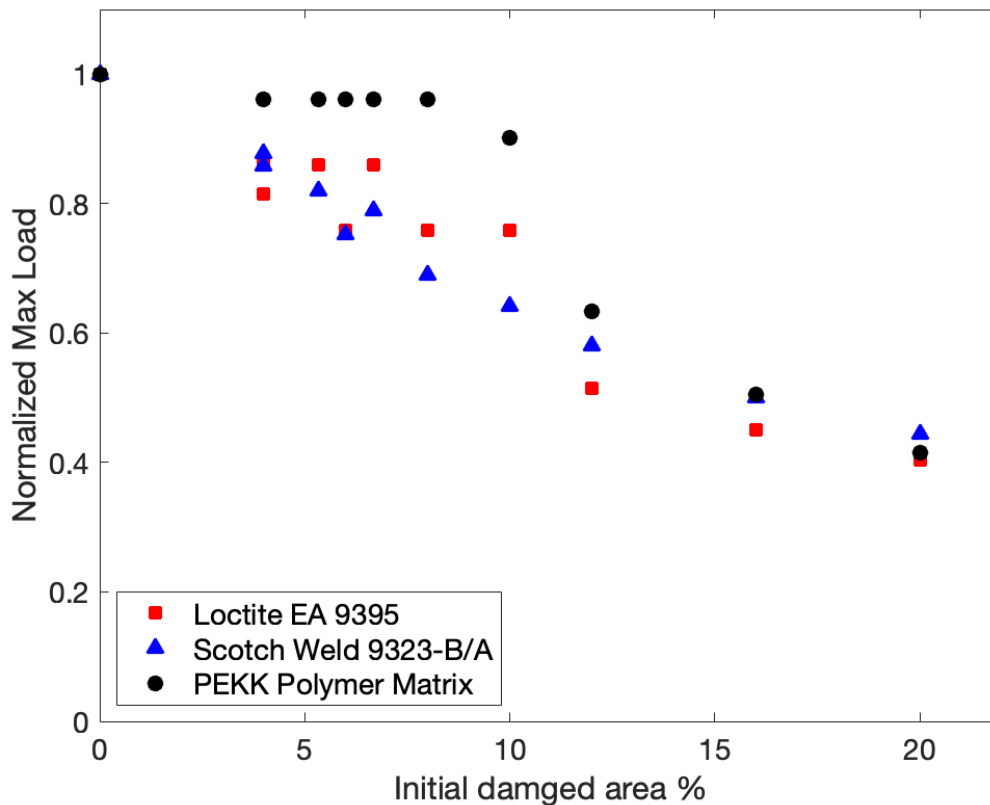


Figure 6.19 Comparative evaluation of normalized ultimate joint strength reduction as a function of increasing initial disbond area for WSLs bonded and welded joints, extrapolated from FE numerical simulations.

Table 6.1 Numerical results of ultimate joint strength for bonded and welded WSLS joints affected by different initial disbond areas.

Initial disbond area [%]	Ultimate joint strength [kN]		
	Loctite EA 9395	Scotch Weld 9323-B/A	PEKK
0	419.1	609.5	445.6
4_l	341.7	535.0	-
4_w	360.9	522.9	428.4
5.3	360.5	500.0	428.4
6	318.3	458.9	428.2
6.7	360.2	480.9	428.2
8	318.2	420.6	428.1
10	318.2	391.2	401.7
12	215.9	354.1	282.4
16	189.9	304.6	225.2
20	169.1	271.0	184.8

It is clear that for thermoplastic welded joints, small initial disbonded area does not affect the joint strength. Instead, a moderate drop is registered when the damaged site reaches about 10% of the total overlap region. It is deemed that thermoplastic welded joint behaves similarly to a more brittle adhesive, the weldline does not uniformly accommodate stress peak increases. Therefore, similar stress redistribution due to the presence of a disbond in the weldline leads to similar load-carrying capability reduction. Figure 6.20 illustrates the stress redistribution that takes place in the weldline when a disbond is present. No further stress increase is exhibited in the bondline until the damage reaches an initial disbonded area of 10%, which corresponds to the first drop in strength for a WSLS welded joint (see Figure 6.19).

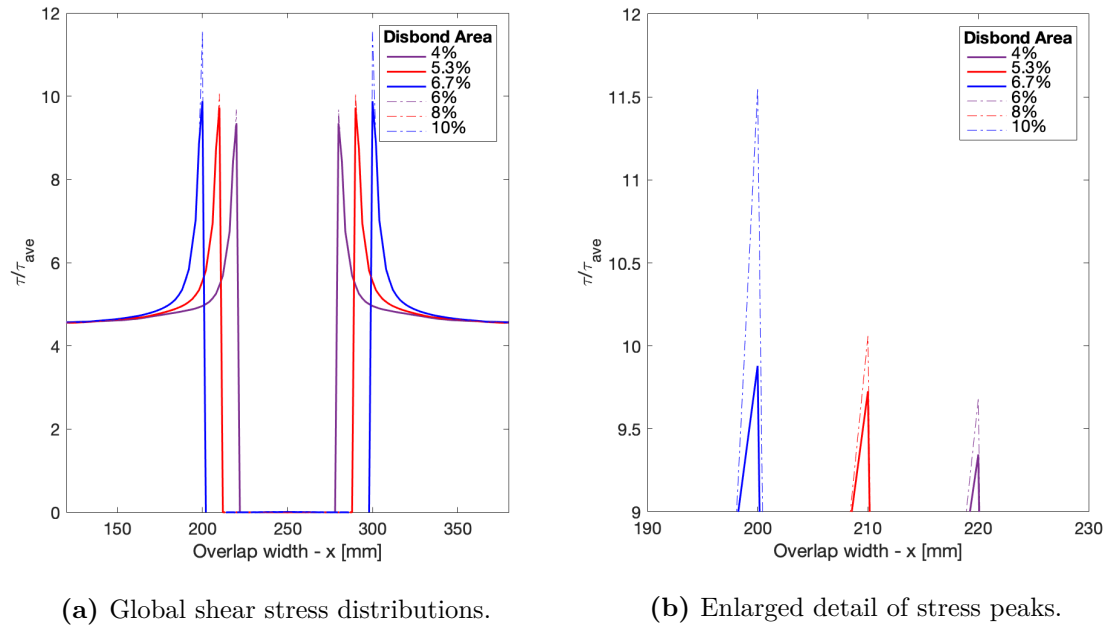


Figure 6.20 Normalized shear stress redistribution in the weldline of a WSLS joint as a function of several disbond sizes, extrapolated from FE numerical simulations.

Similar outcomes were found by Lai et al. [63], which studied the effect of defects on the failure of Medium Density Polyethylene (MDPE) specimens welded through fusion welding. The results obtained from tension test registered no joint strength reduction for damage size of 15% of the welded area. In contrast, a decrease of load-carrying capability is recorded for bigger defect sizes, up to 30%, and 45% of the weldline.

Vieille et al. [64] carried out a comparative study to assess the mechanical behavior of carbon fabric reinforced thermoplastic and thermoset laminates, under different environmental conditions. In particular, tensile tests were performed on notched and unnotched specimens. For both composites, an ultimate strength reduction of 50% was reached with a notch diameter equals to 20% of the specimen width. Comparable results are provided by numerical investigations carried out in this thesis. Indeed, a joint strength reduction between 42% and 46% was found as a result of an initial disbond area of 20% for thermoset WSLS bonded joints, and thermoplastic WSLS welded joints (see Figure 6.19).

It is clear that further researches and experimental tests need to be carried out to validate numerical models of a WSLS welded joint configuration, which aims to simulate a potential welded longitudinal joint of fuselage barrels.

6.2 Fatigue Numerical Predictions

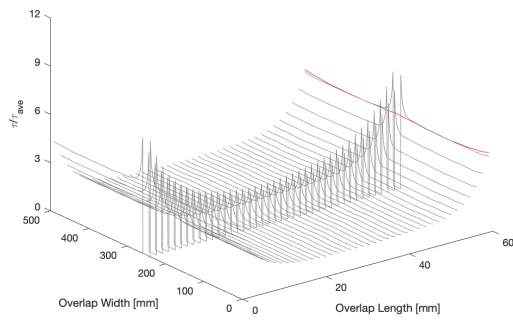
This Section delves into the numerical results of the proposed predictive methodologies for fatigue assessment. The aim is to exploit the outcomes of FE quasi-static analyses in order to predict fatigue response. It comes naturally that fatigue assessment requires experimental data to characterize a structural component completely. Therefore, based on the available data, the Similarity Principle approach, described in Section 5.2.1, is applied to WSLS bonded configurations characterized by Loctite EA 9593 adhesive, for which experimental result in terms of $S - N$ is extrapolated from BOPACS test campaign. On the contrary, the energy criterion explained in Section 5.2.2 is applied to WSLS bonded configurations with Scotch Weld 9323-B/A adhesive, which has been extensively characterized in terms of experimental mechanical and fatigue response within previous Airbus project.

For each proposed methodology, numerical estimates are presented along with a discussion about applicability and limitation. Finally, some considerations and suggestions for thermoplastic welded joints are proposed.

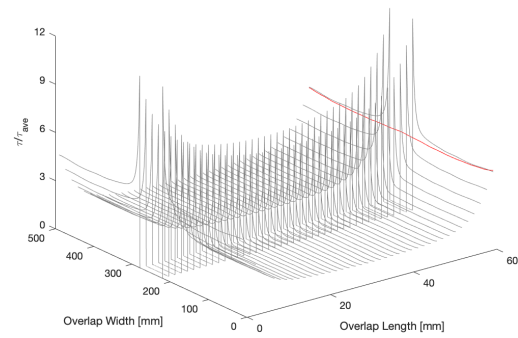
6.2.1 Constant Life Diagrams and Fatigue Strength

By following the methodology explained in Section 5.2.1, numerical predictions of fatigue strength for a constant life of $N_f \approx 7 \cdot 10^5$ are proposed for WSLS bonded joints, accounting for different initial disbond areas.

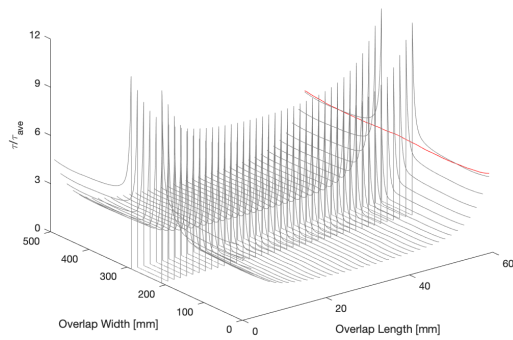
In order to apply the Similarity Principle, stress intensity factors K_t are extrapolated from FE quasi-static analyses by evaluating shear stress redistribution in the cohesive layer due to the presence of the damage. Figures 6.21 and 6.22 provide shear stress distribution in the cohesive layer of different damaged WSLS models, compared to the edge stress of a pristine configuration (red lines). Indeed, the model's geometrical properties are selected to guarantee that the far-field stress is not affected by the presence of the disbond. Stresses are normalized according to the average stress τ_{ave} , defined as the ratio between the applied load and the pristine bonded area. Peaks surround the local disbond, which acts as a stress raiser.



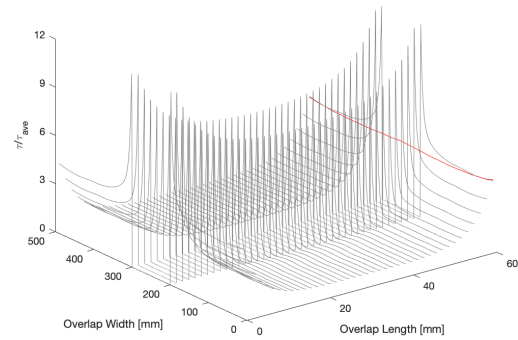
(a) Initial disbonded area 4%.



(b) Initial disbonded area 12%.

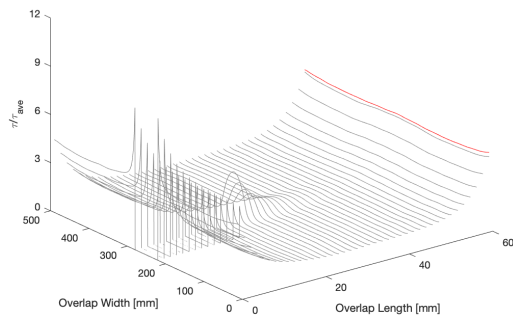


(c) Initial disbonded area 16%.

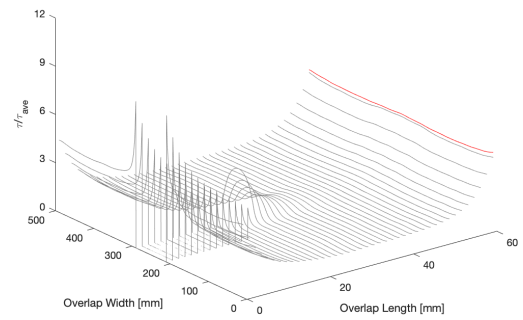


(d) Initial disbonded area 20%.

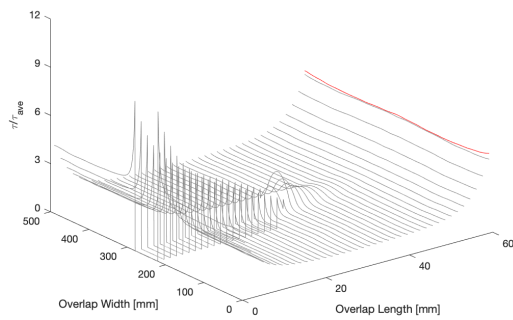
Figure 6.21 Normalized shear stress redistribution in the bondline of WSLs joints affected by different full-length disbond sizes. Red lines represent normalized shear stress distribution for a healthy bondline. Extrapolated from FE numerical simulations.



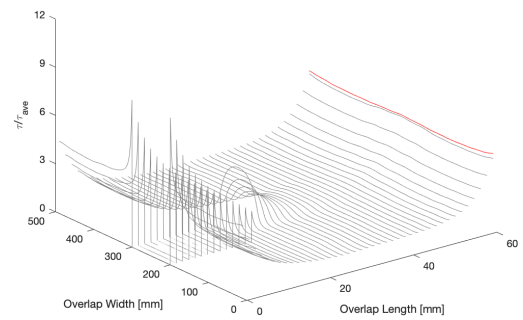
(a) Initial disbonded area 4%.



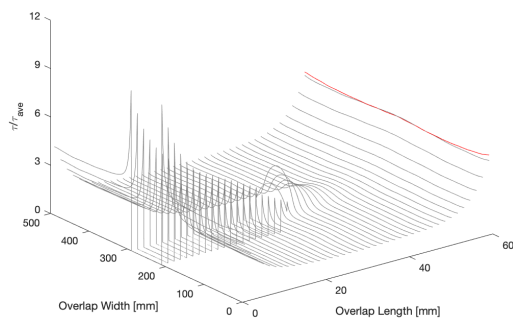
(b) Initial disbonded area 5.3%.



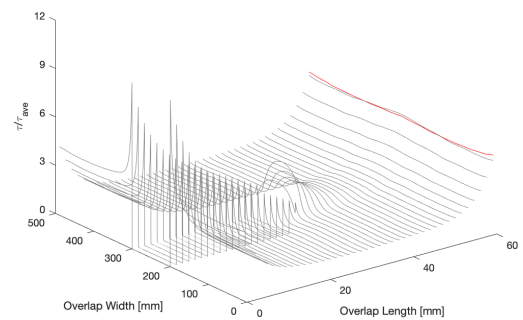
(c) Initial disbonded area 6%.



(d) Initial disbonded area 6.6%.



(e) Initial disbonded area 8%.



(f) Initial disbonded area 10%.

Figure 6.22 Normalized shear stress redistribution in the bondline of WSLs joints affected by several disbond sizes, with different combination of length and width. Red lines represent normalized shear stress distribution for a healthy bondline. Extrapolated from FE numerical simulations.

The most critical areas are the ends of the overlap, where the highest stress peaks are concentrated. Therefore, stress redistribution at the overlap edge is exploited to calculate the stress concentration factor K_t for each configuration. It is defined as the ratio between the peak stress value and the average stress value in the far-field. Figure 6.23 and Table 6.2 provide the results of the numerical estimated K_t . It is evident that increasing the disbond size leads to an increase of stress peaks. Nonetheless, it is interesting to note that an almost asymptotic value is reached as the damage approaches full-length size.

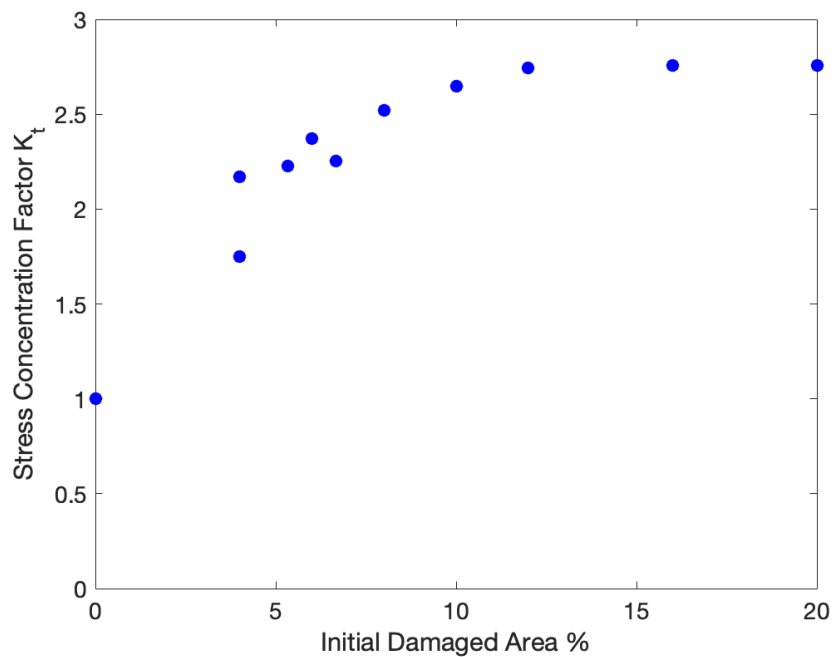


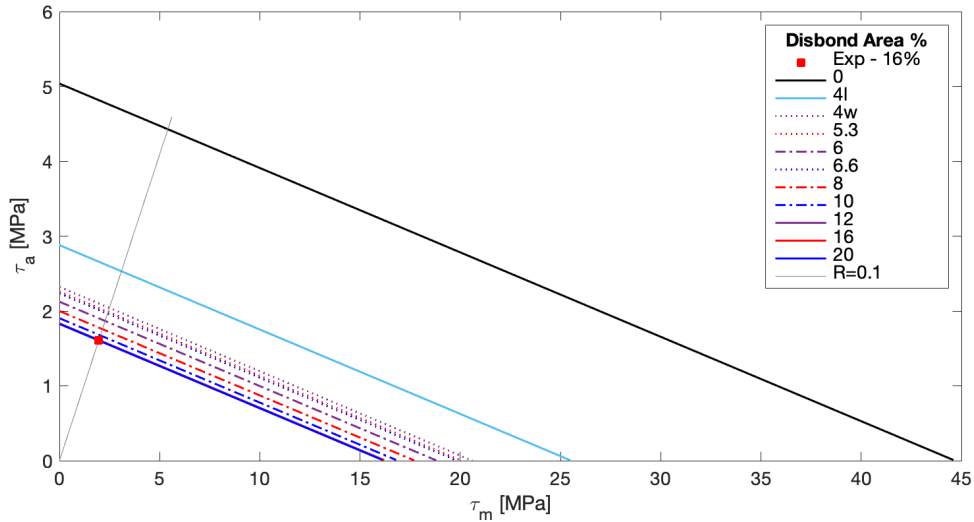
Figure 6.23 Stress concentration factors K_t for several WSLs joints affected by different initial disbond areas.

Table 6.2 Numerical evaluations of stress concentration factor K_t induced in the bondline of WSLs bonded joints due to the presence of initial disbonds.

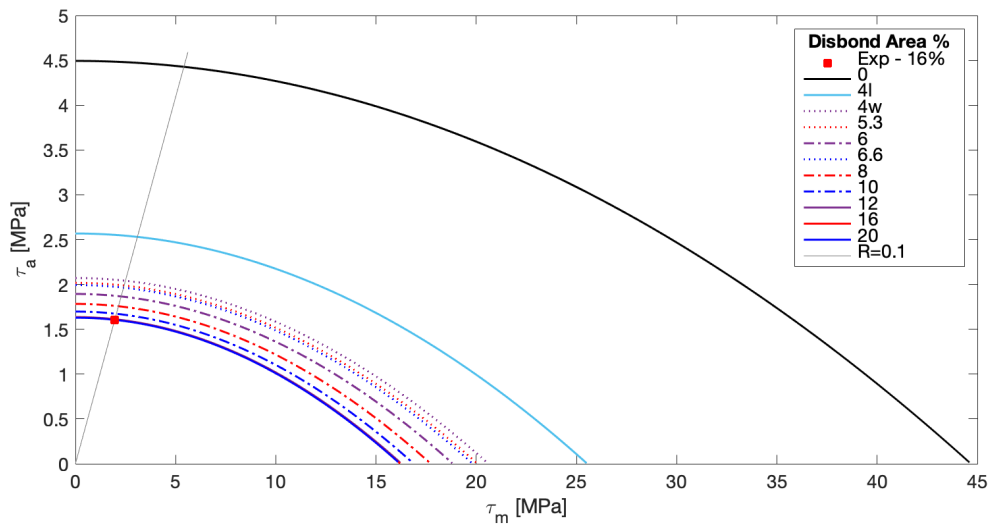
Initial disbond area [%]	0	4_l	4_w	5.3	6	6.7	8	10	12	16	20
K_t	1	1.75	2.17	2.23	2.37	2.25	2.52	2.65	2.74	2.75	2.76

Afterward, CLDs are estimated exploiting as starting point an experimental result from BOPACS test campaign, as explained in Section 5.2.1. Both Goodman relation and Gerber parabola are used to building the CLDs, which are provided in Figure

6.24. In particular, constant-life curves in 6.24a are derived from Eq. 5.1 (linear approximation), whereas Figure 6.24b shows constant-life curves according to Eq. 5.2 (parabolic approximation), starting from the same experimental outcome.



(a) Estimation of CLDs by exploiting Goodman linear relation.



(b) Estimation of CLDs by exploiting Gerber parabola relation.

Figure 6.24 Estimation of CLDs for $N_f \approx 7 \cdot 10^5$ accounting for several disbond sizes, by exploiting the Similarity Principle between damaged and pristine structural components.

Figure 6.25 provides fatigue strength estimations for different WSLs damaged configurations by exploiting CLDs and the Similarity Principle as predictive tools. The numerical results are summarized in Table 6.3.

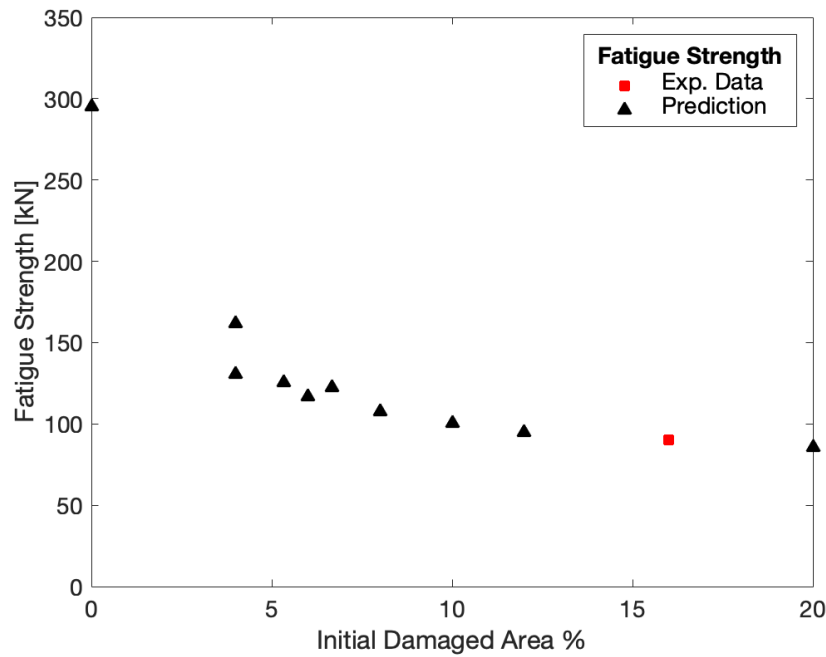


Figure 6.25 Fatigue strength predictions for both pristine and damaged WSLs bonded joints, for a fatigue lifetime of $N_f \approx 7 \cdot 10^5$ and $R = 0.1$, by exploiting the Similarity Principle.

Table 6.3 Numerical results of fatigue strength predictions for a fatigue lifetime of $N_f \approx 7 \cdot 10^5$ and $R = 0.1$, computed by exploiting the Similarity Principle.

Initial disbond area [%]	0	4_l	4_w	5.3	6	6.7	8	10	12	16	20
Fatigue strength predictions [kN]	295	162	131	126	117	122	108	100	95	-	85

It is concluded that it is possible to propose fatigue predictions by only means of one experimental test result and stress analysis extrapolated from FE quasi-static numerical simulations. In particular, fatigue strengths for a constant-life are predicted, accounting for several initially damaged configurations, which rely on the same baseline bonded joint, in terms of geometrical parameters and materials. The reduction of fatigue strength as initial disbond area increases follows the trend of stress concentration factor distribution illustrated in Figure 6.23.

The behavior of two WSLs joints with the same initial disbond area of 4%, but different combinations of disbond length and width, is noteworthy. As shown in Figures 6.21a and 6.22a, the stress distribution is different, and full-length damage, i.e. initial disbond area of $4_l\%$, is less affected by the presence of the damage in terms of stress peaks. Figure 6.26 provides a comparison of shear distribution at the overlap edge of

these WSLs bonded joints. Therefore, as for static strength reduction, also fatigue strength predictions are influenced by different disbond sizes. Nonetheless, according to ultimate strength prediction for Loctite EA 9395 adhesive, Figure 6.18a clearly shows that a full-length disbond causes a higher reduction in strength. On the contrary, in terms of fatigue strength, full-length disbond is less critical because it induces lower stress peaks in the bondline, as shown in Figure 6.26.

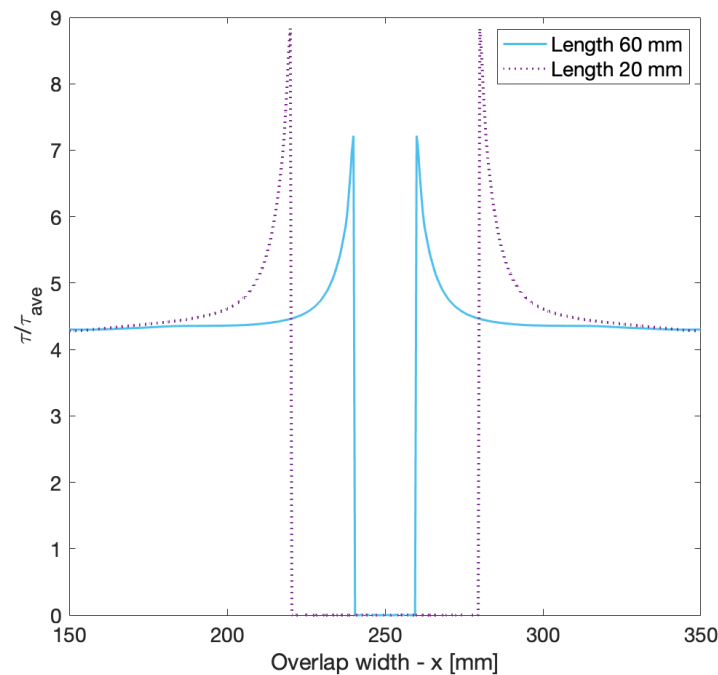


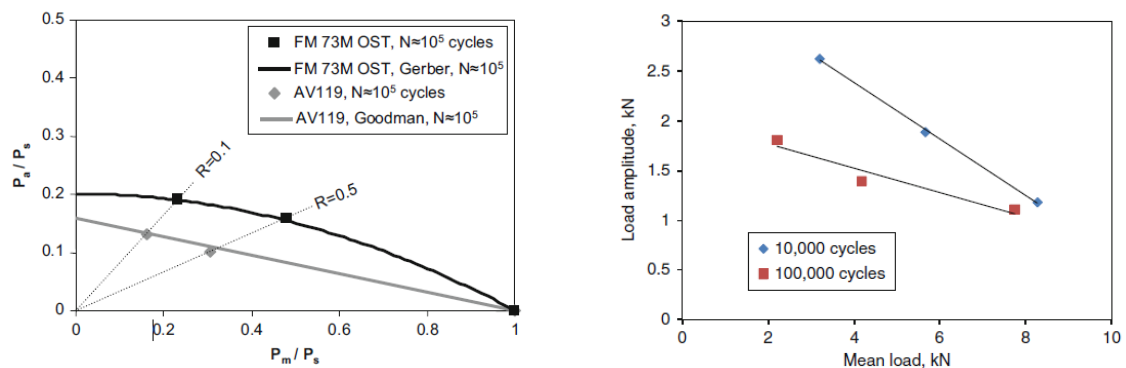
Figure 6.26 Shear stress distribution at the overlap edge of two WSLs damaged configurations characterized by the same initial disbanded area, but different damage orientation within the bondline. Extrapolated from FE numerical simulations.

Applicability and Limitation

CLDs are a well-known predictive tool for fatigue assessment. They are commonly used to analyze the influence of several loading parameters, such as load ratio, stress amplitude, or mean stress, on the fatigue life of a specific structural component. Suitable prediction models can be shaped according to experimental outcomes of basic cyclic loading setup, i.e. constant amplitude load. The most widespread analytical approaches, which are employed to estimate fatigue strength for a constant life, are Goodman linear approximation, and Gerber parabola, in particular for metals [52]. Nonetheless, over the past decade, experimental evidence showed that the previous

predictive models also fit quite well the influence of mean stress and stress ratio on fatigue response of adhesively bonded joints.

Khoramishad et al. [65] studied the influence of R -ratios on fatigue behavior of adhesively bonded SLJ for two different adhesive types, namely ductile and brittle. It was noted that depending on the adhesive properties, experimental outcomes of fatigue tests correlated well with either the Gerber parabola (ductile adhesive) or the Goodman linear approximation (brittle adhesive), as illustrated in Figure 6.27a. Crocombe et al. [66] investigated the effect of mean stress on fatigue limits of adhesively bonded SLJ. It was found that Goodman type curve fits quite well experimental outcomes of fatigue tests, as shown in Figure 6.27b. Both lines converge to the joint's static tensile strength when extrapolated downward to cross the zero-load amplitude fatigue condition. It was concluded that the response of an adhesively bonded joint at different R -ratios could be assessed by an extrapolatory predictive procedure starting from fatigue data obtained for a single load ratio. Therefore, both Goodman linear approximation and Gerber parabola have been proven to be suitable predictive tools for adhesively bonded joints to assess the influence of different parameters on fatigue response.



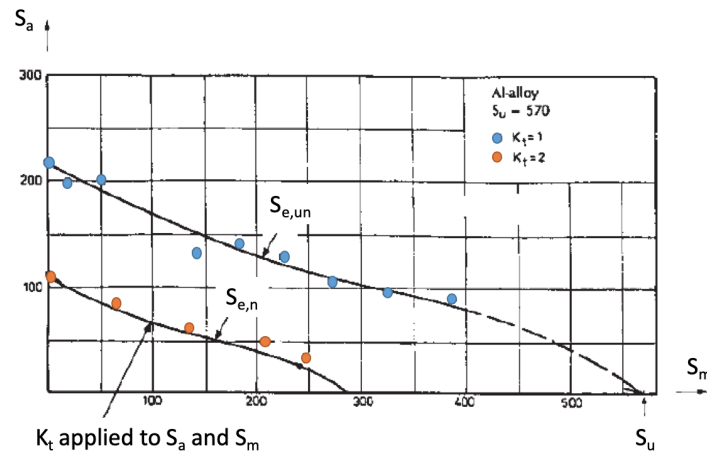
(a) Constant life diagrams for ductile adhesive FM 73 M OST, and brittle adhesive AV119. Data from Khoramishad et al. [65].

(b) Goodman type curves for SLJ for various fatigue lives. Data from Crocombe et al. [66].

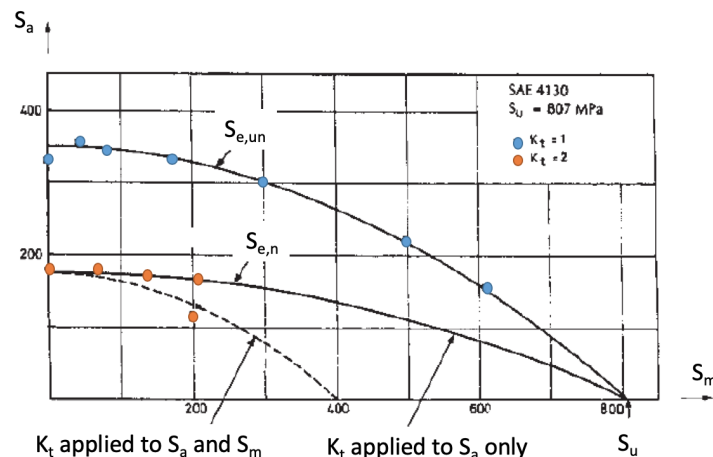
Figure 6.27 CLDs of adhesively bonded joints extrapolated from fatigue test results by means of both Goodman and Gerber analytical approximations exploited as predictive models.

Nevertheless, no experimental investigation has been carried out yet on the applicability of the Similarly Principle on adhesively bonded joints with artificial disbonds. This methodology has been applied to different materials, providing reasonable fatigue strength predictions compared to experimental outcomes. Figure 6.28 provides two examples of constant-life fatigue diagrams with experimental fatigue data of notched

and unnotched specimens made of a high-strength Al-alloy with low ductility, and a moderately ductile low-alloy steel [56], respectively.



(a) Experimental fatigue strength results for $K_t = 1$ and $K_t = 2$ for a high-strength Al-alloy. Goodman relation is used to fit the data. Data from Schijve [56].



(b) Experimental fatigue strength results for $K_t = 1$ and $K_t = 2$ for a moderate ductile steel alloy. Gerber relation is used to fit the data. Data from Schijve [56].

Figure 6.28 Examples of CLDs with experimental fatigue strength data of notched and unnotched specimens. Blue dots refer to fatigue strength of unnotched specimens, whereas red dots to fatigue response of notched configurations. Data from Schijve [56].

For the high-strength Al-alloy, Goodman linear relation fits the curve reasonably well, as illustrated in Figure 6.28a. On the contrary, Gerber parabola represents a better fit for a more ductile alloy, as shown in Figure 6.28b. Obviously, mean stress affects fatigue response, but not in a regular analytical way since scatter of experimental data

can be noted. For notched specimens, it is clear that for the high-strength Al-alloy, the Similarity Principle application provides reasonable results in terms of fatigue strength predictions, which are in good agreement with the experimental outcomes (see Figure 6.28a). On the contrary, for a steel alloy with a higher grade of ductility, a modified Gerber parabola, which accounts for application of K_t to stress amplitude S_a only, agrees better with experimental fatigue data for notched specimens. This behavior can be addressed to material ductility, which leads to large plastic deformation at notch roots before failure. Therefore, to validate and improve the proposed approach based on stress similarity, more experimental fatigue data are necessary.

The last parameter that should be taken into account to provide more accurate fatigue strength predictions is the notch sensitivity factor q . Indeed, the outcomes of several experimental fatigue tests on notched specimens revealed that the reduction factor due to fatigue is smaller than K_t [56]. This factor is commonly called the fatigue notch factor K_f , and the relation between these three parameters can be expressed as follows:

$$q = \frac{K_f - 1}{K_t - 1} \quad (6.1)$$

Therefore, applying the Similarity Principle exploiting K_t may lead to too conservative results depending on the notch sensitivity of the adhesive under examination.

Prabhakaran et al. [67] investigated the influence of notches on the fatigue strength of a brittle and a ductile epoxy. The first one exhibited a very high notch sensitivity for sharper and intermediate notches. The second one showed a high notch-strengthening effect for big notches. Therefore, it is evident that further investigations are needed to assess the fatigue behavior of the Loctite EA 9395 adhesive. This characterization is fundamental to take into consideration all the fundamental parameters requested for the proposed methodology and to avoid too conservative fatigue strength estimates.

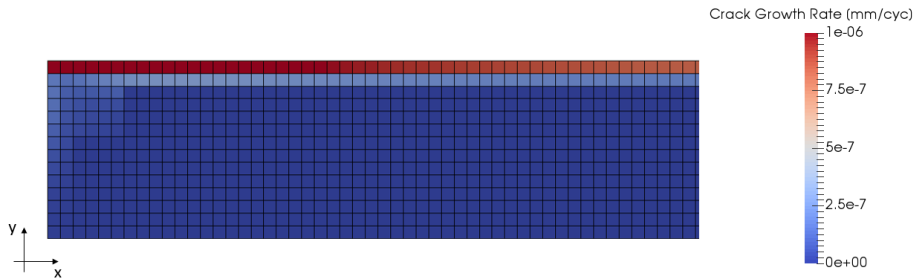
6.2.2 Energy Criterion and Fatigue Lifetime

This Section provides the numerical prediction of fatigue initiation load and fatigue lifetime for three WSLs bonded joints with Scotch Weld 9323-B/A adhesive, for which experimental fitting data for Paris's law are available from previous Airbus internal project.

For a pristine WSLs bonded configuration, the no-growth load level is estimated to be 140 kN, which corresponds to 23% of the joint's static strength. Figure 6.29 shows the crack growth rate distribution in the bondline.



(a) Pristine bondline. The black rectangle frames one of the most critical areas for damage initiation, which is exploited to illustrate fatigue crack growth rate distribution.



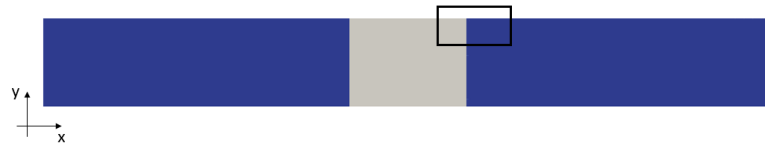
(b) Detail of left-side corner of the adhesive layer as representative case of most critical areas.

Figure 6.29 Fatigue crack growth rate da/dN in the adhesive layer of a pristine WSLs bonded joint at 140 kN, which is the estimated no-growth load level.

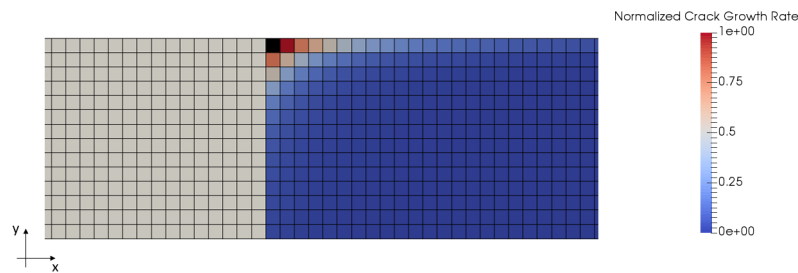
As expected, free edges corners of the adhesive layer identify the areas which are more prone to be affected by fatigue damage initiation. No-growth load level estimate is deemed reasonable compared to experimental investigations carried out on bonded joints characterized by thermosetting-based laminated composites, which indicate a range between 15% and 40% for fatigue limit [15, 54, 55]. Indeed, also for a WSLs bonded joint with adhesive Loctite EA 9395, subjected to fatigue test within BOPACS campaign, the no-growth load level was found at 28% of the static strength.

Afterward, fatigue initiation load is estimated for two WSLs bonded joints affected by initial disbond within the adhesive layer. According to the proposed methodology

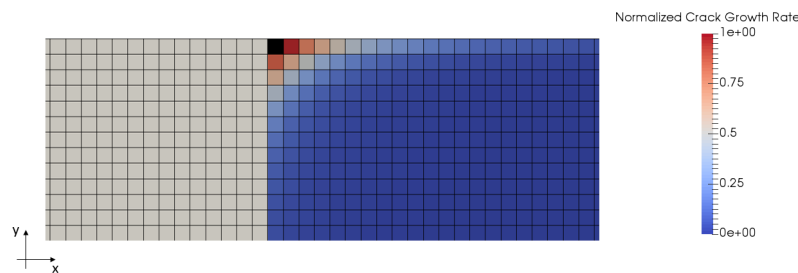
explained in Section 5.2.2, as soon as one finite element in the adhesive layer exceeds the threshold $(da/dN)_{th}$ for a certain applied load, that level represents the minimum P_{max} requested in a fatigue test setup to trigger fatigue damage initiation. For both configurations, which are affected by 12% and 16% initial disbond area, 110 kN represents the minimum load level that ensures fatigue damage initiation. Figure 6.30 shows the fatigue crack growth rate distribution within adhesive layers influenced by the presence of disbond.



(a) Schematic illustration of WSLS bondline affected by the presence of a disbond (in white). The black rectangle frames one of the most critical areas for damage initiation, which is exploited to illustrate fatigue crack growth rate distribution.



(b) Detail of da/dN distribution in the adhesive layer affected by an initial disbonded area of 12%.



(c) Detail of da/dN distribution in the adhesive layer affected by an initial disbonded area of 16%.

Figure 6.30 Fatigue crack growth rate da/dN in the adhesive layer of two WSLS bonded configurations with initial disbonds at 110 kN, which represents the fatigue initiation load.

In this case, the most critical areas are identified by disbond corners, which cause stress increases in the bondline and represent a natural trigger for damage initiation. Figures 6.30b and 6.30c illustrate detailed da/dN distribution around damage corner

for the adhesive layer affected by an initial disbonded area of 12% and 16%, respectively. In addition, to ensure that the estimate load triggers fatigue damage initiation only around the initial disbond, an additional check was added to monitor the fatigue crack growth rate at overlap ends. Indeed, da/dN at the edges of the bondline must not exceed the limit of $1 \cdot 10^{-6}$ mm/cyc. It represents the threshold value for the pristine configuration, in order to avoid crack initiation from overlap free ends.

It is interesting to note that the estimated P_{max} of 110 kN, which ensures fatigue damage initiation, corresponds to 78% of the no-growth load level, which indicates another similarity with BOPACS experimental setup, even if the adhesive used is different. Indeed, during the fatigue test of damaged WSLs bonded joints in BOPACS test campaign, the maximum applied load level of 90 kN was selected by engineering judgment, and it corresponds to 75% of no-growth level.

Finally, fatigue lifetime predictions are carried out by exploiting the methodology summarized in Figure 5.12, which accounts only for the steady Region II. The applied load level P_{max} is 110 kN, as it is estimated to be the minimum load level that can trigger fatigue crack initiation. A new FE quasi-static simulation is performed with an increased artificial disbond after each interaction, according to the calculated width increment Δa . The rupture criterion is met at $3.7 \cdot 10^6$ cycles and $1.5 \cdot 10^6$ cycles for WSLs bonded joints with initial disbond areas of 12% and 16%, respectively. Results of the proposed methodology are provided in Figure 6.31, in which crack growth is normalized according to the maximum estimated crack width.

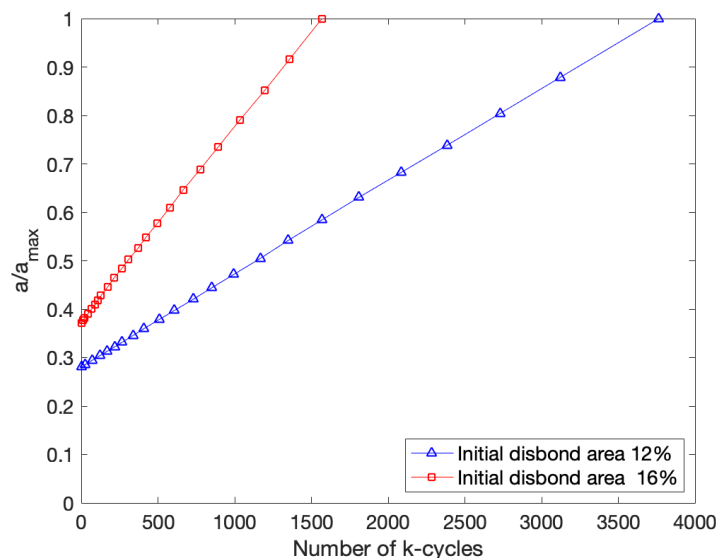


Figure 6.31 Fatigue lifetime prediction for WSLs bonded joints affected by initial disbonds of 12% and 16%, as a function of crack increment.

It should be highlighted that no direct comparison can be carried out with experimental results from BOPACS campaign, since the adhesive used for the numerical simulation is different from the one used for fatigue testing. Indeed, the adhesive's mechanical properties influence the behavior of bonded joints and may lead to dissimilar fatigue response [68].

Tomblin et al. [69] carried out experimental fatigue testing on SLJs characterized by brittle and ductile adhesives to assess the long-term durability of adhesively bonded joints. Fatigue tests conducted under room temperature ambient (RTD) showed that for the same applied percentage of ultimate strength, the ductile adhesive globally failed at a higher number of cycles than the brittle one. However, no extensive data are available in the literature to fully support this statement. Further testing is clearly necessary to assess the fatigue response of SLJs made of different adhesives.

Applicability and Limitation

Exploiting energy criterion and LEFM assumption is a well-established predictive tool for fatigue lifetime, expressed in terms of number of cycles up to failure. Indeed, much effort has been made to model fatigue crack propagation in adhesively bonded joints over the past years employing FE analysis. In particular, the CZM technique represents the focus of many studies because traction-separation law can be manipulated to account for fatigue damage accumulation. Simulation of cyclic loading scenario and extension of cohesive constitutive response require a user-defined subroutine for explicit-time integration, which is out of the scope of these studies. Indeed, this thesis aims to assess whether or not numerical results provided only by FE quasi-static analysis can be exploited for basic fatigue predictions.

The proposed methodology based on energy criterion and fatigue crack growth approach allows first level estimation, such as predictions of the no-growth load level and fatigue initiation load. The second step is represented by fatigue lifetime estimation, which, in case of constant amplitude stress, can be expressed in a closed form, as described in Section 5.2.2. A similar approach has been adopted by Liu et al. [37], which estimated fatigue lifetime of a debonded wide lap joint by running several FE quasi-static analyses with different crack lengths to extrapolate ΔG and numerically integrate the fitting Paris's law. Numerical outcomes in terms of fatigue life prediction showed good agreement with test measured results for adhesion debonding.

Nevertheless, in this thesis, some assumptions have been adopted to simplify the problem, characterized by complex geometry and three-dimensional stress state. For FE numerical analyses, only the crack extension in the width direction has been taken

into account. This implies that the curved crack fronts defined by ultrasonic inspection performed during BOPACS fatigue test are approximated as straight lines. Obviously, this assumption may lead to more conservative estimation since the adhesively bonded joint is affected by a more significant increase in disbond area. The second simplification lies in the assumption that for WSLS bonded joints characterized by the same initial disbond area, but with different adhesive material, the fatigue crack growth rate experienced during the steady growth phase could be comparable. To overcome the lack of experimental data about a WSLS bonded configuration with Scotch Weld 9323-B/A adhesive, this assumption is deemed reasonable for a feasibility approach study. It comes naturally that more experimental data are necessary in order to validate and improve the proposed methodology.

6.2.3 Methodological Proposals for Welded Joints

Experimental data are a fundamental background for any type of fatigue assessment, e.g. load limits, fatigue lifetime, effect of defects, environmental parameters, or material properties. Therefore, based on the predictive tools proposed in this thesis and the type of experimental data required as starting points, some proposals in terms of test requests can be made to begin with the experimental assessment of thermoplastic welded joints.

Besides ultimate static strength experimental validation, extensive characterization of the thermoplastic matrix is necessary to perform FE simulations. Indeed, material input properties strongly influence the numerical investigation outcomes. In particular, the CZM used to simulate the welding line between thermoplastic-based laminated composites is extremely sensitive to the parameters used to define the traction-separation law. They not always have physical significance and need to be adjusted based on experimental test outcomes.

Subsequently, the experimental characterization of fatigue behavior is strongly necessary for thermoplastic welded joints. So far, this topic is still being researched [70, 71], concerning not only mechanical and fatigue behavior, but also welding technologies with related process parameters. Material thresholds for damage propagation need to be defined in terms of no-growth load levels to allow a preliminary understanding of fatigue limits. Then, changes in fatigue response due to the presence of disbond in the weldline can be assessed through experimental tests, which can be used to validate the proposed procedure by exploiting the Similarity Principle. Finally, with an accurate characterization of thermoplastic matrix properties, the CZM can be

improved to properly simulate the fracture process due to fatigue damage initiation and propagation.

Thermoplastic welding technology is a must for future generations of aircraft to enhance performances, reduce maintenance costs, and increase the production rate. Therefore, besides continuous effort to improve thermoplastic welding techniques, experimental tests are a fundamental background to define static and fatigue responses of welded joints, and to validate all types of numerical methodologies.

Chapter 7

Conclusions

The purpose of this thesis is to numerically investigate the effect of manufacturing-induced defects, such as weak bond or disbond, on the performance of new potential boltless design for fuselage panels longitudinal joint, which is typically identified as a HLT joint. Two different boltless joining techniques are examined, namely adhesive bonding and welding, employed to join thermosetting-based and thermoplastic-based laminated composites, respectively.

State-of-art longitudinal joints of the fuselage of Airbus A350-XWB aircraft family are taken as baseline reference design for this work. Currently, these joints are carried out by conventional mechanical fastening of two CFRP composite panels simply overlapping, i.e. SLJ. A WSLJ specimen, previously adopted as test setup within BOPACS project, is numerically modeled in the commercial FE software Abaqus to simulate a HLT joint to ensure compatibility with potential experimental investigations. The CZM technique is exploited to define the joining line of bonded and welded joints, and numerically simulate the damage growth driven by fracture energies.

The main objective of this work is to carry out a comparative numerical evaluation of the effect of defects on the joint performances, in terms of ultimate strength reduction and fatigue response. This assessment involves several initial disbond artificially simulated in the numerical models. It also examines the different behaviors of the materials used to join the composite adherends when a defect is present in the joining line. Quasi-static numerical analysis is exploited as a computational loading scenario.

7.1 Summary of Research Results

Three different classes of joining line materials were investigated to assess the effect of defects on joint load-carrying capability. Two types of adhesive were used to simulate

the bondline of WSLS bonded joints, namely brittle adhesive EA 9395 and ductile adhesive Scotch Weld 9323-B/A. In contrast, a thermoplastic polymer matrix PEKK modeled the weldline of WSLS welded joints. Globally, numerical outcomes indicated a reduction of ultimate joint strength whenever a disbond occurred in the joining line. Nevertheless, each material exhibited a different trend of reduction depending on the initial damage size and position. It was related to diverse responses to deformation and stress resulting from inherent material mechanical properties.

For the brittle adhesive, the joint strength reduction was mainly governed by overlap ends, since this type of adhesive experienced significant stress peaks increases due to the presence of damages. Therefore, if the initial disbond did not approach both overlap leading edges, i.e. full-damaged overlap length, the load-carrying capability was not markedly reduced. On the contrary, the ductile adhesive showed a high sensitivity to edge effects and accommodated a slightly more effective stress distribution within the bondline due to the presence of damage. Therefore, whenever a disbond occurred in the bondline, the adhesive layer was affected by the introduction of additional free edges. This led to a continuous load-carrying capability reduction regardless of the position of the disbond in the bondline. Thermoplastic welded joints affected by initial defects of the weldline showed a distinctive trend of strength reduction. Numerical outcomes highlighted that a small initial disbonded area did not affect the joint load-carrying capability. The first strength drop occurred when the disbond reached an area of 10% of the entire overlap region.

The comparison of numerical investigations concluded that in terms of ultimate joint strength, the performance of boltless joints affected by joining line defects is strongly influenced by the type of materials used to join the composite adherends.

To delve into the influence of disbonds on the fatigue response of boltless joints, two methodological approaches were proposed as predictive tools to exploit numerical outcomes of FE quasi-static analyses. The investigations focused on adhesively bonded joints for which experimental fatigue data were available.

Based on the Similarity Principle of stress peaks distribution, a reverse approach was proposed to predict fatigue limits of several damaged WSLS bonded configurations for constant fatigue life. The experimental fatigue test result of a WSLS specimen affected by an initial disbond area of 16% was extrapolated from BOPACS campaign, in which the adhesive EA 9395 was employed as bonding layer. This data was used as a starting point to numerically extrapolate the CLDs based on two simple fitting equations proposed in the literature, namely Goodman equation and Gerber parabola. By evaluating FE numerical outcomes in terms of stress redistribution in the damaged

bondline, the stress concentration factors were computed and exploited to scale the CLDs according to the severity of the disbond effect. For a constant life, fatigue limits increased as the disbond area gradually reduced.

The second methodology proposed to predict fatigue response was based on the energy criterion that represents the basis of the FCG approach. It allowed an estimation of both fatigue initiation loads and cracks extension as a function of fatigue life expressed in terms of number of cycles to failure. FCG approach exploits the correlation between the fatigue crack growth rate due to cycling loading and the strain energy release rate amplitude ΔG . From FE modeling, ΔG was evaluated for the cohesive elements of the adhesive layer and used to calculate the crack growth rate according to an experimentally defined Paris's law for the adhesive Scotch Weld 9323-B/A. Threshold crack growth rate values were extrapolated from BOPACS test campaign to establish fatigue initiation. For a pristine WSLS bonded joint, the no-growth load level was estimated about 23% of the ultimate joint strength, which falls in the typical fatigue limit range for adhesively bonded joints. For two WSLS joints affected by an initial disbond area of 12% and 16%, respectively, a fatigue initiation loads of about 78% of the no-growth load level were predicted. Similar outcomes were previously found within BOPACS experimental investigations. Fatigue lifetime predictions were carried out by running several FE quasi-static analyses with different crack extensions to extrapolate ΔG and numerically integrate Paris's law. The rupture is reached at $3.7 \cdot 10^6$ cycles and $1.5 \cdot 10^6$ cycles for WSLS bonded joints with initial disbond areas of 12% and 16%, respectively.

Based on these investigations, the exploitation of FE quasi-static simulations to predict fatigue response is concluded to be feasible for preliminary assessment of structures fatigue behavior.

7.2 Proposals for Future Works

The work done in this thesis is limited to computational simulations carried out by commercial FE software focusing on the quasi-static loading scenario. Assumptions have been adopted to simplify the problem, characterized by complex geometry and different materials interfaces. No specimens manufacturing or experimental testing has been conducted in the time frame of this study. Therefore, this offers several proposals for future works to improve numerical modeling and validate predictive methodologies.

The implementation of reliable FE models is strongly dependent on the accuracy of input parameters. Hence, in particular, for potential longitudinal welded joints, an in-

depth and extensive experimental characterization of thermoplastic matrix mechanical properties could further improve the predictive capabilities of numerical analyses. Indeed, to enable a reliable fracture behavior of cohesive elements, material properties required to define the traction-separation law should be evaluated from the fitting of experimental results obtained by testing Double Cantilever Beam (DBC) and End-Notched Flexure (ENF) specimens.

The FE model of boltless joints developed in this study only accounts for the cohesive failure of the joining line. Actually, several failure modes may occur whenever laminated composites materials are employed. Therefore, a further step towards a comprehensive understanding of joint performance could be the implementation of composite adherends interlaminar fracture to investigate the effect of different lay-up sequences.

With the potential perspective of fully boltless joining of primary aircraft structures, it comes naturally to the necessity of more experimental testing to assess the behavior of this type of joints, in particular in terms of fatigue response. Subsequently, numerical models should be formulated and improved according to the experimental outcomes to enhance their predictive capabilities. Both methodological approaches proposed in this work should be validated through experimental testing and further improved to fit the test outcomes better.

References

- [1] KI Tserpes, Jacques Cinquin, and Sp Pantelakis. “On the mechanical performance of noncrimp fabric H-shaped adhesively bonded joints”. In: *Journal of composite materials* 45.15 (2011), pp. 1607–1619.
- [2] Airbus. “Special Edition: A350 XWB”. In: *Airbus Technical Magazine - FAST: Flight Airworthiness Support Technology* (2013).
- [3] Theodor A Schmid Fuertes et al. “Bonding of CFRP primary aerospace structures - discussion of the certification boundary conditions and related technology fields addressing the needs for development”. In: *Composite Interfaces* 22.8 (2015), pp. 795–808.
- [4] DN Markatos et al. “The effects of manufacturing-induced and in-service related bonding quality reduction on the mode-I fracture toughness of composite bonded joints for aeronautical use”. In: *Composites Part B: Engineering* 45.1 (2013), pp. 556–564.
- [5] MD Banea and Lucas FM da Silva. “Adhesively bonded joints in composite materials: an overview”. In: *Proceedings of the Institution of Mechanical Engineers, Part L: Journal of Materials: Design and Applications* 223.1 (2009), pp. 1–18.
- [6] Al Higgins. “Adhesive bonding of aircraft structures”. In: *International Journal of Adhesion and Adhesives* 20.5 (2000), pp. 367–376.
- [7] *Boltless assembling Of Primary Aerospace Composite Structures*. URL: <https://cordis.europa.eu/project/id/314180> (visited on 05/01/2020).
- [8] *The next generation Multifunctional Fuselage Demonstrator — leveraging thermoplastics for cleaner skies*. URL: <https://www.cleansky.eu/the-next-generation-multifunctional-fuselage-demonstrator-leveraging-thermoplastics-for-cleaner> (visited on 05/01/2020).
- [9] PM Mohite. *Aircraft Basic Construction*. MOHITE, PM IITK-Indian Institute of Technology Kanpur: Home Page of Dr. PM Mohite. 2018.
- [10] Airbus Operations GmbH et al. *Reference Structure Design Principles for A350 XWB Volume 4 - Fuselage Design Principles*. 2017.
- [11] Sp Pantelakis and KI Tserpes. “Boltless joining of composite aerostructures: From secondary to primary parts”. In: ().
- [12] KI Tserpes, R Ruzek, and Sp Pantelakis. “Strength of Pi shaped non-crimp fabric adhesively bonded joints”. In: *Plastics, rubber and composites* 41.2 (2012), pp. 100–106.

-
- [13] Somen K Bhudolia et al. “Advances in Ultrasonic Welding of Thermoplastic Composites: A Review”. In: *Materials* 13.6 (2020), p. 1284.
- [14] Ali Yousefpour, Mehdi Hojjati, and Jean-Pierre Immarigeon. “Fusion bonding/welding of thermoplastic composites”. In: *Journal of Thermoplastic composite materials* 17.4 (2004), pp. 303–341.
- [15] Robert D Adams. *Adhesive bonding: science, technology and applications*. Elsevier, 2005.
- [16] Flake C Campbell Jr. *Manufacturing processes for advanced composites*. elsevier, 2003.
- [17] S Budhe et al. “An updated review of adhesively bonded joints in composite materials”. In: *International Journal of Adhesion and Adhesives* 72 (2017), pp. 30–42.
- [18] *Thermoplastic Composites to Play Enhanced Role in Next-Generation Aerospace Applications*. URL: <https://www.aerodefensetech.com/component/content/article/adt/features/articles/34123> (visited on 05/01/2020).
- [19] Martine Dubé. “Static and fatigue behaviour Of thermoplastic composite laminates joined by resistance welding”. PhD thesis. McGill University Montreal, Canada, 2007.
- [20] Irene Fernandez Villegas and Genevieve Palardy. “Ultrasonic welding of CF/PPS composites with integrated triangular energy directors: melting, flow and weld strength development”. In: *Composite Interfaces* 24.5 (2017), pp. 515–528.
- [21] NS Taylor, SB Jones, M Weld, et al. “The feasibility of welding thermoplastic composite materials”. In: *Construction and Building Materials* 3.4 (1989), pp. 213–219.
- [22] F Becker and H Potente. “A step towards understanding the heating phase of laser transmission welding in polymers”. In: *Polymer Engineering & Science* 42.2 (2002), pp. 365–374.
- [23] Darko Stavrov, Giovanni Nino, and Harald Bersee. “Process optimization for resistance welding of thermoplastic composites”. In: *47th AIAA/ASME/ASCE/AHS/ASC Structures, Structural Dynamics, and Materials Conference 14th AIAA/ASME/AHS Adaptive Structures Conference 7th*. 2006, p. 2246.
- [24] Ginger Gardiner. “Thermoplastic composites gain leading edge on the A380”. In: *High Performance Composites* 14.2 (2006), p. 50.
- [25] *What Are Plastic Welding Defects?* URL: <https://d-dplastics.com/2017/07/what-are-plastic-welding-defects/> (visited on 05/01/2020).
- [26] Pedro Ochôa et al. “Diagnostic of manufacturing defects in ultrasonically welded thermoplastic composite joints using ultrasonic guided waves”. In: *NDT & E International* 107 (2019), p. 102126.
- [27] FMF Ribeiro et al. “Strength and damage growth in composite bonded joints with defects”. In: *Composites Part B: Engineering* 100 (2016), pp. 91–100.
- [28] EF Karachalios, RD Adams, and Lucas FM da Silva. “Strength of single lap joints with artificial defects”. In: *International Journal of Adhesion and Adhesives* 45 (2013), pp. 69–76.
-

-
- [29] Uday Shanker Dixit and R Ganesh Narayanan. *Strengthening and Joining by Plastic Deformation: Select Papers from AIMTDR 2016*. Springer, 2018.
- [30] Tsuey T Wang, FW Ryan, and H Schonhorn. “Effect of bonding defects on shear strength in tension of lap joints having brittle adhesives”. In: *Journal of applied polymer Science* 16.8 (1972), pp. 1901–1909.
- [31] Harold Schonhorn, FW Ryan, and Tsuey T Wang. “Effects of symmetrical bonding defects on tensile shear strength of lap joints having ductile adhesives”. In: *Journal of Applied Polymer Science* 15.5 (1971), pp. 1069–1078.
- [32] M Olia and JN Rossettos. “Analysis of adhesively bonded joints with gaps subjected to bending”. In: *International Journal of Solids and Structures* 33.18 (1996), pp. 2681–2693.
- [33] Alireza Chadegani and Romesh C Batra. “Analysis of adhesive-bonded single-lap joint with an interfacial crack and a void”. In: *International journal of adhesion and adhesives* 31.6 (2011), pp. 455–465.
- [34] F L Ribeiro, L Borges, and JRM d’Almeida. “Numerical stress analysis of carbon-fibre-reinforced epoxy composite single-lap joints”. In: *International Journal of Adhesion and Adhesives* 31.5 (2011), pp. 331–337.
- [35] JW Vaningen and Arie Vlot. “Stress analysis of adhesively bonded single lap joints: Survey and evaluation of analyses”. In: *STIN* 94 (1993), p. 34643.
- [36] SLS Nunes et al. “Comparative failure assessment of single and double lap joints with varying adhesive systems”. In: *The Journal of Adhesion* 92.7-9 (2016), pp. 610–634.
- [37] Yiding Liu et al. “Experimental and numerical study of process-induced defects and their effect on fatigue debonding in composite joints”. In: *International Journal of Fatigue* 125 (2019), pp. 47–57.
- [38] R Haghani. “Finite element modelling of adhesive bonds joining fibre-reinforced polymer (FRP) composites to steel”. In: *Rehabilitation of Metallic Civil Infrastructure Using Fiber Reinforced Polymer (FRP) Composites*. Elsevier, 2014, pp. 60–95.
- [39] RC Alderliesten. *Introduction to Aerospace Structures and Materials*. 2018.
- [40] IU Ojalvo and HL Eidinoff. “Bond thickness effects upon stresses in single-lap adhesive joints”. In: *AIAA journal* 16.3 (1978), pp. 204–211.
- [41] T Kruse, T Körwien, and R Ruzek. “Fatigue behaviour and damage tolerant design of composite bonded joints for aerospace application”. In: *Proceedings of the 17th European Conference on Composite Materials ECCM-17, Munich, Germany*. 2016, pp. 26–30.
- [42] O Volkersen. *Die Niekraftverteilung in Zugbeanspruchten mit Konstanten Laschenquerschnitten*. 1938.
- [43] M Goland and E Reissner. “The Stresses in Cemented Joints”. In: *Journal of Applied Mechanics* 11 (1944).
- [44] LJ Hart-Smith. *Adhesive-Bonded Single Lap Joints*. 1973.
- [45] DJ Allman. “A theory for elastic stresses in adhesive bonded lap joints”. In: *The Quarterly journal of mechanics and applied mathematics* 30.4 (1977), pp. 415–436.
-

-
- [46] W. J. Renton and J. R. Vinson. “Analysis of Adhesively Bonded Joints Between Panels of Composite Materials”. In: *Journal of Applied Mechanics* 44.1 (1977), pp. 101–106.
- [47] Abaqus. “Abaqus 2016”. In: *Dassault Systemes Simulia Corporation, Providence, RI, USA* (2016).
- [48] Lucas FM Da Silva and Raul DSG Campilho. “Advances in numerical modelling of adhesive joints”. In: *Advances in numerical modeling of adhesive joints*. Springer, 2012, pp. 1–93.
- [49] A Turon et al. “An engineering solution for solving mesh size effects in the simulation of delamination with cohesive zone models”. In: *Engineering Fracture Mechanics* (2005).
- [50] Arne Hillerborg, Mats Mod er, and P-E Petersson. “Analysis of crack formation and crack growth in concrete by means of fracture mechanics and finite elements”. In: *Cement and concrete research* 6.6 (1976), pp. 773–781.
- [51] MM Abdel Wahab. “Fatigue in adhesively bonded joints: a review”. In: *ISRN Materials Science* 2012 (2012).
- [52] AP Vassilopoulos. “Predicting the fatigue life of adhesively-bonded structural composite joints”. In: *Fatigue and Fracture of Adhesively-Bonded Composite Joints*. Elsevier, 2015, pp. 443–491.
- [53] Matz Haaks and Karl Maier. “Predicting the Lifetime of Steel”. In: *Extreme events in nature and society*. Springer, 2006, pp. 211–232.
- [54] JA Harris and PA Fay. “Fatigue life evaluation of structural adhesives for automotive applications”. In: *International journal of adhesion and adhesives* 12.1 (1992), pp. 9–18.
- [55] KB Katnam et al. “Load ratio effect on the fatigue behaviour of adhesively bonded joints: an enhanced damage model”. In: *The journal of Adhesion* 86.3 (2010), pp. 257–272.
- [56] Jaap Schijve. *Fatigue of structures and materials*. Springer Science & Business Media, 2001.
- [57] C Lin and Kenneth M Liechti. “Similarity concepts in the fatigue fracture of adhesively bonded joints”. In: *The Journal of Adhesion* 21.1 (1987), pp. 1–24.
- [58] S Mall, WS Johnson, and RA Everett. “Cyclic debonding of adhesively bonded composites”. In: *Adhesive Joints*. Springer, 1984, pp. 639–658.
- [59] S Mall and W Steven Johnson. “Characterization of mode I and mixed-mode failure of adhesive bonds between composite adherends”. In: *Composite materials: testing and design (seventh conference)*. ASTM International. 1986.
- [60] Calvin Rans, Ren  Alderliesten, and Rinze Benedictus. “Misinterpreting the results: How similitude can improve our understanding of fatigue delamination growth”. In: *Composites Science and Technology* 71.2 (2011), pp. 230–238.
- [61] David Broek. *The practical use of fracture mechanics*. Springer Science & Business Media, 2012.
-

-
- [62] JD Engerer and Erol Sancaktar. “The effects of partial bonding in load carrying capacity of single lap joints”. In: *International journal of adhesion and adhesives* 31.5 (2011), pp. 373–379.
- [63] Huan Sheng Lai et al. “Effects of defects on failure of butt fusion welded polyethylene pipe”. In: *International Journal of Pressure Vessels and Piping* 139 (2016), pp. 117–122.
- [64] B Vieille, Jérémie Aucher, and Lakhdar Taleb. “Comparative study on the behavior of woven-ply reinforced thermoplastic or thermosetting laminates under severe environmental conditions”. In: *Materials & Design* 35 (2012), pp. 707–719.
- [65] H Khoramishad et al. “A generalised damage model for constant amplitude fatigue loading of adhesively bonded joints”. In: *International Journal of Adhesion and Adhesives* 30.6 (2010), pp. 513–521.
- [66] AD Crocombe and G Richardson. “Assessing stress state and mean load effects on the fatigue response of adhesively bonded joints”. In: *International Journal of Adhesion and Adhesives* 19.1 (1999), pp. 19–27.
- [67] R Prabhakaran, EM Somasekharan Nair, and Pramod Kumar Sinha. “Notch sensitivity of polymers”. In: *Journal of Applied Polymer Science* 22.10 (1978), pp. 3011–3020.
- [68] JJM Machado, EAS Marques, and Lucas FM da Silva. “Adhesives and adhesive joints under impact loadings: An overview”. In: *The Journal of Adhesion* 94.6 (2018), pp. 421–452.
- [69] John Tomblin et al. “Fatigue and Stress Relaxation of Adhesives in Bonded Joints”. In: *US Department of Transportation, Federal Aviation Administration* (2003).
- [70] Vlastimil Votrubec et al. “Fatigue Strength of Laser Welded Joints of PP and PC Components”. In: *World Journal of Mechanics* 8.06 (2018), p. 219.
- [71] Ives De Baere et al. “Fatigue behaviour of infrared welded joints in fibre reinforced thermoplastics”. In: *10th International Conference on Durability of Composite Systems (Duracosys-2012)*. Ghent University, Department of Materials Science and Engineering. 2012.